To Be, or Not to Be:

Cellular Homeostasis to Mechanical Perturbations

by

Shinuo Weng

A dissertation submitted in partial fulfillment
of the requirements for the degree of
Doctor of Philosophy
(Mechanical Engineering)
in the University of Michigan
2017

Doctoral Committee:

Associate Professor Jianping Fu, Chair
Professor Krishna R. Garikipati
Assistant Professor Allen P. Liu
Assistant Professor Ann L. Miller

Dedication

To my beloved grandparents and parents.

Acknowledgement

First, I would like to thank my advisor Prof. Jianping Fu for his tremendous guidance, encouragement, support, and trust in me during the past six years. I am always encouraged and inspired by his knowledge and passion for research. I am so grateful to Prof. Fu for being positive and supportive and helping me out when I faced challenges and experienced ups and downs. I sincerely appreciate his help, suggestions, and advices on research, career development, and even on life. I also thank him for being hands-off most of the time while fully supportive so that I can explore different research directions free of worries. I feel so lucky to be one of the first few students of Prof. Fu to witness the lab establishing its niche, and to grow with it and become more independent and mature.

Moreover, my deep gratitude goes to all other mentors, collaborators, and colleagues. I would like to thank other dissertation committee members, Prof. Allen Liu, Prof. Ann Miller, and Prof. Krishna Garikipati for their constructive suggestions, encouragement, support, and kindness. I appreciate that they are always making efforts to attend the meetings, share their broad knowledge and experiences with me. I would like to thank my collaborators Prof. Gary Fisher, Dr. Wei Xia, Dr. Yong Li, and Dr. Adam Helms, for their great support and suggestions on research and development of career paths.

I also express my thanks to all my fellows, past and present, in the Fu Lab: Dr. Weiqiang Chen, Dr. Yubing Sun, Dr. Raymond Lam, Dr. Koh Meng Aw Yong, Dr. Yi Zheng, Dr. Zeta Yu,

Yue Shao, Xiang Li, Zida Li, Jianming Sang, Xufeng Xue, Sajedeh Esfahani, Chun-Yen Sung, Jennifer Mann, and Liang-Ting Jiang. I appreciate the every minute spent with you in the lab and the office working on various projects, tackling the problems, discussing career plans, and even talking nonsense. I would also like to thank the big bio family in the Mechanical Engineering Department: Prof. Katsuo Kurabayashi, Prof. Nikos Chronis, Prof. Allen Liu, Prof. Edgar Meyhofer, and the current and previous lab members of them, Dr. Pengyu Chen, Dr. Bo-Ram Oh, Dr. Mayurachat Gluari, Dr. Eleni Gourgou, Dr. Luciana Rosselli-Murai, Dr. Shue Wang, and Dr. Neha Kaul, to name a few. I appreciate that you are such great neighbors and colleagues and are always happy to share your space, expensive equipments, and invaluable knowledge and expertise.

Besides the friends from work, I would also like to thank the others: Dianyun, Weixian, Yi, Joyce, Yuqing, Keqin, Kejia, Biqiao, Kaitlyn, Dena, PJ, Maggie, Bai, as well as all of the others in my heart. I appreciate so much for your love and support, and I am grateful to having you in my life.

At last, my love goes to my dearest parents and grandparents. Without your trust, support, patience, and love, I could not overcome the hardships and difficulties that I encountered studying abroad on my own. I appreciate it from the bottom of my heart that you take great care of yourself, live happy and healthy.

This work is financially supported by the National Science Foundation (NSF; CMMI 1129611 and CBET 1149401), National Institutes of Health (R21 HL114011 and R21 EB017078), American Heart Association (AHA SDG 349249), and the Rackham Summer

Award. My PhD study is also supported in part by the Mechanical Engineering Departmental Fellowship and the Rackham Barbour Scholarship, to which I am very grateful.

Table of Contents

List of Figures

List of Tables

List of Appendices

Abstract

Mechanical homeostasis is an emerging mechanobiology concept that describes the critical biological process to maintain whole-cell/tissue physiology against forces and deformation arising both intra- and extracellularly. Dysregulation of mechanical homeostasis has important implications in pathophysiological conditions such as developmental defect, cardiovascular and pulmonary diseases, and cancer. Mechanical homeostasis has been commonly investigated at molecular, cellular, tissue levels and beyond. However, in mechanical homeostasis collective dynamics at smaller scales and its functional relationship with emergent system-level properties at larger scales remains elusive.

The major contribution of this dissertation is to provide a detailed picture of the functional link between molecular and subcellular events and apparent cellular behaviors under mechanical perturbations. A novel suite of technologies, involving microfabrication, live-cell imaging, high-throughput and multidimensional image processing, and mechanical characterization, have been developed and implemented in this research for the live-cell study of both subcellular and cellular aspects of mechanical homeostasis. By utilizing these techniques, we performed cell stretch experiments and quantitative measurements of biomechanical and biochemical responses with a spatiotemporal resolution to examine cell behaviors upon mechanical perturbation. Our data have revealed that cellular mechanical homeostasis is an emergent phenomenon driven by collective and graduated, yet non-homeostatic, subcellular behaviors (“subcellular rheostasis”) that follow distinct mechanosensitive compensatory paths.

We have for the first time shown that subcellular dynamics would observe patterns different from that at the single-cell level. Further investigations have revealed that impairment to the extracellular matrix (ECM) – focal adhesion (FA) – cytoskeleton (CSK) mechanical linkage can lead to an effective exit from cellular mechanical homeostasis by skewing the subcellular rheostasis pattern of FAs, which might be a sensitive gating mechanism of cellular homeostasis. Lastly, a mechano-biophysical model has been constructed in this work to quantitatively recapitulate experimental observations of subcellular rheostasis and its perturbation by different drug treatments. Cross-examination of experimental and theoretical modeling results has unveiled the regulatory roles of different mechanosensitive machineries including catch-slip bonds and myosin motor activity in governing the emergence of cellular mechanical homeostasis.

Chapter 1

Introduction

1.1 Background and motivation of research

Mechanobiology is an emerging research field at the interface of biology, physics, and engineering. Over the last few decades, it has become increasingly appreciated that cells and tissues are not only complex biochemical systems that govern life through cascades of biochemical reactions, but also sophisticated biomechanical systems where physical factors play significant roles in controlling proper biological function, shape, and organization. Mechanical interactions between biological matters and their environments provide physical scaffolds to hold subcellular organelles and multicellular tissues in place for proper shape and organization in a passive manner. Such mechanical interactions also actively and directly act on molecules and cells to trigger mechanosensitive biochemical responses, leading to apparent biochemical and biomechanical properties of cells and tissues [1-21].

There is strong evidence suggesting that intracellular and extracellular mechanical interactions contribute to physiological and pathological processes in embryo development and adult animals. Intracellular and extracellular mechanical interactions come into play during embryo development and morphogenesis, where the mechanics of the extracellular matrix (ECM), cell contraction force, and force transmission between cells and cells and ECM are well

coordinated to control cell fate decision, pattern formation, and tissue morphogenesis [15, 17, 22, 23]. For instance, cell contraction force plays a key role in mitotic spindle positioning that governs symmetric and asymmetric cell division to establish polarity in the embryo [24-27]. Before blastocyst implantation into the uterine endometrium, physical confinement from the maternal tissue generates a non-uniform force distribution in the blastocyst. The distinct mechanical environment of cells in the blastocyst alters the localization and activation of mechanosensitive transcriptional factors, such as YAP and TAZ, in the inner and outer cells, so that inner cells are committed to inner cell mass lineage, whereas outer epithelium becomes committed to trophectoderm [28-30]. Later during embryonic development, cells self-assemble to form complex 3D shapes. Epithelial cells, for example, create contraction at the apical side of cell sheets that deform the cell sheets and generate a variety of tissue shapes during gastrulation, neural tube formation, and gut formation [31-34].

The functional and regulatory roles played by mechanical cues are more obvious in adult animals for the maintenance of mechanical strength and functions of tissues and organs. For example, fluid shear stress exerted by blood flow is a strong modulator of phenotype and function of vascular endothelial cells and smooth muscle cells [35-42]. Turbulent flows at blood vessel branches can create an athero-prone environment where endothelial cells have a greater risk of losing their antithrombotic properties and switching to a proinflammatory state that precedes atherosclerosis [13, 38, 41, 42]. During the progression of atherosclerosis, dysfunction of endothelial synthesis and secretion of bioactive molecules such as nitric oxide, a smooth muscle relaxant to reduce cell contraction, promotes macrophage infiltration and smooth muscle cell overproliferation that leads to hardening of vessel walls [43-46]. Stiffened of ECM further promotes proliferative phenotypic change of smooth muscle cells, extravasation of immune cells,

and destabilization of cell-cell contact in the endothelium that accelerate disease progression in a feed-forward manner [47-52].

Mechanical signals transmitted from molecules, cells, and tissues form feedback or feed-forward control systems together with chemical signals to control gene expression and cell/tissue functions. Insight into these mechanical perspectives of cell and tissue regulation can lead to the development of improved medical devices, biomaterials, tissue engineering approaches, and stem-cell-based therapies [53-56]. Therefore, understanding how mechanical signals are sensed and converted to chemical signals is important.

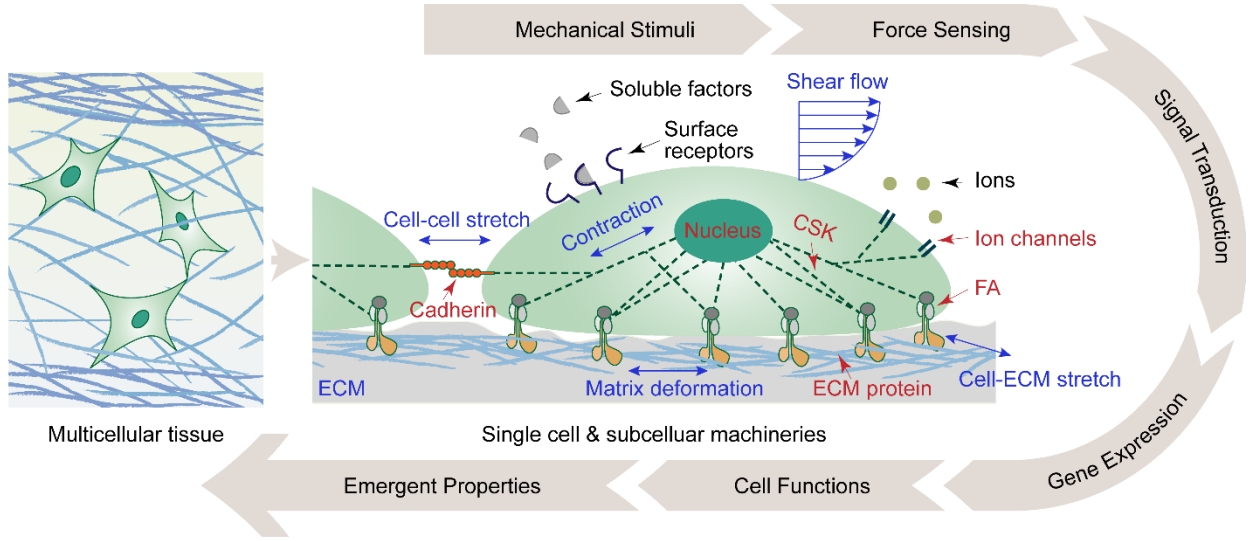

Figure 1-1 Schematic showing the framework of this study on mechanotransduction and cell mechanics. The purpose of this study is to decipher the functional link between processes of mechanotransduction at different length and time scale, including sensing of mechanical stimuli, signal transduction, gene expression, cell function, and the emergent biomechanical and biochemical properties of cells and multicellular tissue.

The processes of mechanosensing and mechanotransduction involve both intracellular and extracellular components, and the main structural contributors include mechanosensitive ion channels, cell surface adhesive proteins, the nucleus, and the actomyosin cytoskeleton (CSK) network, as illustrated in **Figure 1-1**. Mechanosensitive ion channels (or stretch-gated ion channels) are critical for touch and hearing sensation as well as feeling and memory formation [57-61]. They can be opened by mechanical force and deformation to generate electrical signals and ion flux. Cell surface adhesion molecules including focal adhesion (FA) and cadherin are involved in cell attachment to surrounding ECM and neighboring cells, respectively. FAs bind to the ECM via integrins to mediate cell-ECM interactions thus sensing the biomechanical and biochemical properties of the ECM [62-67], while cadherins bind to homotypic or heterotypic substrates from neighboring cells to mediate cell-cell interactions [68, 69]. The cell nucleus has its own mechanical properties, which can change with the transcriptional profile and respond to mechanical stimuli in terms of altered gene expression [70-73]. All of the aforementioned components are connected to the actin CSK, a network of actin filaments that maintains cell shape and mechanical strength. It physically connects ion channels, cell adhesion proteins, and the nucleus to direct force transmission between cells and cells and the ECM and mechanically integrate them in tissues [62-75]. More importantly, it generates the actomyosin contraction to balance intracellular and extracellular forces, change cell shape, drive cell movement, and trigger mechanosensitive signaling pathways by altering the mechano-chemistry of force-sensing molecules including the CSK itself [76-80]. With different density and length and cross linker density and types, the actin CSK displays various architectures with distinct kinetics, dynamics, and mechanics that together determines the emergent mechanical properties of cells such as cell stiffness, contractility, and motility [77, 81].

These structural components and signaling molecules comprise an interconnected and dynamic mechano-chemical system that senses mechanical stimuli such as shear flow, ECM deformation and cell stretches, and transduce mechanical cues into biochemical signals, regulate gene expression that determines cell functions and emergent biomechanical and biochemical properties of multicellular tissues (**Figure 1-1**). The hierarchical nature of biological organisms where molecules, cells, tissue, organs and beyond orchestrate to accomplish complex goals of physiological processes, adds another layer of complexity and regulation to the system. Therefore, elaborate spatiotemporal regulation is essential to mediate diverse physiological processes across different time and length scales from remodeling of actin cytoskeleton to cell migration to cytokinesis and to tissue morphogenesis.

From different *in vitro* and *ex vivo* experiments, scientists have observed that different mechanical properties at cell and tissue scales may be associated with common molecular combinations and similar mechanisms. For instance, tensile and compressive forces observed on segments of actin filaments are generated by identical actomyosin interactions [82-84]. Likewise, the highly dynamic molecular activities, such as stress fiber remodeling and microtubule remodeling, give rise to a dynamic, yet robustly quasi-static state at cellular and tissue levels when they are in a varying mechanical environment. These divergent observations at different scales highlight the scaling inconsistency in biology, and imply the necessity for a multi-dimensional and multiscale analysis of physiological processes including mechanosensing. Specifically, it will be critical to unravel the spatiotemporal coordination and cooperation between different molecules, architectures, and mechanisms for understanding the emergent physiological behaviors.

Besides elegantly designed experiments, there is also a growing need for predictive computational models for studying mechanobiology and mechanotransduction. With quantitative experimental data, knowledge from biology, physics, mechanics, material science, and mathematics could be employed and integrated to create mechano – chemical – biophysical models that recapitulate certain aspects of biological systems, and to identify critical regulatory parameters in the interconnected mechanosensitive responses and their mechanisms.

The research described in this dissertation has focused on a particular mechano-biological behavior - mechanical homeostasis, for which a detailed introduction is provided in **Chapter 3**. This research study is pursued starting with the development of tools (**Chapter 2**), following by experimental findings (**Chapter 3**) and theoretical modeling (**Chapter 4**).

1.2 Research topics and dissertation outline

This dissertation will discuss interdisciplinary research that integrates microengineering, cell and molecular biology, and computational modeling for elucidating the spatiotemporal coordination of mechanotransduction and its regulatory roles in cell mechanics and functions.

In this chapter, I have briefly introduced the vibrant and rapidly progressing research field of mechanobiology, the basic theories and findings underlying how mechanical interactions may be sensed and transduced throught the ECM – FA/cadherin – CSK – nucleus mechano-chemical linkage that eventrually change cell behaviors, and the direction we are going to pursue for a more complete understanding of the multiscale and multidimensional mechanobiological behaviors of cells and tissues. In the following chapters, I will summarize my major

accomplishments and conclusions from my studies on mechanotransduction and cell mechanics. As most of the research described below has been peer-reviewed and published, the individual chapters of my dissertation are adapted from published manuscripts with changes that are necessary for consistency.

In **Chapter 2**, I describe a set of engineering tools for exploring mechanosensing, mechanotransduction and cell mechanics that have been developed over the last few years by my lab mates and me [85-89]. There is always a demand for technological advances for mechanobiology and cell mechanics that could radically change the way we decipher the black box of a cell. The current techniques such as optical tweezers [90-92], atomic force microscopy [93, 94], microengineered micropipette aspiration [95], and microengineered contractile force microscopy [96] have enabled us to apply mechanical forces to cells and molecules and measure the mechanical and chemical responses. However, the majority of these techniques tend to test and analyze a single cell at a time and subcellular structures separately so that the intracellular connection cannot be reconstructed from the data collected. The toolkit we have described here is named micropost array cytometry. It is capable of applying various forms of mechanical stimulations to single cells or a small multicellular colony and simultaneously measuring their biomechanical and biochemical properties and their spatiotemporal evolution. The linkages between behaviors at cellular and subcellular scales as well as the linkages between biochemical and biomechanical attributes are well preserved in the data acquisition process for studying their relation and correlation. **Chapter 2** starts with a brief introduction of the techniques currently used for mechanotransduction followed by a detailed description of the novel techniques developed by us that are incorporated into a cytometry system. Short introductions are given at

the beginning of each section to discuss the demand and the merit of the techniques we have developed.

Chapter 3 explores the temporal coordination between cellular and subcellular responses of cell contraction (or "CSK tension") and FA dynamics during the process of single-cell mechanical homeostasis. Recent studies on single cells experiencing mechanical perturbation have shown both single-cell tensional homeostasis and strain rate-dependent tensional buffering with different testing systems that likely mimic different microenvironments [86, 96, 97]. In this chapter, we use the novel experimental platform described in **Chapter 2** to apply sustained stataic cell stretch while measuring the biomechanical output of CSK tension and biochemical output of FA dynamics at both cellular and subcellular scales. We demonstrate for the first time that single-cell mechanical homeostasis is driven by collective and graduated, yet non-homeostatic, subcellular behaviors ("subcellular rheostasis") of CSK tension and FA [88]. We show that subcellular rheostasis involves a mechanosensitive compensatory pattern wherein ground states of CSK tension and FA determined their distinct reactive paths *via* either relaxation or reinforcement. Distortion of the subcellular rheostasis pattern of FAs, when the structural and functional integrity of the ECM – FA – CSK mechano-chemical linkage is impaired, leads to non-homeostatic behaviors of FAs at the single-cell level. We conclude that the apparent single-cell behavior is collectively determined by subcellular dynamics, and a distinction between behaviors at subcellular and cellular scales might be general in various cellular responses.

In **Chapter 4**, we describe a mechano-biophysical model that is inspired by the experimental observations in **Chapter 3** to explain the origin and regulation of subcellular rheostasis and how it determines the maintenance or exit of mechanical homeostasis [88]. Via

cross-examining experimental and theoretical results, we have not only validated the assumptions and the predictive power of the theoretical model, but also showed that the mechanisms incorporated in the model are both sufficient and necessary for recapitulating experimental findings. The theoretical model developed in the present work has provided unique insights revealing the most essential, sometimes seemingly simplistic, mechanisms underlying complex systems-level cellular dynamics. Our results underscore the significance of theoretical modeling in assisting mechanistic investigations of cell behaviors.

Finally, **Chapter 5** first recaps the research questions this dissertation seeks to address and how I have tackled them, highlights the accomplishments, and key conclusions from each work. Then, I briefly discuss the questions raised from this work and questions which we need to be exploring next. To conclude, I briefly introduce and describe future work in which the experimental techniques and the theoretical model we have developed in this dissertation can be implemented in combination with others to study an interesting open question about cell memory to mechanical history. In short, the direction is to investigate how the mechanical history influences biomechanical and biochemical properties of cells via spatiotemporal coordination of the highly dynamic ECM – FA – CSK – nucleus linkage, and to explore the structural components that retain the non-genetic cell memory of mechanical history.

Chapter 2

Micropost array cytometry, an engineered system to interrogate cell mechanics at the cell and subcellular scale

The major content of this chapter is reproduced from our previously published papers: “Synergistic regulation of cell function by matrix rigidity and adhesive pattern” in Biomaterials, 2011 [85], “A silicone-based stretchable micropost array membrane for monitoring live-cell subcellular cytoskeletal response” in Lab on Chip, 2012 [86], “Live-cell subcellular measurement of cell stiffness using a microengineered stretchable micropost array membrane” in Integrative biology , 2012 [87], and “Mechanosensitive subcellular rheostasis drives emergent single-cell mechanical homeostasis” in Nature Materials, 2016 [88]; and book chapter “Stretchable micropost array cytometry: a powerful tool for cell mechanics and mechanobiology research” in “Integrative Mechanobiology: Micro- and Nano- Techniques in Cell Mechanobiology”, 2015 [89].

2.1 Introduction

The field of mechanobiology has been growing dramatically in the past decades, and it is getting more and more appreciated by the cell biologists that almost every cell types, from

prokaryotes to multicellular organisms, are mechanosensitive. Cell senses, analyzes and integrates the signals from its environment, both chemical and physical, and consequently change its dynamic behaviors, morphology, its internal and external environments, and eventually, fate [1-21, 98].

For adherent cells to grow and function, it is crucial for them to maintain their close association with the neighboring homotypic or heterotypic cells via cell-cell interaction [65-67], or with the various interstitial matrices or basal membranes via cell-ECM interaction [68, 69, 99]. In recent years, it has become increasingly clear that the cellular responses to signals from microenvironment go far beyond its ability to sense specific ECM ligands chemically, and it covers a broad range of physical cues at the interface between cells and the surrounding matrix. Numerous studies have demonstrated that the capability of cells to respond to multiple biointerfacial parameters, including adhesive ligand density and pattern [100-102], surface compliance (or ECM rigidity) [103-109], and ECM dimensionality and anisotropy [110-112], ECM deformation, shear flow [35, 36, 38, 47, 113-115], hydrodynamic pressure [116], tugging or squeezing from neighboring cells [117], among other signals. It is generally believed that the cellular machinery of mechanical sensation is capable of integrating this complex information by globally altering cytoskeleton organization and the cell shapes [14, 118-120], and locally modulating adhesion dynamics and signaling activity [6, 9, 121].

The exploding advances on the understanding of cell mechanobiology over the last decades rely on the technological advances. Microengineered tools and molecular tools have been developed to reveal the interplay between mechanical loading and changes in biochemical and biomechanical properties of cells [122-124]. Brief introductions to the specific areas that we

have contributed to are provided in the following sections. We suggest the readers refer to the reviews in Ref [124] for the available molecular tools to perturb and measure the bio-mechano-chemical responses which are not discussed here.

To contribute toward this effort, we have recently developed a biomechanical toolkit, termed stretchable micropost array cytometry [85-89]. It is capable of quantitative control and application of mechanical regulatory cues to the live cells and real-time measurement of cellular biochemical and biomechanical responses with high spatiotemporal subcellular resolution. Specifically, the stretchable micropost array cytometry integrates high-resolution elastomeric micropost arrays that are tunable cell culture substrates and subcellular force sensors, with a vacuum driven cell-stretching device, such that cells cultured on the micropost arrays could be stretched globally via the local probes of microposts. Leveraging fluorescence live-cell microscopy and image processing techniques, we can acquire multidimensional and multi-content attributes of cells that cover both the biomechanical and biochemical aspects with spatio-temporal resolution. In this chapter, we describe the development of the stretchable micropost array cytometry, followed by highlighting the computational algorithms developed for the multidimensional analysis of biochemical and biomechanical responses of cells. We conclude with remarks regarding future improvements and applications of this toolkit for cell mechanics and mechanobiology studies.

2.2 Micropost arrays to regulate mechanics of cell culture substrate

ECM is the substrate where cells adhere, grow, and function. It consists of a complex mixture of functional and structural macromolecules and serves an instructive role in tissue and organ morphogenesis and maintenance of cell and tissue functions. ECM proteins and the recruited soluble factors such as growth factors provide chemical signals to the cells via ligand-receptor interactions to trigger the downstream biochemical machinery involved in the control of gene expression. In the last decades, it has been widely appreciated that indeed this process is regulated by physical parameters in the Cell-ECM interfaces, which include ligand density and pattern [100-102], surface compliance (or ECM rigidity) [103-109], ECM anisotropy and dimensionality [110-112], and surface nano-topography [125-127]. Therefore, investigations on cellular phenomena at the bio-interface should get both chemical and physical cues involved.

Conventional methods to study cell-ECM interactions have largely relied on natural and synthetic hydrogels [5, 50, 128-130]. Although these hydrogel systems have proven important to deepen our understanding of cellular sensing of environmental signals, there are still certain limitations that prevent their applications in some detailed investigations on Cell-ECM interaction [119, 128, 129]. For example, conventional methods using hydrogels derived from natural ECM proteins (such as collagen I, fibrin, and Matrigel) are known to have difficulty controlling their bulk mechanical properties, and changes in the gel stiffness cannot be decoupled from their other parameters such as ligand density and gel porosity. On the other hand, the synthetic hydrogel systems such as polyacrylamide (PA) or polyethylene glycol (PEG) gels present a significant advancement for studies of cell-ECM interactions [108, 130, 131], as they have well-defined bulk mechanical properties and chemical activities, and can be functionalized with various adhesive peptides and functional proteins using linker chemistry; nevertheless, they are still not immune to molecular-scale changes in porosity, wettability, polymer chain mobility,

and binding properties of immobilized adhesive ligands that accompany changes in their bulk stiffness [119, 129], which has been shown having profound effects on cellular functions [132-134]. For example, a recent study using synthetic hydrogels for human pluripotent stem cells indicates that these molecular-scale changes in wettability and surface topology can have significant effects on stem cell survival and cloning efficiency [132]. Other reports clearly suggest that the nanoscale local alterations in receptor-ligand binding characteristics could strongly influence cellular sensing of ECM surface properties and thus downstream cellular behaviors [133, 134].

Although the natural and synthetic hydrogel systems discussed about will continue to be important in characterizing and controlling cell-ECM interaction for fundamental studies as well as tissue engineering and regenerative medicine, there is a great need for new types of synthetic materials with which multiple parameters such as, but not limited to surface chemistry, adhesive pattern, topography, and mechanics can be modified independently and precisely to facilitate the quest for design principles and material selection rules to control cellular responses (ref) [129, 135, 136].

In particular, we target the mechanics of ECM that has been proven critical in cellular processes such as cell motility, survival, growth, and differentiation. Instead of chemical modification on the synthetic biomaterials, we take the strategy of geometrical and topological modification of the ECM to control its physical properties. Recently, our group and some others have proposed an idea of using microfabricated elastomeric polydimethylsiloxane (PDMS) micropost arrays to regulate substrate rigidity independently of effects on the adhesive and other material surface properties [137, 138]. Our approach involves a library of replica-molded arrays

of hexagonally spaced PDMS microposts from microfabricated silicon masters, which present the same surface geometry but different post heights to control substrate rigidity. Cells adhered on the PDMS microposts contract and bend the underlying posts, and the amount of post bending magnitude is related to the compliance of the posts sensed by cells which future regulated the cell contractility (**Figure 2-1 a&b**). The spring constant K of the PDMS micropost is solely determined by its geometry and the *Young*'s modulus E of the PDMS, and K can be approximately calculated using the *Euler-Bernoulli* beam theory as $K=3\pi ED^4/(64L^3)$ [138-140], where D and L are the PDMS post diameter and height, respectively. The substrate rigidity of the PDMS micropost array can be further characterized using the effective *Young*'s modulus E_{eff}, which is equivalent to the *Young*'s modulus of *a* continuous elastic substrate whose local surface deformation is the same as that of a PDMS micropost, and E_{eff} is expressed as $E_{eff} = 9K/(2\pi D)$ [138] (**Figure 2-1 c**) . Thus, the rigidity of the PDMS micropost array can be modulated simply by varying the post height L and diameter D while keeping all other aspects of the substrate such as surface chemistry, ligand density, and bulk and nanoscale mechanics of the substrate unchanged. In our previous study, we have shown that indeed, the rigidity of the PDMS micropost array can significantly influence cell morphology, focal adhesion (FA) formation, cytoskeletal contractility, and stem cell differentiation [137, 141-143].

As most of the existing biomechanics studies that characterize biointerfacial cellular phenomena with changes on individual biophysical parameters in the cell microenvironments, micropost arrays have been used by us and some other research groups to study the independent effect of substrate rigidity on the trigger of downstream intracellular signaling cascade and cellular responses, the synergistic and collective regulations of cell behaviors by a combination of different biointerfacial parameters with substrate rigidity are still elusive and largely

uncharacterized, which will clearly hamper future efforts to design efficient synthetic materials and biointerfaces containing multiple biophysical signals to collectively direct cellular behaviors. To specifically address this issue and thus advance our current understanding of the combined influences of different biointerfacial parameters on cellular behaviors, we took advantage of the unique characteristic of the PDMS micropost array whose mechanical rigidity could be easily and completed decoupled from its surface properties including the ECM ligand and the presentation of the ECM pattern, to study the synergistic and independent effects of substrate rigidity and adhesive ECM pattern on cell spreading, FA formation, cytoskeletal contractility, and proliferation of different types of adherent mammalian cells.

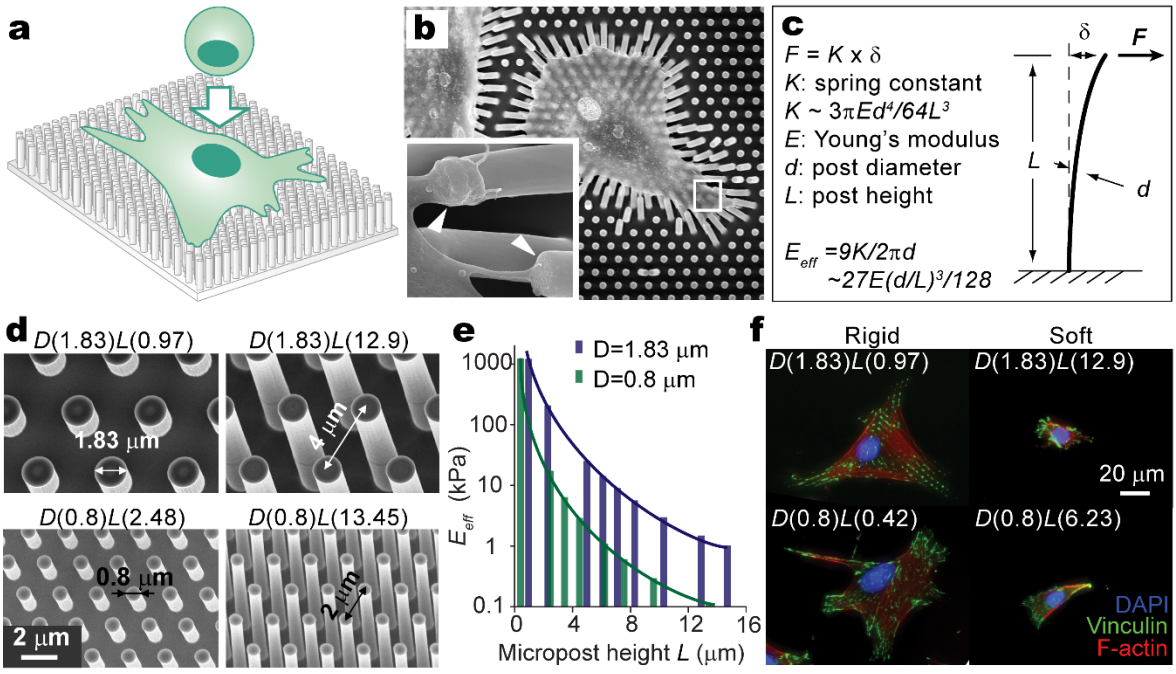

Figure 2-1 Microfabricated PDMS micropost arrays to engineer physical properties of the cell culture substrate. (**a**) Schematic showing cell culture on the PDMS micropost arrays. (**b**) Representative scanning electron microscopy (SEM) image of cells spreading on top of PDMS microposts and bending the underlying posts. (**c**) A mechanical model of the microposts, demonstrating that the effective rigidity of the PDMS micropost array could be regulated by its

geometry. (**d**) Representative ECM images of silicon micropost masters with various post diameter and post height. (**e**) The effective rigidity of two sets of micropost arrays and its dependence on the post height (*blue*: D = 1.83 μm; *green*: D = 0.8 μm).

In this study, we designed and fabricated two sets of hexagonally spaced micropost arrays with different post diameter D and center-to-center distance S to manipulate the adhesive pattern, and a variety of post length L that independently modulate the effective modulus of the PDMS micropost arrays E_{eff}. The first set of PDMS micropost arrays had a post diameter D of 0.8 μm, a post center-to-center distance S of 2 μm, and post heights L ranging from 0.42 μm to 13.45 μm (**Figure 2-1 d&e**). The other set of PDMS micropost arrays had a post diameter D of 1.83 μm, a post center-to-center distance S of 4 μm, and post heights L ranging from 0.97 μm to 14.7 μm (**Figure 2-1 d&e**). For convenience, the PDMS micropost array with a post diameter of x μm and a post height of y μm was designated as 'micropost array D(x)L(y)'. Of note, the two sets of micropost arrays have a comparable percentile of adhesive areas, but distinct adhesive patterns- the adhesive sites in D(0.8) set are smaller and denser and those in D(1.83) set are larger and looser. By changing the length L of the micropost independently in each set, the two sets of microposts together produced a more than 10,000-fold range of rigidity from 0.10 kPa (D(0.8)L(13.45)) to 1,200 kPa (*D(0.8)L(0.42)*) (**Figure 2-1 d&e**), that is much broader than that is currently achieved by natural or synthetic hydrogels (ref). Three different PDMS micropost arrays were deliberately selected from each of the two sets of PDMS micropost arrays (**Table 2.1**) and paired together based on their comparable effective moduli E_{eff} (1 kPa or *soft* (D(0.8)L(6.23) vs. D(1.83)L(12.9)), 15 kPa or *medium* rigidity (D(0.8)L(2.48) vs. D(1.83)L(6.1)), and 1,200 kPa or *rigid* (D(0.8)L(0.42) vs. D(1.83)L(0.97)), which covered a broad range of mechanical stiffness

and were physiologically relevant to different human tissues where mechanics and forces have been proven important for their physiological and pathological functions.

Table 2.1 Configuration of micropost arrays.

Array designation	Post diameter D (μm)	Center-to-center distance S (μm)	Post height L (μm)	Post rigidity K (nN/μm)	Equivalent modulus E_{eff} (kPa)
D(0.8)L(0.42)	0.8	2	0.42	688.4	1232.6
D(0.8)L(2.48)			2.48	9.7	17.9
D(0.8)L(6.23)			6.23	0.6	1.1
D(1.83)L(0.97)	1.83	4	0.97	1556.7	1218.5
D(1.83)L(6.1)			6.1	18.2	14.2
D(1.83)L(12.9)			12.9	1.9	1.5

We applied these PDMS micropost arrays to systematically study the synergistic and independent effects of substrate rigidity and adhesive ECM pattern on mechanoresponsive cellular behaviors, including cell spreading, FA formation, cytoskeletal contractility, and proliferation. Our results demonstrated a close interplay of matrix rigidity and adhesive ECM pattern in regulating mechanoresponsive cellular behaviors in a cell type-specific manner [85]. Take the cell spreading and FA formation for example, as shown in **Figure 2-1 f**, NIH/3T3 fibroblasts have previously been shown to respond to mechanical cues both *in vivo* and *in vitro* did respond to rigidity changes of the PDMS micropost arrays and exhibited marked differences in their degrees of attachment and spreading. Cell plated on the *rigid* substrate spread to a large projected area and shown highly organized actin fiber networks and distinct and mature adhesions that closely mimicked the hexagonal arrangement of the PDMS micropost tops. In contrast, cells plated on *soft* substrate displayed a rounded or spindle-shaped morphology, poorly

organized actin filaments, and small-punctuate adhesion. We also observed in some cases elongated adhesions bridging two or more PDMS microposts at the cell periphery for cells plated on the *soft* PDMS micropost arrays. This observation was more prominent for the *D*(0.8) micropost arrays, which likely could be attributed to their shorter center-to-center distance and lower spring constant, facilitating FAs to bridge neighboring posts to form a bigger complex. This process could have a significant impact on the FA turnover and thus the motility of the cells, which have potential to explain the processes like mesenchymal-epithelial transition (EMT) and cancer cell metastasis. In this study, our investigations not only suggested the important applications of our PDMS micropost arrays in investigating mechano-sensing and -transduction processes and biointerfacial phenomena but also provided the basis for future studies to unravel integrated cellular responses to complex biomechanical stimuli and to design synthetic biomaterials for tissue engineering and regenerative medicine.

To conclude this session, micropost array system is an effective way to regulate the mechanics of the cell culture substrate by solely changing the length of the microposts. Therefore, micropost array system is capable of studies on the independent and synergistic regulation by substrate rigidity and other biointerfacial properties including but not limited to the adhesive ligand [100-102], surface nano-topography [125], ECM dimensionality and isotropy [110-112]. Of note, invented as a tool to measure live-cell subcellular cytoskeleton contractile force, one of the most important outputs for the study of mechanotransduction, micropost array system has become the most efficient alternative approach to the traction force microscopy that is widely used in the hydrogel systems. (The application of the micropost arrays as force sensors will be discussed in brief in **Section 2.4**.) Being such a versatile system, there is a great trend to add on more by integrating the micropost arrays with other techniques such as microfluidics [144,

145], magnetic wire-actuator [146, 147], magnetic/optical/acoustic tweezers [148-151], and cell stretching devices [97, 152-155] to apply local or global stimuli to mimic the mechanical signal in the microenvironment other than the substrate rigidity and different adhesive surface properties. Altogether, we claim that the application of micropost arrays in the studies of cellular mechanotransduction is indispensable and irreplaceable.

2.3 Cell stretching device to apply mechanical stimulation

Cells and tissues in our body are continuously subjected to different kinds of mechanical stresses including tensile and compressive forces and shear stress. These mechanical stimuli play important roles in various biological processes at the molecular and cellular scales to determine the maintenance and alteration of cell functions such as proliferation, differentiation, contraction, migration, and inflammatory responses. For example, cyclic stretch to smooth muscles and cardiomyocytes have been shown critical for the cell maturation and synchronized vasomotion [156-160]; the pattern of shear stress is an important mediator of the inflammatory response of endothelial cells [161-163]; and stretch to fibroblasts can tune the secretion proteins such as matrix metalloproteinases (MMPs) that is closely related to aging and chronic sport injury [164-167].

Many tools and techniques have been developed in particular to provide mechanical perturbations as a means to mechanically probe cellular components such as adhesion complex and cytoskeleton, and study the roles of mechanical forces in cell biology, tissue engineering, and regenerative medicine.

Techniques applying local mechanical perturbation to the cells are usually used to measurement local mechanical properties or study force-dependent dynamics of specific molecules in mechanotransduction. Micropipette aspiration is one of the techniques to deform a cell thus characterizing its mechanical properties [168-171]. It applies a precisely controlled vacuum pressure to a small area on a cell via a glass micropipette and measures the aspiration length of the cell into the micropipette as a result determined by the applied pressure and the mechanical properties of the cell. Combined with live-cell imaging, the micropipette aspiration technique is also used for time-lapse studies of force-dependent molecular functions [172]. Optical tweezer (also known as laser trapping) [90-92] and magnetic tweezer [27, 173] [148, 174] are similar techniques that use either optical laser field or magnetic field to control the displacement of microbeads (magnetic microbeads for magnetic tweezer) within a defined region in a cell or on the cell surface. Microbeads are coated with adhesive ligand or antibody to bind to specific receptors on or in the cells thus probing specific cellular components and signaling pathways. The forces applied by the tweezers to balance forces from the cells can be calculated by the parameters of the (optical/magnetic) fields and the microbeads. Typically, a suspension cell is attached with two microbeads, one fixed to the surface of a glass slide, and the other moved by the tweeze to generate a steady or time-varying stretching force to the cell [90]; while an adhesive cell is only attached to one moving microbeads [174]. Because the microbeads are coated with specific ligands or antibodies, the mechanical and mechanochemical responses to the applied stress are highly selective in contrast to the micropipette aspiration technique. Similarly, atomic force microscopy (AFM) uses an electronic controller to move an elastic cantilever beam over a cell [93, 94, 175-177]. The end of the cantilever has a nano-microscopic tip functionalized with the adhesive ligand to bind the surface receptors. Once the force is caught

on the tip, the electronic controller can move the cantilever to apply local stretch or indentation on the cell, and the force is measured by measuring the deflection of the cantilever. Sophisticated AFM can scan over the entire cell surface to measure the local properties such as height, stiffness, and protein distribution. Optical tweezer, magnetic tweezer, and atomic force microscopy are also widely used in *in vitro* experiments to measure the force-dependent binding between molecules [93, 178-181]. Another technique to apply a local mechanical load to cells is the acoustic tweezers [150, 151]. It uses the acoustic wave to vibrate the lipid microbubbles covalently attached to cells surfaces via adhesive ligand-receptor binding. The magnitude, frequency, and duration, and period of the applied forces are fully determined by the ultrasound parameters, yet it is not able to control the position of the microbubbles. However, the use of ultrasound and the microbubbles are FDA-approved that endure it the potential for the *in vivo* medical treatment. Laser surgery is a distinct technique that cut the cytoskeleton at a precisely controlled position to apply local mechanical perturbation [182-185]. With live-cell fluorescent microscopy, scientists use it to study mechanical properties of the cytoskeleton and how the cells accommodate the loss of local internal contraction via spatiotemporal variation and remodeling.

In contrast to techniques as mentioned above that apply local mechanical perturbations, techniques for the application of global mechanical stimulation and perturbation has two major categories: fluidic devices to apply shear flow and hydrodynamic pressure [186], and cell stretching devices to apply whole-cell stretch [187]. Fluidic devices are usually applied to the tissues or cell types that are exposed *in vivo* to stress flow, interstitial flow, and osmosis flow, such as vascular cells, blood cells, epithelial cells, bone cells, and cancer cells, to probe their associated biological responses [115, 145, 188-190]. Cell stretching devices are used to provide predefined cell stretching profiles to cells, small colonies, micro-tissues, or tissue samples that

are known to experience various patterns of deformation such as cardiomyocytes, vascular cells, skeleton muscles, fibroblasts, and bone cells [97, 152-155]. Fluidic devices and cell stretching devices are commercially available for the study of mechanobiology, yet many groups prefer to customize the system to mimic the specific mechanical stimuli in the physiology of their interest. In these studies, the cellular responses such as contraction, differentiation, and protein synthesis are usually treated as the average of the whole object, neglecting the variations between different subgroups.

As discussed in **Chapter 1**, acquiring the mechanosensitive responses at different length scales will provide additional information for the understanding of the connection between the various molecular mechanisms and the transition among various architectures that eventually give rise to the emergent behaviors of the whole objects. Therefore, the technique we developed here is aiming to gain the merit from both, applying local and global stimuli, and observing the local and global responses in the same platform simultaneously.

Our strategy involved a vacuum driven stretching device (CSD) to apply global stretching to an elastic PDMS basal membrane and the micropost array described in integrated on the basal membrane that discretizes the deformation of the basal membrane [86, 88, 89, 191]. The integration of the elastic basal membrane and the micropost array was named stretchable micropost array membrane (**Figure 2-2 b**). By doing so, the cells attached to the top of the microposts as is illustrated in **Figure 2-2 a** could be stretched globally with a serious of local displacement of the posts underneath. The cellular attribute detected using the method described in **Section 2.4**, **2.5**, or **Error! Reference source not found.** reflect the local responses to the

local mechanical stimuli via the displacement of the posts in the neighborhood. Meanwhile, the summation of these local responses reflects the whole-cell response to the global cell stretch.

In short, the CSD was designed with a circular viewing aperture surrounded by a vacuum chamber, with the stretchable micropost array membrane attached to the CSD, and the PDMS micropost array centered on the viewing aperture to permit visualization of the microposts under an optical microscope (**Figure 2-2 a**). The CSD was activated for cell stretch by applying a vacuum to draw the periphery of the PDMS basal membrane into the vacuum chamber, causing the central area of the stretchable micropost array membrane holding the PDMS micropost array to deform equibiaxially and the post c.t.c distance *S* to increase uniformly. Uniaxial cell stretching is also available by inserting two PDMS units into the annular vacuum chamber that divide the chamber into two symmetrical compartments where the basal membrane can deform and draw the central area with uniaxial deformation [191]. If not mentioned particularly, the results presented in the dissertation are drawn from equibiaxial cells stretching. The stretching magnitude of the stretchable micropost array membrane was adjusted by vacuum intensity that was controlled by customized LabVIEW program via digital vacuum regulator. The magnitude was easily determined *in situ* by utilizing the regularly positioned PDMS microposts as fiduciary markers to quantify their increased center-to-center distance (c.t.c) *S* under different levels of cell stretching (**Figure 2-2 c**).

To confirm that deformation of the stretchable micropost array membrane was indeed equibiaxial and spatially homogeneous over the entire PDMS micropost array, we applied different levels of static stretch to the stretchable micropost array membrane with the stretch magnitude ranging from 0% to 20%. Bright-field images of the PDMS microposts were taken

from eight different locations covering the entire micropost. Using the image processing program ImageJ, images were analyzed to determine the post c.t.c. distance *S* and the micropost diameter *D* at each of these eight locations before and after stretch. *S* varied by less than 2% among the eight different locations, regardless of the stretch magnitude, suggesting that the stretchable micropost array membrane stretch produced by the CSD was indeed homogeneous and equibiaxial over the entire micropost array. Similarly, regardless of the stretch magnitude, the diameter *D* of the top surface of the PDMS micropost, measured at the eight different locations, remained constant, indicating that the mechanical strain generated within the PDMS base membrane during the stretch did not propagate up the micropost to change the micropost geometry. Finite element analysis was also performed by us to confirm this point. We further examined the reliability of the stretchable micropost array membrane under static stretch conditions and cyclic stretch. Our data confirmed that the stretchable micropost array membrane could withstand a constant static stretch for at least 1 h under a broad range of stretch magnitudes from 0% up to 20%. For the cyclic stretch, it took about 10 sec for the membrane to stable after stretch, and up to the 1 min after a release; yet, repeated stretch did not show any residual strain accumulation. By doing so, we also obtained the calibration curve determining the relation between vacuum pressure and the stretch magnitude, thus helping us to decide the approximate vacuum pressure before measuring the c.t.c. distance *S*. (data not shown for the validation and calibration work.)

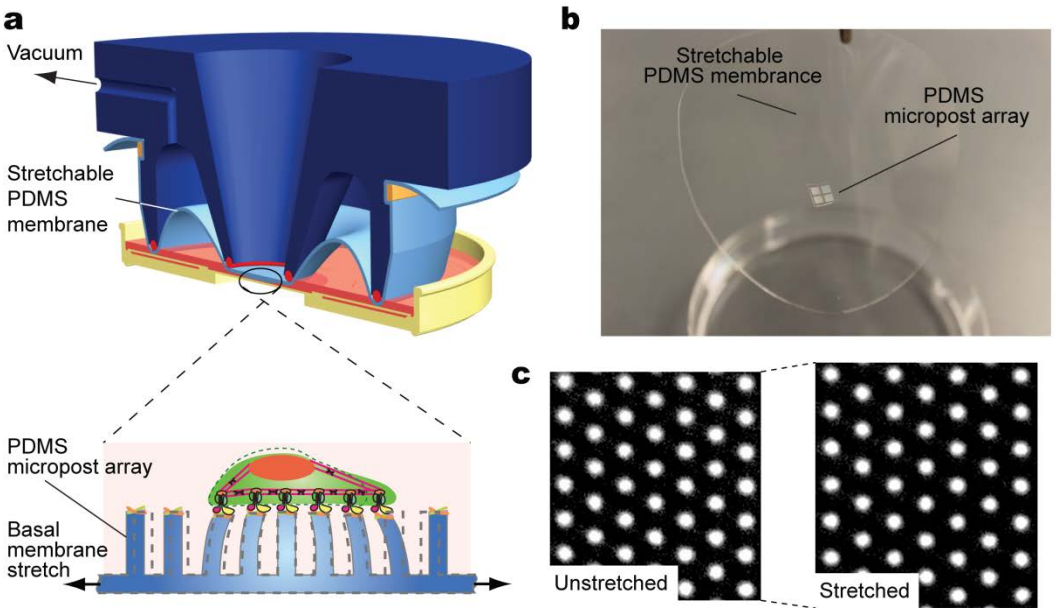

Figure 2-2 Experimental setup using stretchable PDMS micropost array to apply stretch to live cells. (**a**) Schematic of a custom-made, vacuum-driven cell stretching device (CSD), which contained a circular viewing aperture surrounded by a vacuum chamber. The stretchable micropost array membrane was inverted before mounted onto the CSD with the PDMS micropost array centered on the viewing aperture to permit direct visualization of live cells and PDMS microposts under microscopy. The CSD was placed inside a glass-bottom dish to facilitate high-resolution live-cell imaging. The CSD was activated for cell stretch by applying vacuum to draw periphery of the PDMS base membrane into the vacuum chamber, causing the central area of stretchable membrane holding the PDMS micropost array to stretch equibiaxially, thus the cells attached to the micropost array. The stretch magnitude was determined in situ by utilizing regularly positioned PDMS microposts as fiduciary markers. (**b**) Photo showing a PDMS stretchable micropost array membrane before mounted onto the CSD. (**c**) Fluorescent images showing the displacement of the microposts by the basal membrane stretch. The images were used to determine the stretch magnitude in situ.

In a summary, by leveraging the technique of traditional machining and microfabrication, we integrated the approaches for global cell stretching and local cell stretching, thus enabled us to study cell mechanics and mechanotransduction from both cellular scale and subcellular scale, which has not been shown clearly by the others. The unique potential of this system will be demonstrated in the rest of this dissertation. We have to admit that there are some restrictions of this device. For example, the stretching frequency cannot reach the physiologically relevant

range due to the media spill risk, and the limited field of view of the microscope restricted sample size.

2.4 Live-cell measurement of cytoskeleton tension, FA dynamics, and others with spatial registration

Cell contraction is a prediction for many life-sustaining mechanisms that play a major role in mammalian non-muscle cells [109, 172, 192-194]. Cell contraction is a mechanical contractile force exerted by the cells via mechanism including filament dynamics and its interaction with motor proteins to against forces from extracellular matrix (ECM) and the adjacent cells. The balance between all sources of forces determines the shape changes and movement of organelles, cells, and tissues [76-80].

Focal adhesion is a complex adhesive assembly through which actin cytoskeleton is linked to the ECM, and the intracellular forces from cell contraction and extracellular forces from ECM are transmitted between cell and ECM. Therefore, focal adhesion is the site where internal and external forces are converged. The complex of FA is not only full of structure proteins such as paxillin and vinculins that strengthen cell adhesion by mechanically anchoring the actin cytoskeleton to ECM via integrins, it also recruit many signaling proteins such as focal adhesion kinase (FAK) and Src involved in regulation of cell functions such as cell proliferation, migration, and survival, suggesting that FAs also function as organization centers for signaling cascades [195-198].

Moreover, the interplay between FA and forces are very complex [199]. The composition of FAs changes with cell contraction force on them. FA proteins such as integrin [200, 201] and vinculin [202], and talin [173, 203] changes conformation by force and are activated for FA growth and stabilization. Force-dependent recruitment of α-actinin, an actin crosslinking protein, facilitates force transmission through FA. Yet, tension alone is insufficient to drive FA maturation [204]. The complex interplay between FA and force demonstrated that force-dependent FA signaling plays a critical role in mechanosensing and mechanotransduction with diversified mechanosensitive signaling pathways.

Therefore, spatiotemporal regulation of cell contraction and FA signaling thus the downstream signaling pathways [205-207] is critical for developmental processes and disease progression [12, 13, 22, 109], and could be leveraged in tissue engineering and medicine. For example, YAP/TAZ, a transcriptional coactivator, has been shown in the studies of stem cell differentiation, cardiovascular system and cancer cells, sensitive to mechanical cues such as ECM rigidity, shear flow, and cyclic cell stretch [208-210]. Cell contraction and FAs are the obvious candidates that mediate the conversion of these mechanical cues into mechanosensitive phenotypes that are induced through YAP/TAZ activity. By using the PDMS micropost arrays described in **Section 2.2**, we developed an approach for neural induction from the human pluripotent stem cells and subtype specification that significantly improved purity and yield by controlling the mechanosensitive YAP/TAZ activities via the regulation of cell contraction and FA dynamics [143].

Quantitative analysis of cell contraction and FAs provides direct information on the mechanosensing and mechanotransduction showing how the cells response to the environmental

cues at the first step. Dynamic analysis of FAs is usually based on a series of fluorescent images showing clusters of FA complexes at different time points. Researchers usually set threshold from experience to remove the unavoidable background fluorescence, and analyze the protein turn over using fluorescent intensity quantitatively or the kymograph qualitatively. The results obtained depend highly on the image quality and the experience of the analyzers. Cell contraction can be measured directly from the deformation of the 2D or 3D substrate where cells are attached. Traction force microscopy is one of the most widely used techniques in which cells are cultured on natural or synthetic hydrogels imbedded with fluorescent microspheres [211-213]. The translational displacement field of the hydrogel is computed from a pair of fluorescent images showing the positions of the microsphere with and without cell attachment and cell-generated contraction. With a well-characterized mechanical behavior of the hydrogel, the stress filed and the cell contraction force can be calculated from the strain field. Method with similar ideas has been developed to measure cell contraction force in 3D hydrogel as well [193, 214, 215]. The approached mentioned about have been successfully applied for the study of force-mediated FA dynamics, rigidity sensing, cell migration, and etc.; however, it is difficult to decouple force and displacement in the continuous substrate with limited fluorescent markers, thus making it hard to calculate the force at particular adhesive sites. Moreover, most hydrogels are not purely elastic and may experience creep with load. The complicate mechanical characteristics of hydrogel also prevent the traction force microscopy from cell stretching assays [216].

Here, we used micropost, a discontinuous substrate for cell culture and an array of force sensors, where force on each post is calculated from the post displacement, and force and displacement do not propagate through the basal membrane. This technique has been used as an

alternative to the traction force microscopy to study the functional role of cell contraction in cell adhesion, migration, growth and differentiation of multicellular systems [117, 217-223]. For example, Ganz et al. examined adhesive forces exerted through N-cadherin mediated cell-cell contacts by immobilizing N-cadherin-Fc chimaera mimicking the cell adhesion molecule N-cadherin on the top surface of the microposts [217]. To investigate the functional correlation between cell-cell tugging force and adherens junctions (AJ) size, Liu et al. coated bowtie-like adhesive islands of fibronectin on microposts so that endothelial cells seeded on the microposts were constrained to the bowtie pattern with two cells forming cell-cell AJs [117]. In another research, Liang et al. applied the PDMS micropost array to measure contractile forces of platelets during aggregation and activation of microthrombi composed of many platelets [223]. Nelson et al. also attempted to culture a monolayer of the endothelial cell on the PDMS micropost array coated with asymmetric annulus shaped fibronectin patterns [219]. Nelson et al. observed that regions of concentrated cell growth corresponded to regions of cells with greater contractile forces generated within the monolayer.

In this study, micropost tops were functionalized for cell attachment with ECM proteins tagged with fluorophore. Fluorescent images of the micropost tops (**Figure 2-3 a** *blue* panel) were acquired at different time points for the measurement of cell contractile force map (**Figure 2-3 a** *yellow* panel) and its dynamic responses. We developed a customized MATLAB (Mathworks, Natick, MA) program for the quantitative analysis of subcellular contractile forces (see **Appendix B** for details) [88]. Briefly, positions of individual micropost tops were determined by two-dimensional (2D) Gaussian fitting, where 'windows' were drawn enclosing single posts and were adjusted to the center of the post tops. Post centroids calculated from the previous step were then refined by applying 2D Gaussian fitting again. Free-standing microposts

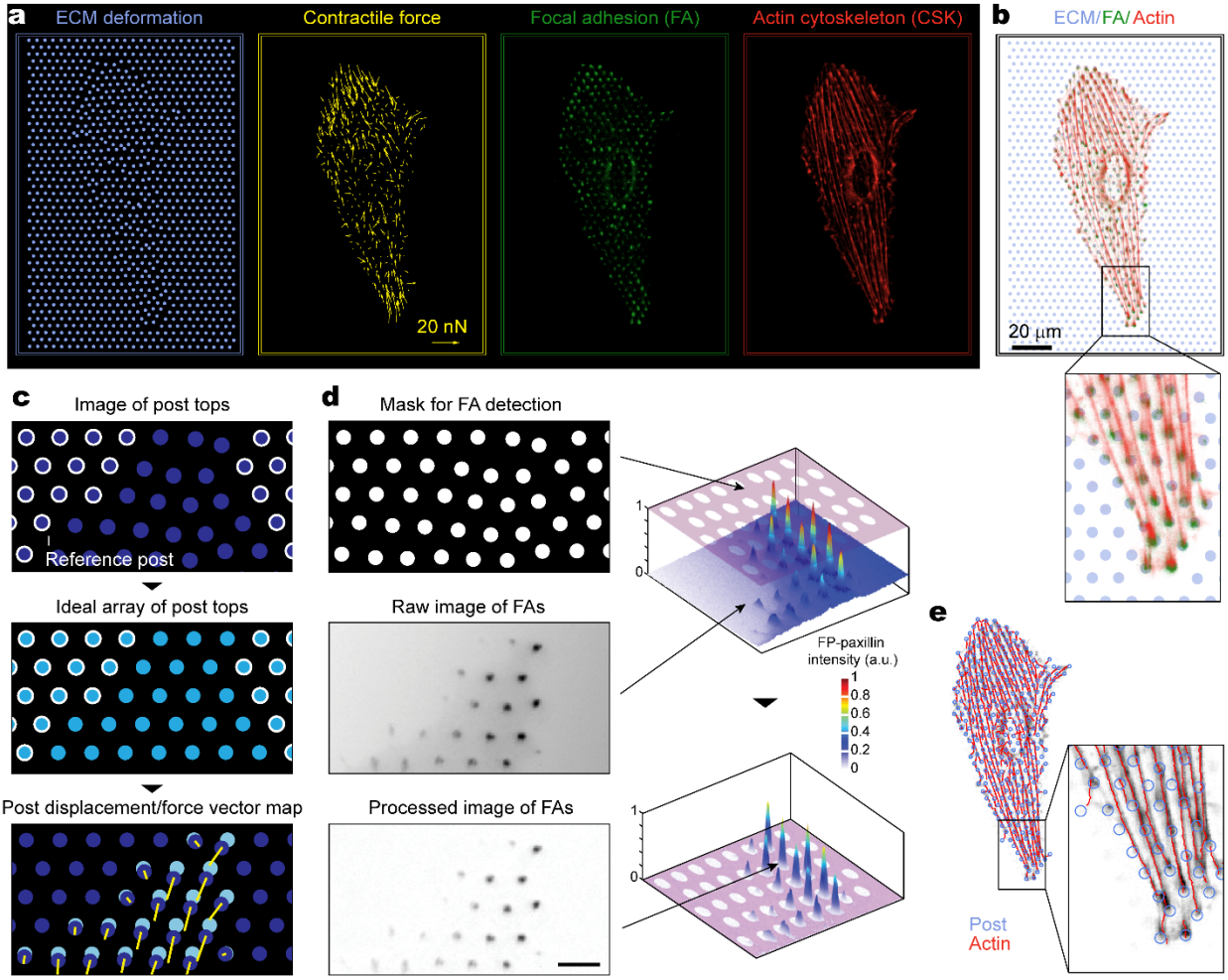

Figure 2-3 Live-cell imaging and image processing to characterize cell mechanics (**a**) Representative fluorescent and processed images showing the raw data extracted from live-cell imaging. The results of extracellular matrix (ECM) deformation, cytoskeleton (CSK) tension, focal adhesions (FAs), and actin CSK could be used further to quantify and characterize cell mechanics with and without extra physical and chemical stimulation. (**b**) Merged image from (**a**), showing localization of FAs (*green*) with ECM proteins (*light blue*) on top of posts and anchoring of actin stress fibers (*red*) to the posts (*light blue*) via FAs (*green*). (**c**) Image analysis to quantify CSK tension. Free-standing, unbent microposts (marked by white circles) in the fluorescent image of post tops (dark blue; top) were selected as reference posts to generate an ideal force-free post array (light blue; middle). Displacements of post tops from their unbent positions were then quantified and multiplied by the micropost spring constant to obtain CSK tension exerted on microposts (yellow force vectors; bottom). (**d**) Image analysis to quantify single FAs with spatial registration. Fluorescent image of post tops was converted into a binary image and was used as a mask for FA detection (top left). Local background fluorescence in the raw fluorescence microscopy of fluorescent protein (FP) tagged FA was subtracted using morphological opening (middle and bottom left). FA detection mask was then used to register each FA to individual single microposts (right). (e) Image analysis to detect single stress fibers (reconstructed in *red*) and spatial registration to the posts (*blue circles*).

without cell attachment were manually selected as reference posts to generate an ideal array of deflection-free microposts. Using undeflected 'free' posts as references, deflections of microposts underneath a cell were quantified and converted to horizontal traction forces (CSK tension) by multiplying post deflection with the nominal post spring constant K_{post} determined from finite element analysis (**Figure 2-3 c**).

The examination of FA dynamics takes advantage of the intrinsic discrete nature of the micropost arrays that determines the pattern of the adhesive ECM proteins and constrains the formation of FA complex on the micropost tops (**Figure 2-3 b**). The position of the micropost tops identified for the calculation of CSK tension is applied directly to position single FAs that facilitate quantitative analysis of FAs and other proteins co-localized with adhesive ECM proteins. For the fluorescent microscopy of live-cell FAs, we used rat embryo fibroblast cell line REF-52 stably expressing yellow fluorescent protein (YFP)-paxillin fusion protein that was a gift from Dr. Alexander D. Bershadsky, and human skin fibroblasts (HUSFs, gift from Dr. Gary J. Fisher) and human mesenchymal stem cells (HUMSCs; Lonza, Allendale, NJ) expressing green fluorescent protein (GFP)-paxillin fusion protein by infection cells with LentiBrite™ paxillin-GFP lentiviral biosensors (Millipore, Billerica, MA) (**Figure 2-3 a** *green* panel). The quantification of live-cell FA dynamics was achieved by continuously monitoring clustering of fluorescent protein (FP)-paxillin on micropost tops using a custom-developed MATLAB program (**Figure 2-3 d**). During image processing, local background fluorescence was first determined by performing morphological opening with a disk structure element of the same diameter as the PDMS micropost. Subtraction of background fluorescence was then conducted to extract FP-paxillin intensity in individual FAs localized on PDMS micropost tops. Compared with the conventional method of background subtraction that determines the threshold

manually, the algorithm used here is efficient and fully automatic to avoid producing artifacts. Instead of subtracting a uniformly distributed background, this algorithm determines and subtracts local background that prominently improves the signal-to-noise ratio where only the fluorescent signal from the clustered FA complex counts. This method also has the merit of easy spatial registration. The fluorescent image of PDMS micropost tops was converted to a binary image serving as a mask to detect individual FAs confined on micropost tops, thus registering each single FAs to subcellular CSK tension applied on the corresponding posts. Of note, individual circles in the FA detection mask were enlarged to 1.5 times the original post size to ensure full enclosure and thus accurate measurements of FAs. Total fluorescence intensity of FP-paxillin confined on individual micropost tops was quantified as the FP-paxillin intensity per FA or simply FA size.

The application of live-cell measurement of CSK tension and FAs is described in detail in **Chapter 3**. Of note, application of this algorithm can be extended to examine dynamics of other FA proteins such as talin and vinculin and signaling proteins such as focal adhesion kinase (FAK) that colocalize at the adhesive sites. A similar idea is also employed to spatially register the actin stress fibers. As shown in **Figure 2-3 b**, FAs are also the anchoring points through which the actin stress fibers are linked to the ECM. Therefore, the underneath microposts can be assigned to the detected actin stress fibers as spatial markers (**Figure 2-3 e**). In short, we first transfected the cells with LifeAct lentivirus (Ibidi, Planegg / Martinsried, Germany) that enabled visualization of F-actin. We have developed computational algorithm to detect single stress fibers and digitize them. We first reduced the background of the original fluorescent images of actin network, and found the ridge areas where the fluorescent intensity reached its local maximum. By applying a series of image filters to reduce the sprouts and remove false positive

areas, we converted the ridge images into skeleton images where each line represented a single bundle of actin filaments. Later on, morphological analysis was performed on the skeleton images so that all disconnected lines were digitized with the location information. Then, the posts (**Figure 2-3 e** *blue circles*) close to the stress fibers (**Figure 2-3 e** *red lines*) could be assigned to them. The algorithm used so far do not retain the information about width and intensity of single stress fibers in the image processing, which could be a major lost for studying the dynamic remodeling of actin network. Future work will focus on solving this issue.

Together, taking the advantage that micropost arrays regulate the sites for FA formation through which cells are attached to the ECM, micropost array-based live-cell measurements of CSK, CSK tension, and FAs are highly automatic with spatial resolution using purely live-cell imaging and image processing. It enabled the study of force-mediated mechanotransduction where the essential components including structural and functional proteins as well as the co-localized cell contraction can be measured and analyzed with spatial registration.

2.5 Measurement of cell stiffness with subcellular resolution

Besides cell contraction and adhesive properties, cell stiffness is another important mechanical attribute that indicate the physiological and pathological changes in cells [49, 175, 224-229]. For example, alteration in cancer cell stiffness is a hallmark of cancer metastasis. Reduced cell stiffness likely as a result of perturbed cytoskeleton have significant effect on cell ability to squeeze through the surround tissue and intravasate into blood vessel. Experimental results from indentation tests and microfluidic deformation assays have demonstrated that cancer

cells are softer than the normal cells from the same sources, and invasive phenotype is softer than the less-invasive phenotype [224-226]. Recently, there also evidence showing that the hardening of vascular wall in hypertension is not only attributed by the changes in extracellular matrix proteins, but also mediated by the altered stiffness of individual vascular smooth muscle cells, where expression of actin, phosphorylated myosin light chain and myosin light chain kinase (MLCK) were found to be increased at least two fold compared with the normotensive controls [230].

Cell stiffness is correlated with cell contractility, remodeling of cytoskeleton, and signaling in mechanotransduction [49, 224, 231, 232]. However, this widely accepted knowledge have not been shown in detail how spatiotemporal distribution of stress fiber, cell contraction, and signaling molecules directly modulate cell stiffness. Although the technique of AFM is capable of measure cell stiffness in different subcellular regions, which is important for understanding spatial variation and correlation with adhesive and cytoskeleton structures in mechanoresponsive adaptation and the emergent of cellular mechanics with the bottom-up processing, it is not compatible with other techniques to apply global mechanical perturbation in this study. To address the knowledge gap and solve the technical problem, we have recently applied the cell stretching device in conjunction with a finite element method to achieve whole-cell cell stiffness measurements with a subcellular spatial resolution [87].

The finite element analysis of cell stiffness using the stretchable micropost array cytometry leverages the intrinsic discrete nature of the PDMS micropost arrays that is arranged in a hexagonal pattern [87]. Thus, the individual cells adhered to the tops of PDMS micropost arrays are automatically discretized by a mesh of triangles. Before cell stretch, each node *i* of the

triangular mesh, which is located on top of a micropost, has its position vector (x_{it}, y_{it}) and a corresponding post base position vector (x_{ib}, y_{ib}). The force vector (f_{ix}, f_{iy}) on the node *i* is the reaction force to the action force bending the underlying post, and can be expressed as $f_{ix} = K_p \cdot (x_{ib} - x_{it})$ and $f_{iy} = K_p \cdot (y_{ib} - y_{it})$, where K_p is the spring constant of the PDMS post. Immediately after cell stretch, new sets of vectors are obtained, including node position vectors (X_{it}, Y_{it}), position vectors of the corresponding post bases (X_{ib}, Y_{ib}), and force vectors (F_{ix}, F_{iy}), where $F_{ix} = K_p \cdot (X_{ib} - X_{it})$, $F_{iy} = K_p \cdot (Y_{ib} - Y_{it})$. Thus, by subtracting the initial node position and force vectors from those after stretch, respectively, we can obtain the post top displacement (u_{ix}, u_{iy}) and the change of CSK tension (df_{ix}, df_{iy}) of each node (**Figure 2-4**). For the finite element analysis of a small triangular element whose vertices are located on top of three neighboring microposts, the displacement vectors and the force vectors are combined with the expression $\boldsymbol{u} = [u_{1x}, u_{1y}, u_{2x}, u_{2y}, u_{3x}, u_{3y}]$ and $\boldsymbol{df} = [df_{1x}, df_{1y}, df_{2x}, df_{2y}, df_{3x}, df_{3y}]$, respectively, where index $i = 1$, 2, and 3 identify the nodes in a counterclockwise order. The relation between $\boldsymbol{u}$ and $\boldsymbol{df}$ can be expressed as

$$\begin{bmatrix} df_{1x} \\ df_{1y} \\ df_{2x} \\ df_{2y} \\ df_{3x} \\ df_{3y} \end{bmatrix} = \frac{AE_h}{1-\nu^2} B^T \begin{bmatrix} 1 & \nu & 0 \\ \nu & 1 & 0 \\ 0 & 0 & (1-\nu)/2 \end{bmatrix} B \begin{bmatrix} u_{1x} \\ u_{1y} \\ u_{2x} \\ u_{2y} \\ u_{3x} \\ u_{3y} \end{bmatrix} \tag{2.1}$$

where

$$B = \frac{1}{2A}\begin{bmatrix} y_{2t}-y_{3t} & 0 & y_{3t}-y_{1t} & 0 & y_{1t}-y_{2t} & 0 \\ 0 & x_{3t}-x_{2t} & 0 & x_{1t}-x_{3t} & 0 & x_{2t}-x_{1t} \\ x_{3t}-x_{2t} & y_{2t}-y_{3t} & x_{1t}-x_{3t} & y_{3t}-y_{1t} & x_{2t}-x_{1t} & y_{1t}-y_{2t} \end{bmatrix} \tag{2.2}$$

and

$$A = \frac{1}{2}\begin{Vmatrix} 1 & 1 & 1 \\ x_{1t} & x_{2t} & x_{3t} \\ y_{1t} & y_{2t} & y_{3t} \end{Vmatrix} \tag{2.3}$$

E_h stands for the product of the finite element's *Young's* modulus and its height, and v is its *Poisson*'s ratio. The relations described by Equation (2.1) for all triangular elements within the cell area are combined into a global matrix form as

$$\boldsymbol{dF} = \boldsymbol{S}(\boldsymbol{E}_h, \boldsymbol{v})\cdot\boldsymbol{U} \tag{2.4}$$

where the global force matrix $\boldsymbol{dF}$ and the global displacement matrix $\boldsymbol{U}$ are acquired as described previously, and the matrices of $\boldsymbol{E}_h$ and $\mathbf{v}$ are the unknown parameters of the subcellular triangular elements that we will solve numerically.

It is worth noting that as $\boldsymbol{E}_h$ and $\mathbf{v}$ are defined on each finite element, the total number of unknown variables is twice the number of elements, while the total number of the equations in Equation (2.4) is twice the number of nodes. Since the number of elements is usually greater than the number of nodes, additional constraints are added to make the problem numerically solvable. We assumed that the neighboring elements sharing the same horizontal edges have same cell stiffness and *Poisson*'s ratio.

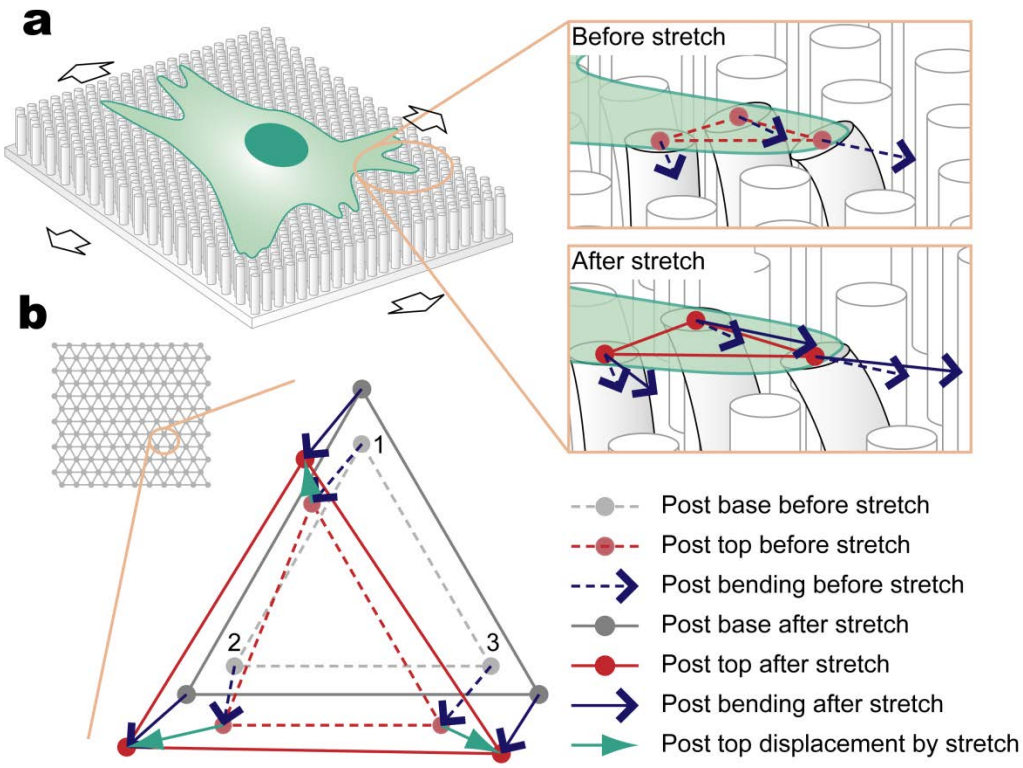

Figure 2-4 Measurement of subcellular cell stiffness using the stretchable micropost array cytometry (SμPAC). (**a**) Schematic of the micropost array-based subcellular discretization, and the change of the post position and post bending in response to stretch. (**b**) Schematic of the micropost array-based grid and elements for the finite element analysis.

With optimized $\boldsymbol{E}_h$ and $\boldsymbol{\nu}$, we can further calculate the whole-cell average *Young's* modulus, E_{ave}, and *Poisson*'s ratio, ν_{ave}, of an entire single cell. E_{ave} and ν_{ave} are obtained by averaging over all grid elements, *i.e.* $E_{ave} = \sum(E_h A)/(4\pi R^3)$ and $\nu_{ave} = \sum(\nu A)/\sum A$, where R is the radius of the cell in a suspended state.

We applied this technique to characterize subcellular cell stiffness of live single vascular smooth muscle cells (VSMCs). We treated cells with blebbistatin (myosin II inhibitor, 100 μM), Y27632 (Rho-associated protein kinase (ROCK) inhibitor, 10 μM), and cytochalasin D (actin polymerization inhibitor, 40 μM) to block myosin II and ROCK activities and actin

polymerization, respectively. We observed that the whole-cell average *Young*'s, E_{ave} of drug-treated live cells was significantly less than the value measured of untreated control cells, confirming the critical involvements of actin network and myosin II-mediated actomyosin contraction in regulating mechanical stiffness of VSMCs. Interestingly, cell stiffness of VSMCs treated with blebbistatin and Y27632 deceased more as compared to the cells treated with cytochalasin D, again highlighting the importance of cell contraction in mediating cell stiffness [87].

By leveraging what we have developed in the previous sections, we explored the potential of the stretchable micropost array system and achieved the live-cell measurement of cell stiffness with subcellular resolution, without utilizing any other equipment. As a proof of concept, we have demonstrated its feasibility in the measurement of subcellular cell stiffness and whole-cell stiffness, and the experimental results have highlighted the mediatory role of cell contraction and cytoskeleton on the regulation of cell stiffness. The spatiotemporal regulation between cell stiffness, cytoskeleton, adhesion and contraction is part of the future work that is described in **Section 5.3**.

2.6 Summary

Pulling together the techniques described in this Chapter, we developed a unique tool termed micropost array cytometry. It can apply global mechanical perturbations to live single cells via regularly positioned local probes, while acquiring cellular responses with a subcellular resolution in real time. By comparing whole-cell responses to subcellular activities, it may help

elucidate how single cell-level behaviors emerge from complex yet organized subcellular dynamics. Leveraging the unique capability of the micropost array cytometry, we have successfully characterized cell contractile force, cell stiffness, and FA dynamics at both whole-cell and subcellular scales in real time. Future work described in **Section Error! Reference source not found.** brings in cytoskeleton into the system and will characterize the dynamic spatial connection between cell contraction, cell adhesion, cytoskeleton, cell stiffness, with more physiologically relevant mechanical stimulation such as cyclic stretch.

Although the applications of the micropost array cytometry demonstrated in this dissertation have been carried out using a custom designed cell stretching device for live single cells, the micropost array cytometry is versatile to be integrated with many other molecular and cell mechanics tools for investigating different cell mechanics and mechanobiology questions in various contexts. The technique of micropost array cytometry can also be implemented with other types of tissue cultures to study mechanobiology beyond the cellular scale. For example, a two-cell pair model [117] can be used with the micropost array cytometry to study the cell-cell interaction, an epithelial monolayer model can be applied to study the mechanotransduction in collective cell migration, and a stem-cell colony model [233]can be applied to study the mechanosensitive pattern formation in embryonic development. The micropost array cytometry can also be implemented with other techniques to apply external mechanical stimulation or perturbation such as microfluidic devices to apply shear flow [145] and magnetic wire imbedded in the microposts to apply local mechanical stretch directed on FAs [147]. In addition, it will also be exciting to combine the micropost array cytometry with dynamic molecular manipulation tools such as optogenetics [234], to locally activate cell contraction by activing RhoA, for example, to study how the intracellular mechanical perturbation is tackled with.

To conclude, with the micropost array cytometry and other biochemical techniques, we are able to perturb surface receptors, ion channels, cell-ECM interaction, and cell-cell interaction, and observe the spatiotemporal regulation of cytoskeleton, focal adhesion, contraction, and nucleus, which enable the study of mechanotransduction from mechanical stimulation, force sensing, signal transduction, gene expression, cell function, and the emergent properties of cells (**Figure 1-1**).

Chapter 3

Mechanosensitive subcellular rheostasis drives emergent single-cell mechanical homeostasis

The major content of this chapter is reproduced from our previously published paper: "Mechanosensitive subcellular rheostasis drives emergent single-cell mechanical homeostasis" in *Nature Materials*, 2016[88].

3.1 Introduction

Over the last decades, there have been growing interests in mechanobiology and mechanotransduction. With a substantial amount of evidence, it has become increasing clear that physical forces and changes in cell mechanics contribute to development, physiology, and diseases. For example, cyclic stretches to cardiomyocytes and smooth muscle cells due to heart beating regulate their rhythmic contraction and are closely related to the tissue hardening and aging [156-160]. Transient stretch to fibroblasts in the joints triggers signaling events regulating extracellular matrix (ECM) protein deposition [164-167]. Shear stress on endothelial cells by blood flow affects cellular functions including permeability, maturation, remodeling, and inflammatory responses [161-163]. Changes on physical forces also arise as a result of processes

such as local cell death, growth, and division [235]. As a most remarkable example, continuous cell division together with differentiation in the embryo development drives morphogenetic movement where adjacent cells squeeze and push each other during gastrulation and neural tube formation [31-34]. In these mechanically active environment, if not dealt with, the accumulation of stress and strain, and the resulting tissue deformation can pose a significant challenge to tissue integrity and structures, leading to diseases like the developmental defects. Therefore, it is critical to understand how and when a stable cell/tissue physiology could be maintained against intrinsic and extrinsic mechanical perturbations, the process of which is termed mechanical homeostasis (**Figure 3-3 a**).

Considerable studies have been devoted to answering this question and mechanisms acting on different time and length scales have been reported to guide cell and tissue homeostasis or adaptation to the applied stress [236]. Within seconds, the poroelastic responses of cells arise from cytosol redistribution through the dense meshwork of cytoplasmic fibers (cytoskeleton) and organelles as an instantaneous response to the external forces [237, 238]. Soon after that, the stress bearing structures such as actin stress fibers join in where disassembly of stress fibers leads to a relaxation of stress and assembly of stress fibers leads to reinforcement [239]. Between minutes to an hour, significant remodeling of cytoskeleton network and cell shape change associated with various patterns of cell contraction may occur to change cell neighbors, orient cell division along the axis of external forces, or extrude cells from its niche [240-246]. In a longer term, morphological changes of tissues are usually observed as a consequence of the constitutive mechanical load [247]. All of these mechanisms redistribute stress and release strains in cells and tissues, hence driving cells to a previous or new steady state [236].

It is clear that the spatiotemporal control of the underlying mechanotransduction severs to maintain the intracellular homeostasis in the face to variations in the extracellular microenvironment, especially the mechanical stimuli due to tension and compression [13, 248-250]. However, it remains unclear how distinctive mechanisms of mechanical homeostasis are employed and coordinated during cellular processes with time and length scales spanning many orders of magnitude, such as morphogenesis. Current finding using different cells and different testing systems have shown divergent results of cellular responses under cell stretching. For example, Webster et al. showed that responses of cell contraction was strain rate-dependent and homeostasis was only observed when the rate of cell stretch was very low [96]. Krishnan et al. and Chen et al. found that cells after a transient stretch experienced an apparent fluidization followed by a reinforcement, but mechanical homeostasis was cell type-dependent [97, 251]. In another work, Chen et al. specifically studied the response of single FAs when cells were stretched uniaxially, and found that FA dynamics could be orientation-specific [252]. These studies have demonstrated that finding at both cellular and subcellular scale provide unique insight into processes of mechanical homeostasis and imply the necessity for a multiscale and systematic analysis of this phenomenon. Therefore, rather than focusing on the molecular machineries or phenotypical and morphological changes of cells separately, the motivation of this work is to bridge the gap between the subcellular events and the resulting cellular responses. Specifically, we applied a sustained stretch to a cell and examined its mechanical responses from both cellular and subcellular scales, and we investigated how emergent single-cell properties were determined by collective dynamics at subcellular scale.

3.2 Experimental methods

3.2.1 Cell culture and reagents

Both rat embryo fibroblast cell line REF-52 stably expressing yellow fluorescent protein (YFP) -paxillin fusion protein (gift from Dr. Alexander D. Bershadsky) and human skin fibroblasts (HUSFs; gift from Dr. Gary J. Fisher) were maintained in high-glucose Dulbecco's modified Eagle's medium (DMEM; Invitrogen) supplemented with 10% fetal bovine serum (FBS; Invitrogen), 4 mM L-glutamine (Invitrogen), 100 units mL^{-1} penicillin (Invitrogen), and 100 μg mL^{-1} streptomycin (Invitrogen) at 37°C and 5% CO_2. Human mesenchymal stem cells (HUMSCs; Lonza, Allendale, NJ) were maintained in MesenPRO RS™ medium (Invitrogen) at 37°C and 5% CO_2. LentiBrite™ paxillin-green fluorescent protein (GFP) lentiviral biosensors (Millipore, Billerica, MA) were transduced into HUSFs and HUMSCs at multiplicity of infection (MOI) of 50 - 80 according to manufacturer's protocol. CellLight® actin-RFP construct (Invitrogen) was transfected into REF-52 fibroblast cells at particles per cell (PPC) of 60 according to manufacturer's protocol.

When cells became 90% confluent, cells were washed twice with PBS and incubated with 0.25% trypsin-EDTA solution (Invitrogen) for 2 min for cell re-suspension. Single REF-52 fibroblasts, HUSFs, and HUMSCs were seeded at a density of 8,000 cells cm^{-2}, 4,000 cells cm^{-2}, and 2,000 cells cm^{-2}, respectively, on the stretchable micropost array membrane (**Figure 2-2**) and were allowed to spread out for at least 6 hr before cell stretch assays. To reduce background fluorescence, phenol red-free growth medium (Invitrogen) was used during live-cell fluorescence imaging.

To perturb the actin cytoskeleton in REF-52 fibroblasts, small-molecule inhibitors targeting the cytoskeleton integrity and tension, including 50 nM nocodazole (Sigma-Aldrich), which depolymerizes microtubules and impedes FA disassembly[253]; 10 μM blebbistatin (Cayman Chemical, Ann Arbor, MI), which inhibits myosin motor activity and thus CSK tension[254]; 10 nM jasplakinolide (Cayman Chemical), which enhances actin polymerization[255]; and 200 nM cytochalasin D (Tocris bioscience, Bristol, UK), which blocks actin polymerization[256], were supplemented to cell growth medium for 2 hr prior to cell stretch assays. Dosages of the inhibitors were optimized by titration to minimize their off-target effects on cell area, focal adhesion (FA) size, CSK tension, and actin CSK architecture (**Figure 3-1**). Of note, although the low dosage of cytochalasin D applied in this study still appeared to affect cell mechanobiological states (phenotypes), significant portions of FAs, the actin CSK, and CSK tension were still remained to support our investigations of the roles of the CSK integrity and tension on single-cell mechanical homeostasis and subcellular rheostasis.

To modulate the catch-slip bond property of integrin-fibronectin bond for HUMSCs, anti-human integrin β1 antibody TS2/16 (Santa Cruz, Dallas, TX) was added to cell growth medium at 5 μg mL^{-1} for 2 hr prior to cell stretch assays.

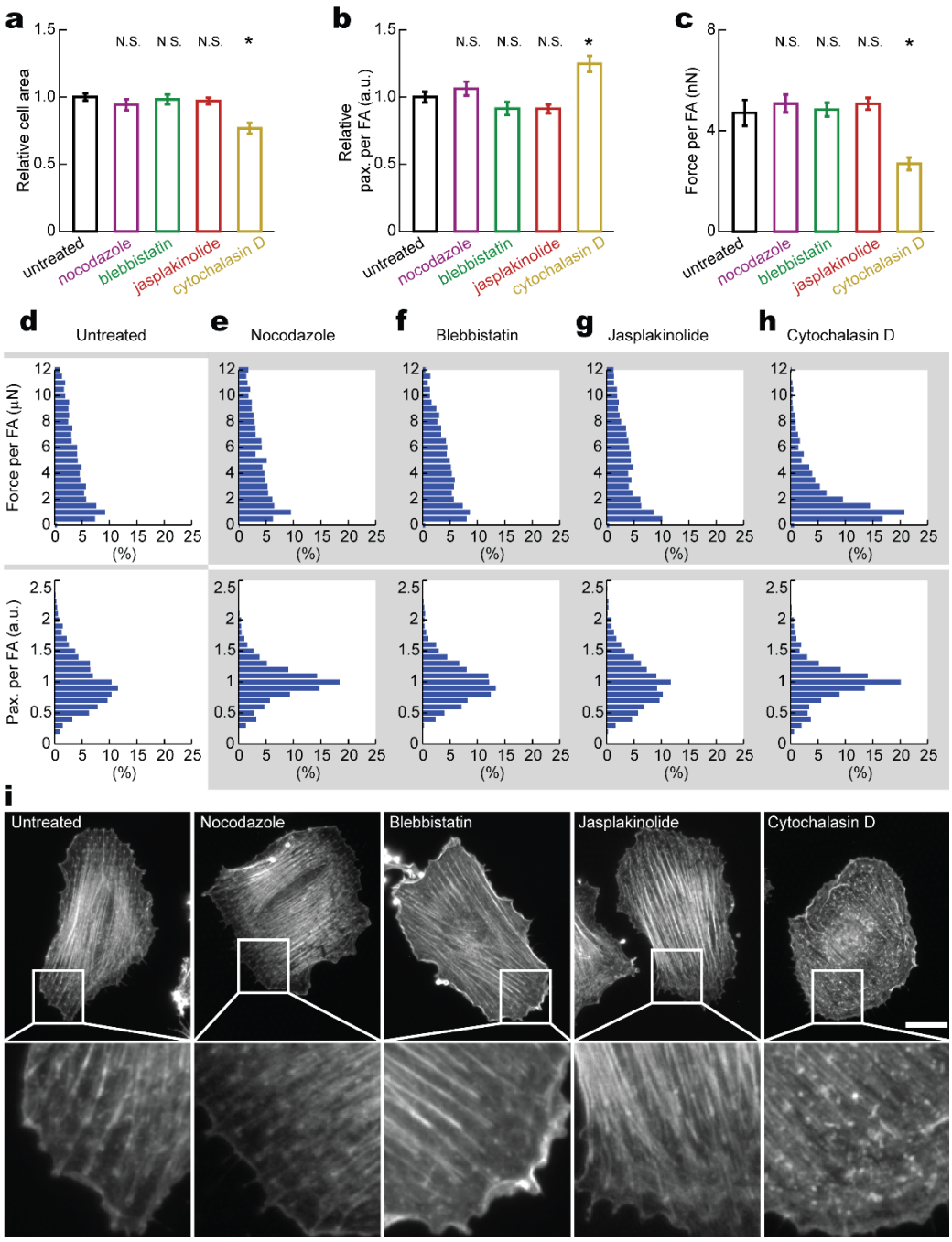

Figure 3-1 Effect of treatments with low-dosage pharmacological small-molecule inhibitors. Changes of cell spread area (**a**), focal adhesion (FA) formation (**b**, **d-h**), cytoskeleton (CSK) tension (**c**, **d-h**), and actin cytoskeleton architecture (**i**) for REF-52 cells were measured and analyzed. Drug dosages: nocodazole, 50 nM; blebbistatin, 10 μM; jasplakinolide, 10 nM; cytochalasin D, 200 nM. Data in **a** and **b** was normalized to values obtained for untreated controls. Data represents the mean ± s.e.m with n = 10. P-values were calculated using student's paired sample t-test comparing drug treated cells with untreated control. N.S., statistically not significant and $P > 0.05$. *, $P < 0.05$. (**d-h**) Distribution of subcellular CSK tension (top) and FA size (bottom)

for untreated and drug-treated REF-52 cells as indicated. For each condition, data from 10 cells and over 2,000 FAs was pooled and analyzed. (**i**) Representative fluorescence microscopy images showing effects of small-molecule inhibitors on the actin CSK architecture of REF-52 cells. Images at the bottom are magnifications of the boxed regions in the top images. REF-52 cells seeded on the stretchable micropost array membrane were fixed and stained with fluorescently labeled phalloidin. Untreated REF-52 cells and those treated with low dosages of nocodazole, blebbistatin, and jasplakinolide were all well spread with prominent, highly organized actin stress fibers. Compared to untreated control, REF-52 cells treated with cytochalasin D had smaller cell spreading and less organized and somewhat punctuated actin filaments. Nonetheless, we should note that there were still plenty visible actin stress fibers connected to FAs with measurable CSK tension. Scale bar, 20 μm.

3.2.2 Cell stretching assay

A custom-made, vacuum-driven cell stretching device (CSD) was developed for stretching the stretchable micropost array membrane as described in **Section 2.3** (**Figure 2-2**)[257]. For cell stretch assays, cells were first seeded onto the stretchable micropost array membrane and cultured for at least 6 hr, before the stretchable micropost array membrane was inverted and mounted onto the CSD and submerged in pre-warmed culture medium inside a glass-bottom dish to facilitate high-resolution live-cell imaging. The PDMS micropost array on the stretchable micropost array membrane was centered on the viewing aperture of the CSD to permit direct visualization of microposts under microscopy. The CSD was connected to a portable vacuum generator (Vacu-Cell Vacuum System, C&L Instruments, Hershey, PA) or in-house vacuum via a vacuum regulator (Airtrol, New Berlin, WI) to control the onset and magnitude of vacuum. The CSD was activated for cell stretch by applying vacuum to draw periphery of the PDMS basal membrane into the vacuum chamber, causing the central area of the stretchable micropost array membrane holding the PDMS micropost array to stretch equibiaxially (**Figure 2-2 c**). Stretch magnitude of the stretchable micropost array membrane was determined by utilizing regularly positioned PDMS microposts as fiduciary markers.

During cell stretch assays, each single cell was continuously monitored for 15 min prior to cell stretch (**Figure 3-3 b**). At the onset of stretch, a rapid 4%, 8%, or 16% step increase of cell stretch was applied and was held constant for another 30 min (**Figure 3-3 b**).

3.2.3 Fluorescence imaging

Live-cell fluorescence imaging was performed using a monochrome charge-coupled device (CCD) camera (AxioCam, Carl Zeiss MicroImaging, Thornwood, NY) attached to an inverted epi-fluorescence microscope (Zeiss Axio Observer Z1, Carl Zeiss Microimaging) enclosed in an environmental incubator (XL S1 incubator, Carl Zeiss MicroImaging) maintaining cell culture at 37°C and 5% CO_2. Images of micropost tops, FAs containing fluorescent protein (FP)-paxillin fusion proteins, and/or RFP-fused actin were recorded using a 40× EC Plan-Neofluar objective (NA 0.75, Ph2, Carl Zeiss MicroImaging) (**Figure 2-3 a**). Upon stretch, the basal PDMS membrane of the stretchable micropost array membrane inevitably generated vertical deformation causing out-of-focus movements of cells cultured on the microposts, which was corrected manually by re-adjusting focal plane within 10 sec after the onset of stretch.

3.2.4 Quantitative analysis of cytoskeleton tension and focal adhesion

Quantitative analysis of subcellular CSK tension and focal adhesions was performed using the methods described in **Section 2.4**. Briefly, quantitative analysis of subcellular CSK tension was first performed using a custom-developed MATLAB program (Mathworks, Natick, MA) (**Figure 2-3 b**)[258]. Briefly, individual micropost tops were determined by two-

dimensional (2D) Gaussian fitting, where 'windows' were drawn enclosing single posts and were adjusted to center the post tops. Post centroids calculated from the previous step were then refined by applying 2D Gaussian fitting again. Undeflected microposts without cell attachment were manually selected as reference posts to generate an ideal array of force-free microposts. Using undeflected 'free' posts as references, deflections of microposts underneath a cell were quantified and converted to horizontal traction forces (CSK tension) by multiplying post deflection with the nominal post spring constant K_{post}.

Dynamics of FA was examined by continuously monitoring clustering of fluorescent protein (FP)-paxillin on micropost tops (**Figure 2-3 b,c**). During image processing, background fluorescence was first determined through performing morphological opening with a disk structure element of the same diameter as the PDMS micropost. Subtraction of background fluorescence was then conducted to extract FP-paxillin intensity in individual FAs localized on PDMS micropost tops. To spatially register each single FA to CSK tension, fluorescent image of PDMS micropost tops was converted to a binary image serving as a mask to detect individual FAs confined on micropost tops. It should be noted that individual circles in the FA detection mask were enlarged to 1.5 times the original post size to ensure full enclosure and thus accurate measurements of FAs. Total fluorescence intensity of FP-paxillin confined on individual micropost tops was quantified as the FP-paxillin intensity per FA or simply FA size.

3.2.5 Compensation of fluorescence quenching

Calibration curves for different fluorescent proteins and cell stretch levels were obtained to compensate fluorescence quenching due to photo-bleaching and light path variation caused by cell stretch (**Figure 3-2 a&b**). Briefly, cells seeded on the stretchable micropost array

membrane were washed twice with PBS before fixed with 4% paraformaldehyde (PFA; Electron Microscopy Sciences, Hatfield, PA) in a CSK buffer (10 mM PIPES, 100 mM sodium chloride, 300 mM sucrose, 3 mM magnesium chloride, and pH adjusted to 6.9; Sigma-Aldrich) for 30 min. Cells were then washed twice with PBS before permeabilization with 0.1% Triton X-100 (Sigma-Aldrich) for 10 min. Cell stretch assays were conducted on fixed cells to obtain total FP-paxillin intensity in each single cell as a function of time, using the same data acquisition frequency (sampling rate) as used in live-cell experiments. Two exponential functions were then used for best fitting of the decay of total FP-paxillin intensity in single cells before and after the onset of cell stretch, respectively (**Figure 3-2 c**). These exponential functions were utilized as calibration curves for compensating fluorescence quenching in live-cell assays.

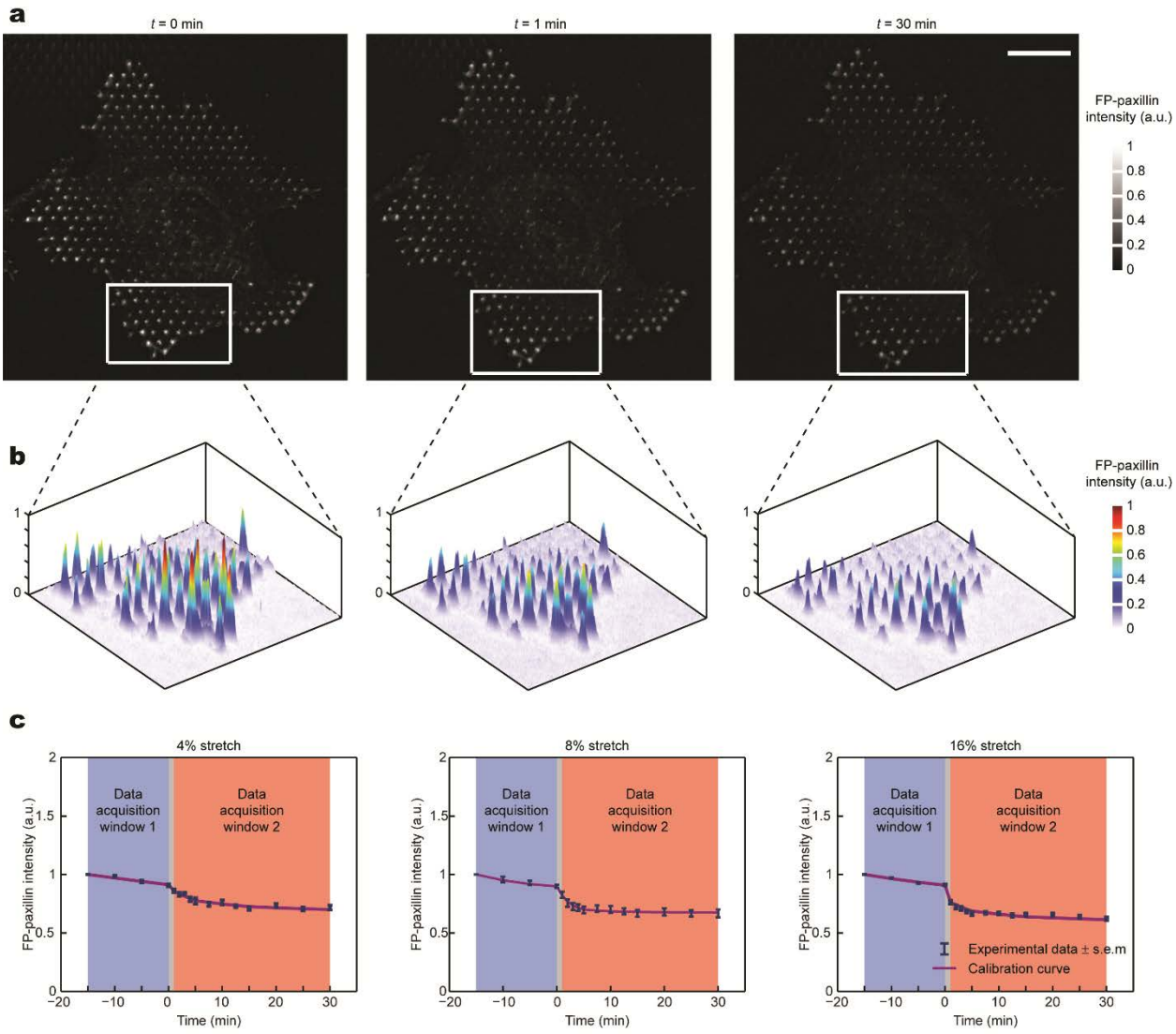

Figure 3-2 Compensation of fluorescence quenching. Due to photobleaching and light path variation caused by cell stretch, fluoresce quenches. To quantify fluorescence quenching, FP-paxillin expressing cells seeded on the stretchable micropost array membrane were fixed before assayed using the same static equibiaxial stretch protocol shown in **Figure 3-3b**. (**a&b**) Representative fluorescence microscopy images (after background fluorescence subtraction) of FP-paxillin (**a**) and corresponding 3-D colorimetric heat maps (**b**) before (t = 0 min) and after the onset of 8% static equibiaxial stretch (t = 1 min and t = 30 min), showing noticeable decay of fluorescence intensity due to non-specific effects of fluorescence quenching caused by photobleaching and light path variation resulted from cell stretch. (**c**) Calibration curves for fluorescence quenching of YFP-paxillin intensity during cell stretch assays at the stretch levels of 4%, 8%, and 16% as indicated. Under each stretch level, normalized whole-cell YFP-paxillin intensity as a function of time was best fitted with two exponential functions (purple curves), serving as a calibration curve for compensating fluorescence quenching for live-cell assays. Note that whole-cell YFP-paxillin intensity was normalized to values obtained at the beginning of cell stretch assays (t = -15 min). Data represents the mean ± s.e.m with n = 10.

3.2.6 Cross-correlation analysis between cytoskeleton tension and focal adhesion

Dynamic synchronization between subcellular FAs and their associated CSK tension was evaluated using cross-correlation analysis[259]. Linear interpolation was first conducted to achieve a constant sampling frequency for FA size and CSK tension data sets while increasing the sampling resolution to 0.1 min. Refined data sets of CSK tension and FA size were denoted as *A* and *B*, respectively, with indices from 1 to N corresponding to the time t from -15 min to 30 min with an interval of 0.1 min. Since FA size *B* was relatively stable at both the beginning and the end of cell stretch assays, the FA size data set *B* was extended below t = -15 min and beyond t = 30 min using its steady-state values at t = -15 and 30 min, respectively, for cross-correlation analysis. Specifically, for the extended FA size data set B_e, $B_e(1) = B_e(2) = \cdots = B_e(\mathrm{N}-1) = B_e(\mathrm{N}) = B(1)$, $B_e(\mathrm{N}+1) = B(1)$, $B_e(\mathrm{N}+2) = B(2)$, $\cdots$, $B_e(2\mathrm{N}-1) = B(\mathrm{N}-1)$, $B_e(2\mathrm{N}) = B(\mathrm{N})$, and $B_e(2\mathrm{N}+1) = B_e(2\mathrm{N}+2) = \cdots = B_e(3\mathrm{N}-1) = B_e(3\mathrm{N}) = B(\mathrm{N})$, wherein $B(1)$ and $B(\mathrm{N})$ were the steady-state FA values at t = -15 and 30 min, respectively. Discrete cross-correlation $CC(\mathrm{i})$ and discrete normalized cross-correlation $NCC(\mathrm{i})$ between the CSK tension data set *A* and the FA size data set *B* were calculated as $CC(i) = \sum_{k=1}^{N} A(k) \cdot B_e(i+k-1)$ and

$NCC(i) = CC(i) \Big/ \sqrt{\sum_{k=1}^{N} A^2(k) \cdot \sum_{k=1}^{N} B_e^2(i+k-1)}$, respectively, where index i ranged from 1 to 2N+1, corresponding to the time axis t from -45 min to 45 min with an interval of 0.1 min. Discrete cross-correlation $CC(\mathrm{i})$ and discrete normalized cross-correlation $NCC(\mathrm{i})$ were further converted to $CC(\mathrm{t})$ and $NCC(\mathrm{t})$, respectively, where the greatest value of $NCC(\mathrm{t})$ determined the maximum normalized cross-correlation between CSK tension *A* and FA size *B*. The time point at which $NCC(\mathrm{t})$ reached its maximum determined the time delay of FA size *B* relative to CSK

tension *A* and was designated in this work as the "CSK tension - FA size cross-correlation time delay".

3.3 Results and discussion

3.3.1 Single-cell mechanical homeostasis and subcellular rheostasis

We first examined whether individual REF-52 fibroblasts would exhibit mechanical homeostasis at a global cellular scale. We first applied an 8% equibiaxial stretch to single REF-52 cells (**Figure 3-3 b**). Before cell stretch, the whole-cell summation of CSK tension and FA size of single REF-52 fibroblasts remained constant as mechanobiological ground (quasi-static) states, and they restored their respective ground-state values at the single-cell level within 30 min after the onset of 8% static equibiaxial stretch (**Figure 3-3 e,f**). Such homeostatic behaviors of REF-52 fibroblasts at the single-cell level for both CSK tension and FA were characterized by biphasic dynamics comprising an acute excitation phase within 1 min after the onset of stretch (*Phase I*; t = 0 - 1 min) followed by another slow decay phase within 1 - 30 min following sustained cell stretch (*Phase II*; t = 1 - 30 min), in which both whole-cell CSK tension and FA decreased monotonically to their respective ground states (**Figure 3-3 e,f**). The biphasic responses of both CSK tension and FAs were consistent with our guess that cells experience an excited state followed by a post-excitation state to restore its quasi-static states as it was before the mechanical stimuli (**Figure 3-3 a**).

Other than the whole-cell responses, the analysis of single FAs and the associated CSK tension was also available using the micropost array cytometry is illustrated in **Figure 2-3**. We

performed linear correlation analysis and cross-correlation analysis (**Section 3.2.6**) between single FAs and their associated CSK tension to exam their correlation and dynamics synchronization. Detailed subcellular analysis using paired CSK tension - FA size data pooled from single REF-52 fibroblasts revealed strong linear correlation and temporal synchronization between subcellular CSK tension and FA size during the entire mechanical homeostasis of REF-52 fibroblasts when responding to 8% static equibiaxial stretch (**Figure 3-4 a-d, f, i**), suggesting interdependence and temporal synchronization of CSK tension and FA morphogenesis as persistent and robust properties associated with homeostasis.

Strikingly, at the subcellular level, however, highly heterogeneous, non-homeostatic behaviors were observed for individual FAs and their associated CSK tension (**Figure 3-5 a-d**). For the four posts marked with red, green, blue, and purple arrows in **Figure 3-5 a**, the dynamics of FAs and subcellular CSK tension co-localized on them were plotted with color-coded in **Figure 3-5 b&c**. All pairs of data experienced an excitation immediately after the onset of cell stretching in *Phase I*. After initial excitation in *Phase I*, individual FAs and their dynamically correlated CSK tension underwent either relaxation or reinforcement in *Phase II* when the whole-cell was undergoing the relaxation phase in the homeostatic response to restore the ground state values of CSK tension and FAs (**Figure 3-3 e&f**, **Figure 3-5 b&c**). Interesting, the linear correlations between single FAs and the associated subcellular CSK tension were still well maintained during the distinctive dynamic reactions. The distinction between cellular responses and subcellular responses raised the question how the heterogeneous and non-homeostatic subcellular responses could give rise to a homeostatic cellular response.

We next investigated how heterogeneous, non-homeostatic responses of subcellular CSK tension and FA might collectively determine single-cell homeostasis. We grouped the paired data of individual FAs and the subcellular CSK tension based on their ground-state CSK tension before cell stretch, and the average responses in each cohort were plotted with color-coded in **Figure 3-5 e &f**. Our analysis revealed an expanded spectrum of graduated paths (termed "rheostasis") for both subcellular CSK tension and FA size. The pairs with low ground-state CSK tension had a sharp increase in both CSK tension and FA size after the onset of cell stretch (*Phase I*), and a powerful reinforcement to keep rising in the sustained cell stretch (*Phase II*). However, as the value of ground-state CSK tension increases, the reinforcement in these cohorts was weakened and even replaced with a strong relaxation of CSK tension and decrease of FA sizes, thought the initial excitation in *Phase I* was observed in all cohorts (**Figure 3-5 e &f**). Of note, the dynamics responses of subcellular CSK tension and FA size eventually converged onto their respective ground-state, whole-cell averages (**Figure 3-5 e &f**).

By presenting the subcellular variations of CSK tension and FA size during both *Phase I* (t = 0 - 1 min) and *Phase II* (t = 1 - 30 min) in two-dimensional ground-state CSK tension - FA size diagrams, we further unraveled dependence of subcellular rheostasis on ground-state values of CSK tension and FA size (**Figure 3-5 g-j**). Specifically, in *Phase I*, reinforcements of subcellular CSK tension and FA size appeared uniform across the cell, likely serving as a passive mechanical response to resist rapid cell deformation (**Figure 3-5 g&i**). In distinct contrast, in *Phase II*, dynamics of CSK tension and FA demonstrated a notable mechanosensitive transition from reinforcement to relaxation. Subcellular CSK tension and FA with ground-state values less than whole-cell averages (*red* dashed lines) underwent reinforcement-like rheostasis; whereas

those greater than whole-cell averages (*red* dashed lines) experienced relaxation-like rheostasis (**Figure 3-5 h&j**).

In addition to REF-52 fibroblasts, single-cell mechanical homeostasis and mechanosensitive subcellular rheostasis pattern of CSK tension and FAs were observed in human mesenchymal stem cells (HUMSCs) and human skin fibroblasts (HUSFs) when responding to 8% static equibiaxial stretch (**Figure 3-6**).

We further examined if mechanical stimulation severity affected single-cell homeostasis and subcellular rheostasis by applying 4% and 16% sustained equibiaxial stretching other than 8% cell stretch. Compared with 8% static equibiaxial stretch, 4% static stretch resulted in similar biphasic single-cell homeostasis and mechanosensitive subcellular rheostasis in REF-52 fibroblasts (**Figure 3-3 c&d, Figure 3-4 e&h**, **Figure 3-7 a&b,e-h**). However, for REF-52 fibroblasts under 16% static equibiaxial stretch, a significant variation on the pattern of subcellular rheostasis was observed, yet the observation still supported whole-cell homeostasis and subcellular rheostasis on CSK tension and FAs (**Figure 3-3 g&h, Figure 3-7 c&d, i-l**). We noticed that reinforcement of either CSK tension or FA with high ground-state values during *Phase I* was inhibited, leading to monotonic relaxation of subcellular CSK and the decrease of FA size for those with high ground-state value (**Figure 3-7 c&d,i-l**). Consequently, biphasic responses of whole-cell FAs was abolished and replaced with an apparent quasi-static dynamics with only small and non-significant variation (**Figure 3-3 h, Figure 3-7 d**). 16% static equibiaxial stretch further compromised linear correlation between subcellular CSK tension and FA size in REF-52 fibroblasts (**Figure 3-4 g**). Strikingly, REF-52 fibroblasts under 16% static equibiaxial stretch still retained single-cell mechanical homeostasis with temporal

synchronization between subcellular CSK tension and FA size (**Figure 3-3 g&h**, **Figure 3-4 j**), suggesting single-cell homeostasis as a resilient property when responding to a broad range of external biophysical stimulation.

To conclude, mechanical homeostasis on CSK tension and FA were observed with different cell types and with different severity of sustained cell stretch, suggesting that they are a general phenomenon and likely intrinsic properties of the cells. Rather than owing to a self-similarity-like property governing mechanoresponsive behaviors across both cellular and subcellular scales, we approved for the first time that the cellular-scale mechanical homeostasis was an emergent biological phenomenon driven by collective subcellular rheostasis of CSK tension and FA following distinct mechanosensitive compensatory patterns. This finding highlighted the intrinsic heterogeneity of mechanobiological behaviors across at different scales, and the importance of multi-scale studies from both bottom-up and top-down for the understanding of the apparent biological phenomena and the collective effect of different mechanisms.

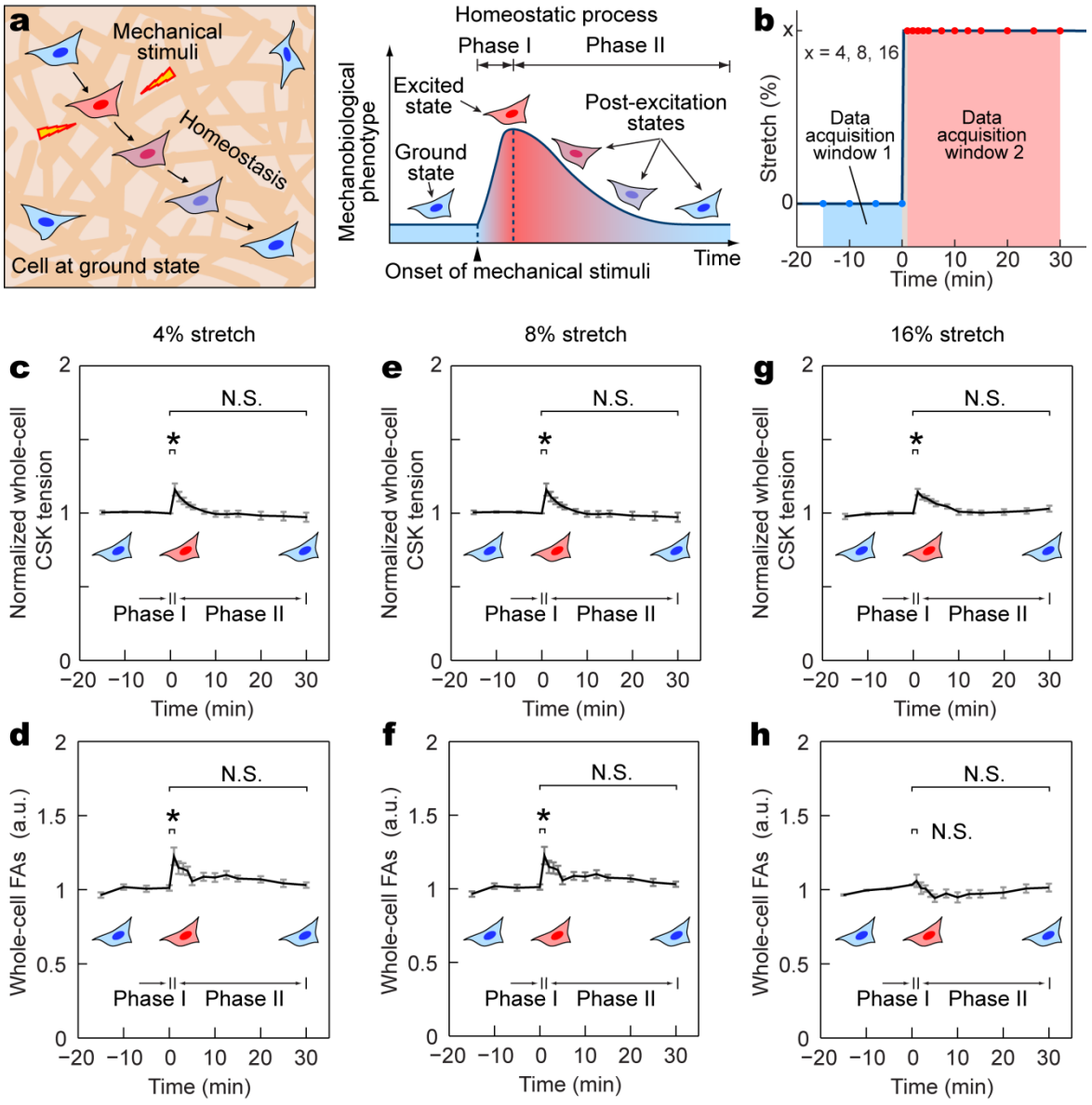

Figure 3-3 Dynamics of whole-cell cytoskeleton (CSK) tension and focal adhesion (FA) during single cell homeostasis. (**a**) Conceptual schematic of single-cell mechanical homeostasis. Upon mechanical perturbation, a biphasic cellular response comprising an excited state (*Phase I*) and a post-excitation state (*Phase II*) restores ground states of cellular mechanical phenotype through actively regulated feedback mechanisms. (**b**) Static equibiaxial stretch protocol in conjunction with real-time, live-cell imaging to monitor dynamics responses of CSK tension and FAs upon cell stretch. Blue dots and red dots marked the unevenly spaced time points for live-cell data acquisition before and after the onset of cell stretch, respectively. (**c**-**h**) Temporal evolutions of normalized whole-cell CSK tension (**c**,**e**,**g**) and FA size (**d**,**f**,**h**) during single-cell mechanical homeostasis for REF-52 fibroblasts under 4% (**c**,**d**), 8% (**e**,**f**), and 16% (**g**,**h**) static equibiaxial stretch. Data for each single cell was normalized to ground-state values at t = 0 min. Data represents the mean ± s.e.m with n = 8, 10, 8 for 4%, 8%, and 16% stretches, respectively. P-

values were calculated using student's paired sample t-test comparing data before (t = 0 min) and after (t = 1 min and 30 min) cell stretch. N.S., statistically insignificant and $P > 0.05$. *, $P < 0.05$.

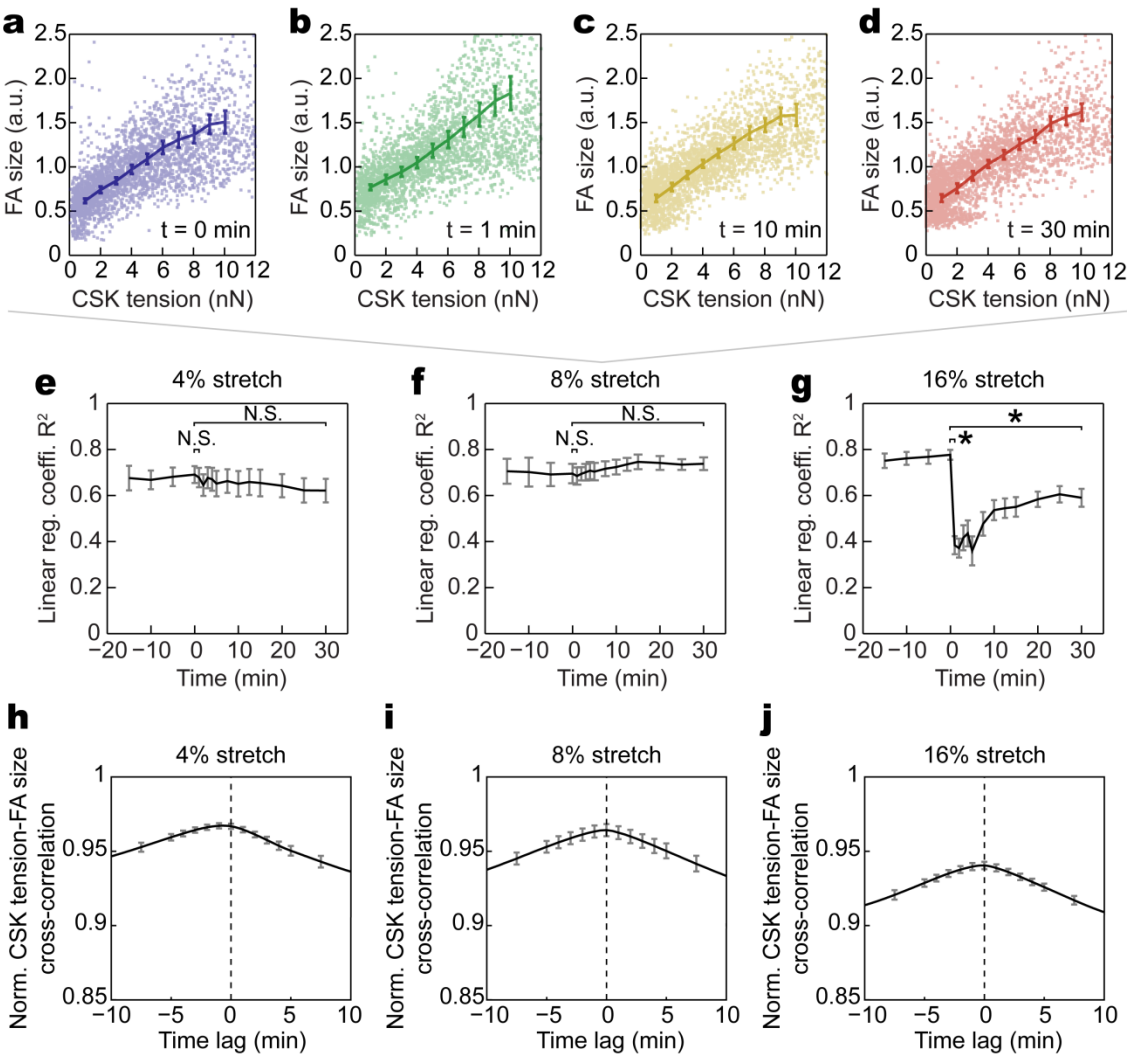

Figure 3-4 Dynamic correlation and synchronization of subcellular cytoskeleton (CSK) tension and focal adhesion (FA) during single-cell mechanical homeostasis (**a-d**) Paired subcellular CSK tension - FA size data showing correlation during mechanical homeostasis upon 8% equibiaxial cell stretch. Data points represent individual FAs detected at time point as indicated. More than 2,500 FAs were analyzed from n = 10 REF-52 fibroblasts. (**e-g**) Linear regression coefficients R^2 calculated from best linear fitting of paired FA size - CSK tension data were plotted as a function of time for 4% (**e**), 8% (**f**), and 16% (**g**) stretches. (**h-j**) Cross-correlation analysis of temporal coordination between subcellular CSK tension and FA size in response to 4% (**h**), 8% (**i**), and 16% (**j**) stretches. Maximums of normalized cross-correlation between CSK tension and FA size for each FA subgroups were all around or above 0.9, supporting the prominent temporal synchronization between CSK tension and FA size in response to 4% - 16% cell stretches. All data represents the mean ± s.e.m, with n = 8, 10, 8 for 4%, 8%, and 16% stretches, respectively. P-values were calculated using student's paired sample t-test comparing the data before (t = 0 min) and after (t = 1 min, 30 min) cell stretch. N.S., statistically not significant and $P > 0.05$. *, $P < 0.05$.

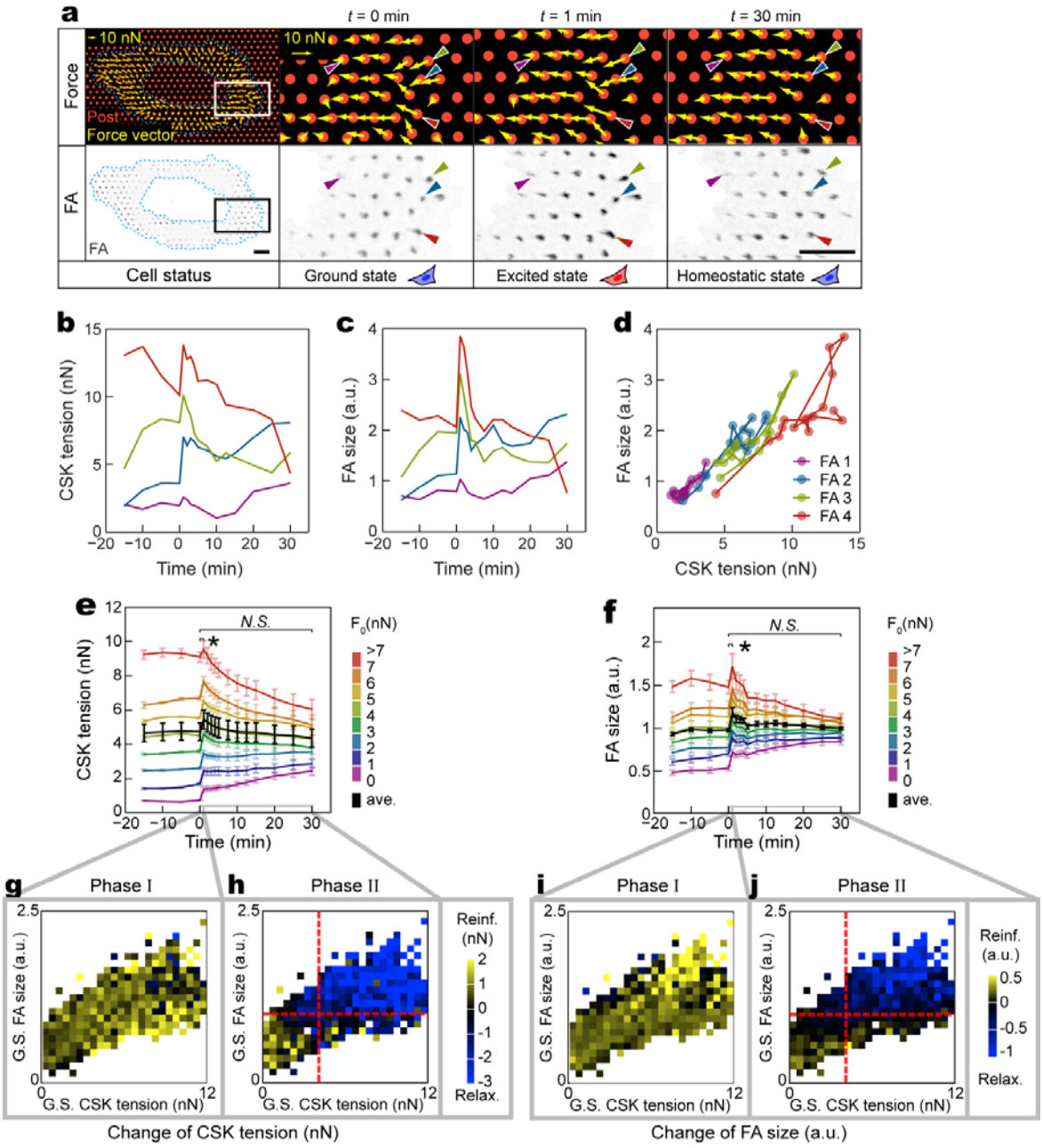

Figure 3-5 Mechano-sensitive subcellular rheostasis of CSK tension and FAs drives single-cell mechanical homeostasis. Representative fluorescent images of microposts (*red dots*) with force vector maps (*yellow arrows*) showing the subcellular CSK tension, and the corresponding fluorescent images showing individual FAs in a single REF-52 fibroblast before (t = 0 min, ground state) and after (t = 1 min, excited state; t = 30 min, homeostatic state) the onset of 8% static equibiaxial stretch. Color-coded arrowheads marked four microposts and the corresponding single FAs during the temporal evolution. Region of interest enclosed by blue dashed polygons excluded the nucleus and perinuclear region where signal-to-noise ratios of both FA size and CSK tension were significantly lower compared with other subcellular regions. (**b&c**) Temporal evolutions of CSK tension (**b**) and FA size (**c**) for four representative single FAs (marked by color-coded arrowheads in **a**) showing subcellular heterogeneity and non-homeostatic response during single-

cell mechanical homeostasis. (**d**) Temporal trajectories of paired CSK tension - FA size data for the same four single FAs in **b&c** during single-cell homeostasis. (**e&f**) Heterogeneous rheostatic paths for subcellular CSK tension (**e**) and FA (**f**). Results from REF-52 fibroblasts under 8% static equibiaxial stretch were grouped into subsets based on ground-state CSK tension values at t = 0 min (F_0). Average result from each subset was plotted using the rainbow spectrum (from *purple* to *red*). Whole-cell average response (*black*) was included for referencing single-cell homeostasis. Data represents the mean ± s.e.m with n = 10. (**g-j**) Dependence of subcellular rheostasis on ground-state values of both CSK tension and FA size. Changes in CSK tension (**g&h**) and FA size (**i&j**) during *Phase I* (t = 0 - 1 min; **g&i**) and *phase II* (t = 1 - 30 min; **h&j**) were color-coded in two-dimensional ground-state CSK tension - FA size diagrams obtained at t = 0 min. Red dashed lines in **h** and **j** marked average ground-state values of CSK tension and FA size as well as a transition boundary between reinforcement and relaxation for subcellular rheostasis during *Phase II*.

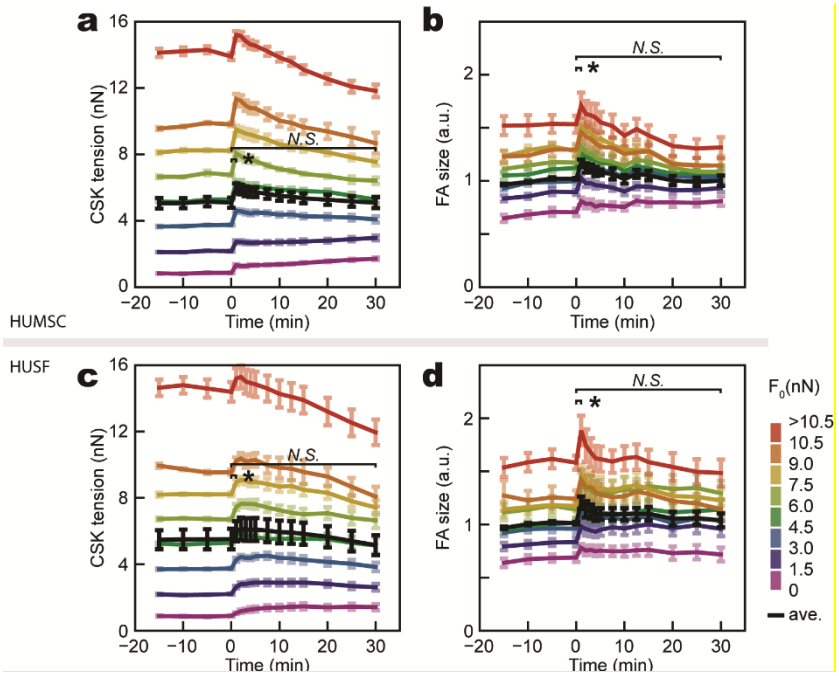

Figure 3-6 Single-cell mechanical homeostasis and subcellular rheostasis in human mesenchymal stem cells and human skin fibroblasts. Human mesenchymal stem cells (HUMSC) and human skin fibroblast (HUSF) were stretched at 8% equibiaxially and sustained. Heterogeneous rheostatic paths for subcellular CSK tension (**a&c**) and FA (**b&d**) were plotted for FA subsets grouped based on ground-state values of CSK tension F_0 at t = 0 min. Average result from each subset was plotted using the rainbow spectrum (from *purple* to *red*). Whole-cell average responses were included for referencing single-cell homeostasis (*black*). Data represents the mean ± s.e.m with n = 10 cells. P-values were calculated using student's paired sample t-test comparing data before (t = 0 min) and after (t = 1 or 30 min) stretch. *N.S.*, statistically not significant and $P > 0.05$. *, $P < 0.05$.

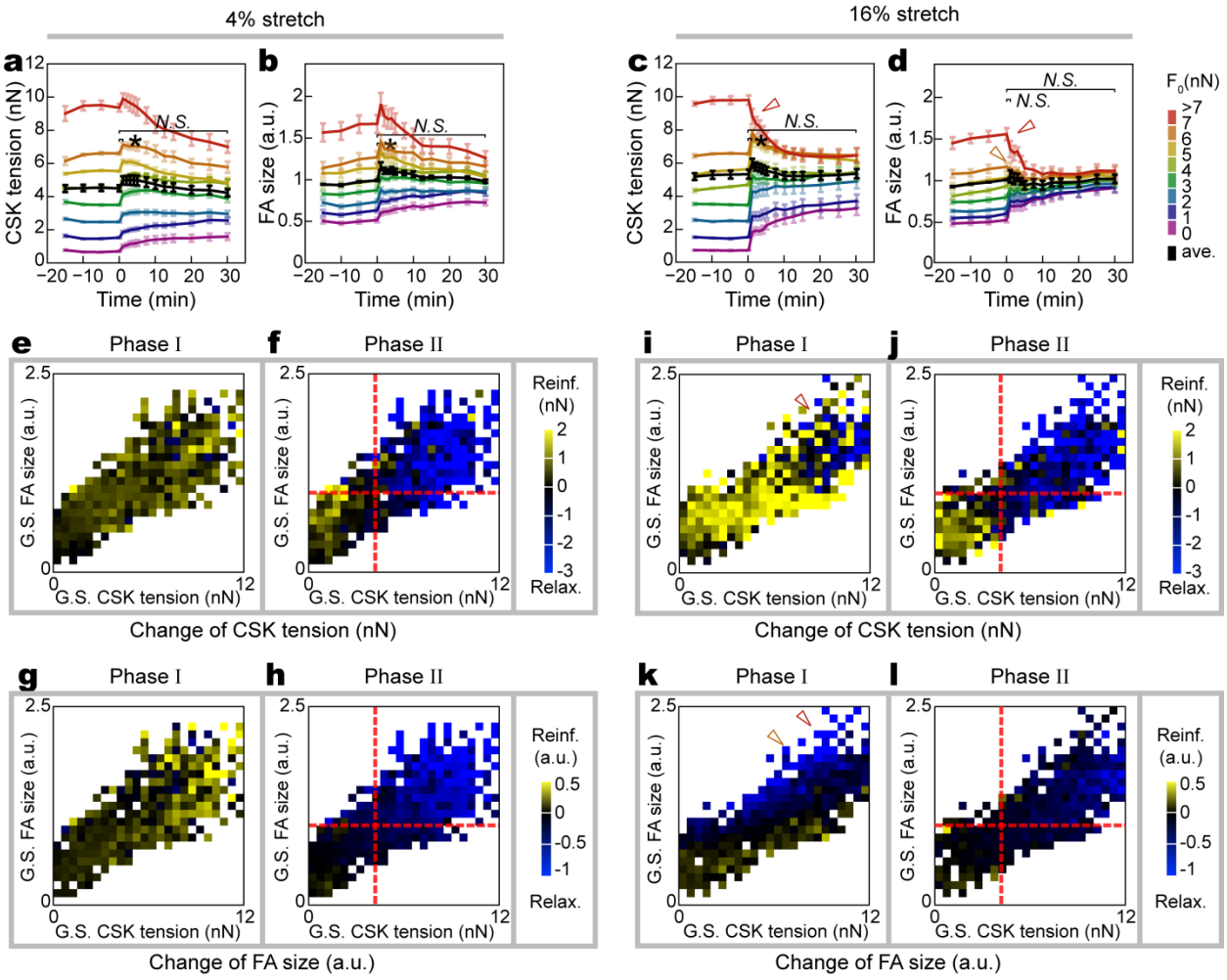

Figure 3-7 Effect of stretch severity on single-cell homeostasis and subcellular rheostasis. **(a-d)** Subcellular CSK tension and FA followed distinct mechanosensitive rheostatic paths to drive single-cell mechanical homeostasis for single REF-52 cells under 4% (**a&b**) and 16% (**c&d**) static equi-biaxial stretches. Results were grouped into subsets based on ground-state CSK tension values F_0 at t = 0 min. Average result from each subset was plotted using the rainbow spectrum (from *purple* to *red*). Whole-cell average responses (*black*) were included as a reference. Data represents the mean ± s.e.m with n = 8 for both 4% and 16% stretches. P-values were calculated using student's paired sample t-test comparing data before (t = 0 min) and after (t = 1 or 30 min) stretch. *N.S.*, statistically not significant and $P > 0.05$. *, $P < 0.05$. (**e-h, i-l**) Dependence of subcellular rheostasis on ground-state values of CSK tension and FA size. Changes in CSK tension (**e&f**, **i&j**) and FA size (**g&h**, **k&l**) during *Phase I* (t = 0 - 1 min; **e**, **g**, **i**, **k**) and *phase II* (t = 1 - 30 min; **g**, **h**, **k**, **l**) were color-coded in two-dimensional CSK tension - FA size diagrams obtained at t = 0 min showing ground-state values of CSK tension and FA size. Red dashed lines in **f**, **h**, **j**, and **l** marked average ground-state values of CSK tension and FA size as well as a transition boundary between reinforcement and relaxation for subcellular rheostasis of CSK tension (**f**, **j**) and FA size (**h**, **l**) during *Phase II*. Hollow red and orange arrowheads indicated damped reinforcement of CSK tension and FA size in *Phase I*.

3.3.2 Exit of single-cell mechanical homeostasis by skewed subcellular rheostasis

Although we reported that mechanical homeostasis was a general phenomenon in our study, it does not always hold as was reported by others [96]. We investigated the mechanisms that could influence the whole-cell mechanical homeostasis and by comparing the behaviors at cellular scale and subcellular scale to study how the subcellular behaviors determine the exit of single-cell mechanical homeostasis.

We first investigated how single-cell mechanical homeostasis might respond to perturbations to the CSK, which have been implicated in pathogenic contexts featuring dysregulation of mechanical homeostasis, such as cancer [109]. REF-52 fibroblasts were treated with small-molecule inhibitors targeting CSK integrity and tension: (1) nocodazole, which depolymerizes microtubules and impedes FA disassembly[253]; (2) blebbistatin, which inhibits myosin motor activity and thus CSK tension[254]; (3) jasplakinolide, which enhances actin polymerization[255]; (4) cytochalasin D, which blocks actin polymerization[256]. To minimize off-target effects, dosages of the inhibitors were optimized so that there was no significant change in the cell area, FA size, CSK tension, or actin CSK architecture at ground states in inhibitor-treated cells (**Figure 3-1**). Of note, although the low dosage of cytochalasin D still appeared to affect the apparent cell phenotypes (**Figure 3-1**), it was required to elicit a significant change in single-cell homeostasis and thus to study corresponding variations in subcellular homeostasis (see discussions below).

Interestingly, upon treatments with the inhibitors, single-cell homeostasis and subcellular rheostasis of CSK tension were well preserved in REF-52 fibroblasts under 8% static equibiaxial stretch (**Figure 3-8 a**, top panel). However, significant variations in subcellular FA rheostasis

were evident in inhibitor-treated cells. Specifically, nocodazole, blebbistatin, and jasplakinolide treatments completely prevented FAs with high ground-state values from undergoing relaxation in *Phase II* (**Figure 3-8 d, f, g, i, j, l**, bottom panel). Jasplakinolide treatment also abolished acute increase in FA size during *Phase I* (**Figure 3-8 j,** bottom panel; **l**, top panel). These effects significantly biased subcellular FA rheostasis patterns and break the balance on subcellular compensation, hence induced an efficient exit of FA homeostasis at the single-cell level. Notably, although cytochalasin D did not significantly affect mechanosensitive rheostatic transition between reinforcement and relaxation, it largely abolished ground-state FAs sustaining high CSK tension and thus biased the proportions of distinct FA subsets participating in the rheostasis, leading to skewed FA homeostasis at single-cell level (**Figure 3-8 m**, **n**, **o** and **Figure 3-1 h**). In addition, all inhibitor treatments reduced time-independent linear correlation, as well as temporal synchronization, between subcellular CSK tension and FA (**Figure 3-9**), consistent with the finding that FA but not CSK tension exhibited biased rheostasis under inhibitor treatments.

Inspired by the CSK and CSK tension-dependent subcellular rheostatic pattern that displayed apparent catch and slip-like behaviors, and examined the regulatory role of catch-slip-bond like behaviors of the CSK-FA system on the maintenance of cellular homeostasis via subcellular rheostasis. Catch-slip bond mechanisms have been demonstrated common in the ECM-FA-cytoskeleton system and critical to cellular mechanotransduction [179, 180, 260-264]. To examine specifically the role of easy-to-access integrin-mediated catch-slip bond in mechanosensitive subcellular rheostasis, HUMSCs were treated with an antibody (clone TS2/16) targeting human β_1 integrin before assayed with the stretchable micropost array membrane for 8% static equibiaxial stretch. Single molecular studies *in vitro* have demonstrated that antibody

TS2/16 treatment shortens integrin-fibronectin bond lifetime under high forces and prolongs the lifetime at low forces (**Figure 3-10 a**) [265]. *Ex vivo*, cells treated with TS2/16 antibody had lower cell contraction and larger FA clusters at the ground state (**Figure 3-10 b&c**). Upon cell stretching, treatment with TS2/16 biased subcellular rheostasis and single-cell homeostasis of FA but not CSK tension (**Figure 3-10 d-g**), confirming FA dynamics as a more sensitive gating mechanism for cellular homeostasis compared to CSK tension. Specifically, TS2/16 treatment inhibited both the strengthening (*Phase I*) and relaxation (*Phase II*) phases for FAs with high ground-state values (**Figure 3-10 g**, *red* and *orange*). Suppressed FA strengthening in *Phase I* was likely due to the domination of the slip portion of integrin bond dynamics at high forces and a rapid switch from "catch" to "slip" mode after cell stretch. Subsequently suppressed relaxation (leading to an apparent stabilization phase) was likely attributable to prolonged integrin bond lifetime equivalent to a "re-catch" for a failing bond. These results provided convincing evidence supporting the involvement of integrin catch-slip-bond dynamics, and likely the other catch-slip bonds in the CSK-FA system in mediating mechanosensitive FA rheostasis.

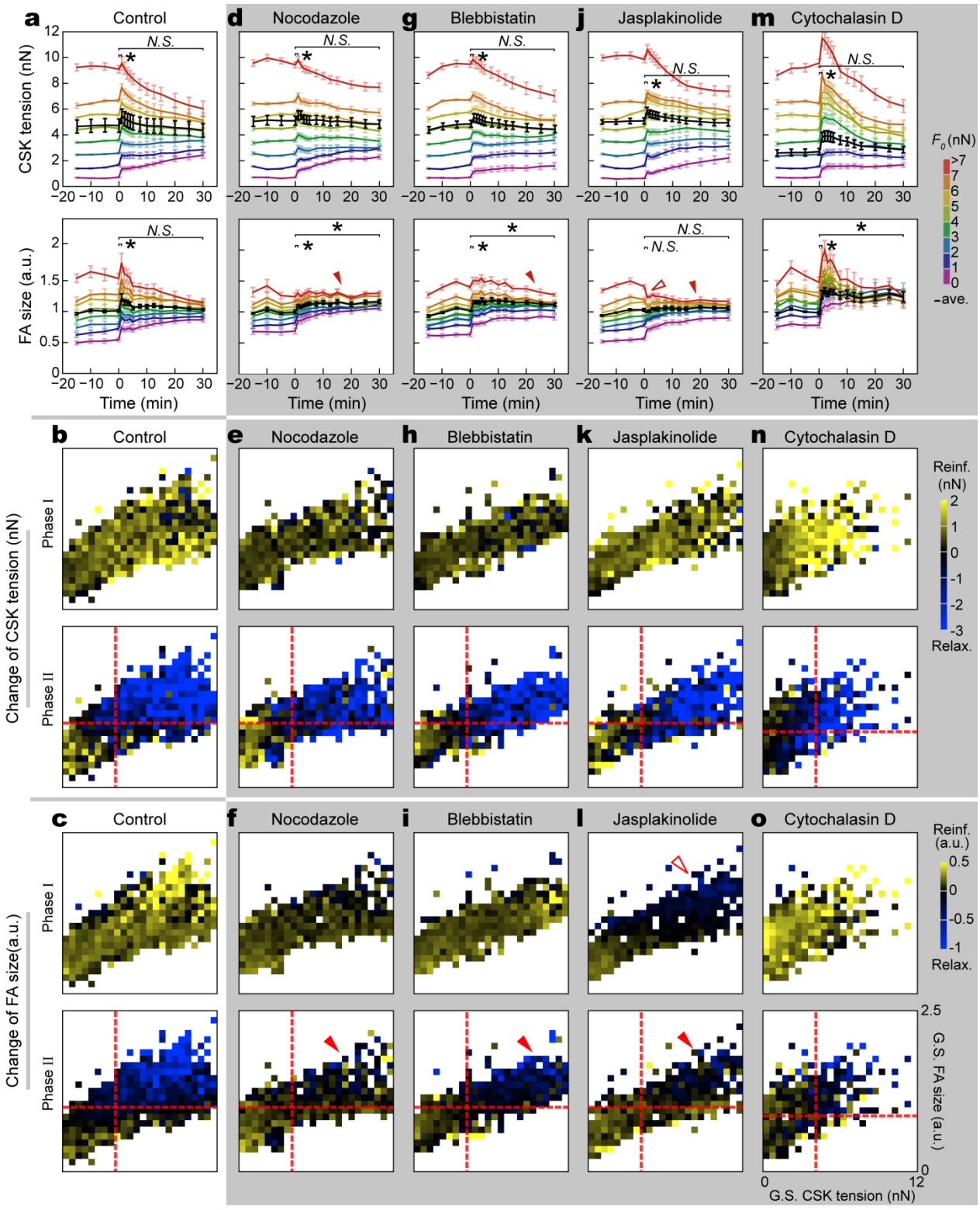

Figure 3-8 Dependence of single-cell homeostasis and subcellular rheostasis on the CSK integrity. Responses of single-cell homeostatic and subcellular rheostatic responses of CSK tension and FAs

to pharmacological inhibitors in REF-52 fibroblasts under 8% static equi-biaxial stretch (**a-c**: untreated control; **d-f**: nocodazole; **g-i**: blebbistatin; **j-l**: jasplakinolide; **m-o**: cytochalasin D). (**a**, **d**, **g**, **j**, **m**) Whole-cell average response (*black*) and rheostatic subcellular responses (*purple* to *red* spectra) of CSK tension (*top*) and FA (*bottom*) to 8% static equi-biaxial stretch with the pharmacological inhibition as indicated. Paired subcellular CSK tension-single FA data were grouped into subsets based on ground-state CSK tension values F_0 at t = 0 min. Average results from each subset were plotted using the rainbow spectra (from *purple* to *red*), showing the distinct heterogeneous rheostatic patthern. Whole-cell average responses (*black*) were included showing the whole-cell homeostatic or non-homeostatic response. Data represents the mean ± s.e.m with n = 10 for each condition. P-values were calculated using student's paired sample *t*-test comparing data before (t = 0 min) and after (t = 1 or 30 min) stretch. *N.S.*, statistically not significant and $P > 0.05$. *, $P < 0.05$. (**b&c**, **e&f**, **h&i**, **k&l**, **n&o**) Dependence of subcellular rheostasis on ground-state values of CSK tension and FA size. Changes in CSK tension (**b**, **e**, **h**, **k**, **n**) and FA size (**c**, **f**, **i**, **l**, **o**) during *Phase I* (t = 0 - 1 min; *top*) and *phase II* (t = 1 - 30 min; *bottom*) were color-coded in two-dimensional CSK tension - FA size diagrams obtained at t = 0 min showing ground-state values of CSK tension and FA size. Red dashed lines marking the average of ground-state values of CSK tension and FA size for untreated cells were included as references to illustrate changes in the mechanosensitive rheostatic patterns upon treatments with small-molecule inhibitors. Hollow red arrowheads indicated damped FA strengthening in *Phase I*, whereas solid red arrowheads marked largely abolished FA relaxation in *Phase II*. Under each condition, data from 10 cells was pooled and analyzed.

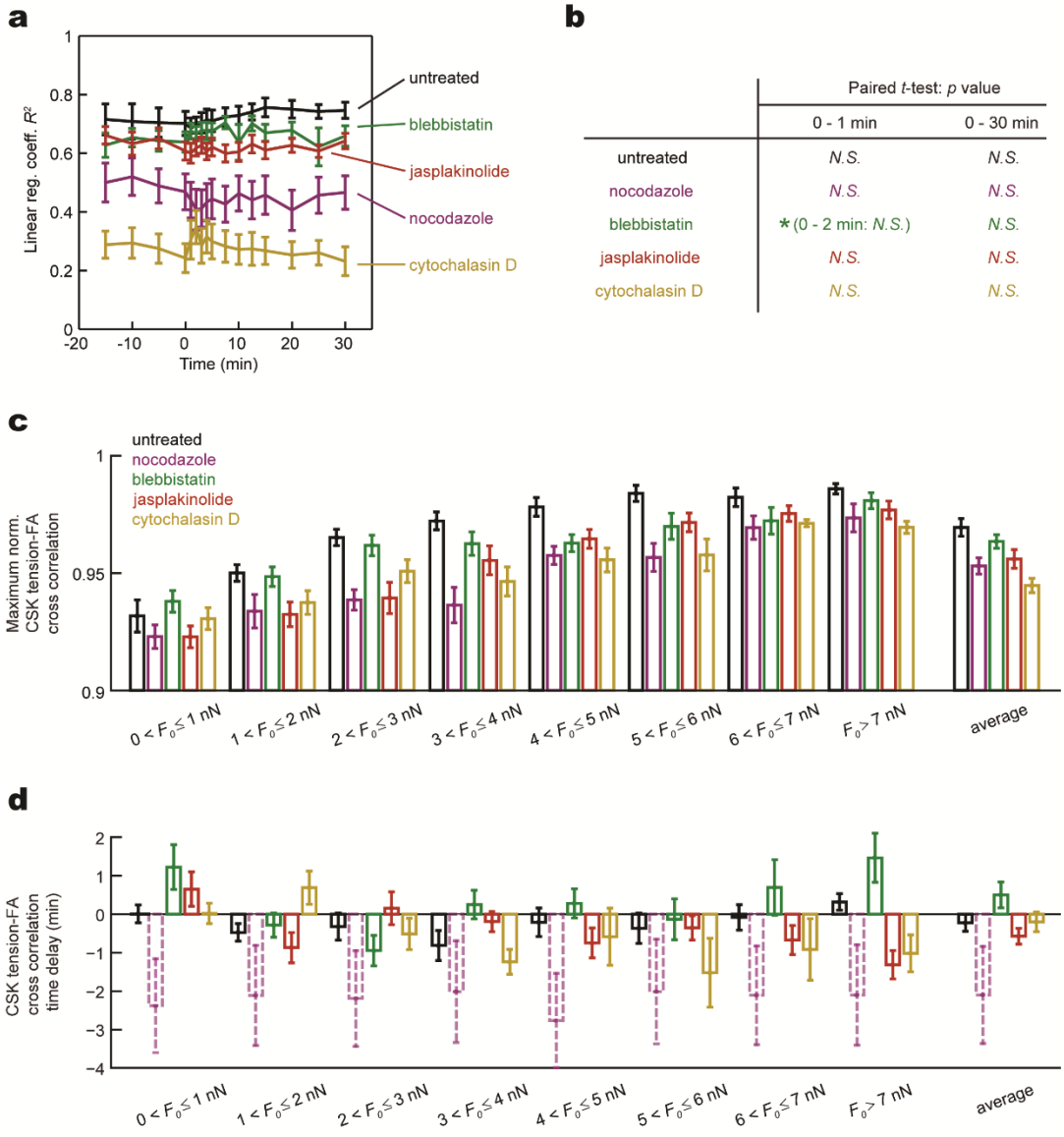

Figure 3-9 Effects of small-molecule inhibitors on CSK tension and FA correlation. (**a&b**) and synchronization (**c&d**) of subcellular cytoskeleton (CSK) tension and focal adhesion (FA) in REF-52 fibroblasts during homeostatic processes in response to 8% static equibiaxial stretch. (**a&b**) Linear regression coefficients R^2 calculated from best linear fitting of paired FA size - CSK tension data were plotted as a function of time for both untreated and drug-treated cells as indicated. Data represents the mean ± s.e.m with n = 10. In b, P-values were calculated using student's paired sample t-test comparing R2 values between t = 0 min and t = 1 min or between t = 0 min and t = 30 min. N.S., statistically not significant and P > 0.05. *, P < 0.05. (**c&d**) Temporal synchronization between CSK tension and FA determined by cross-correlation analysis. Bar plot in c plotted maximum normalized cross-correlation between CSK tension and FA size and its dependence on ground-state values of CSK tension F0 as well as drug treatment conditions as indicated. Maximums of normalized cross-correlation between CSK tension and FA size for all FA subgroups were > 0.9, supporting prominent temporal synchronization between CSK tension and FA size under different drug treatment conditions. Bar plot in d showed cross-correlation time delay

between CSK tension and FA. Negative cross-correlation time delay suggested that FA responded more promptly than CSK tension and vice versa. Cross-correlation time delay data for the nocodazole treatment group was likely an artifact given the distinct difference between the data for CSK tension and FA size.

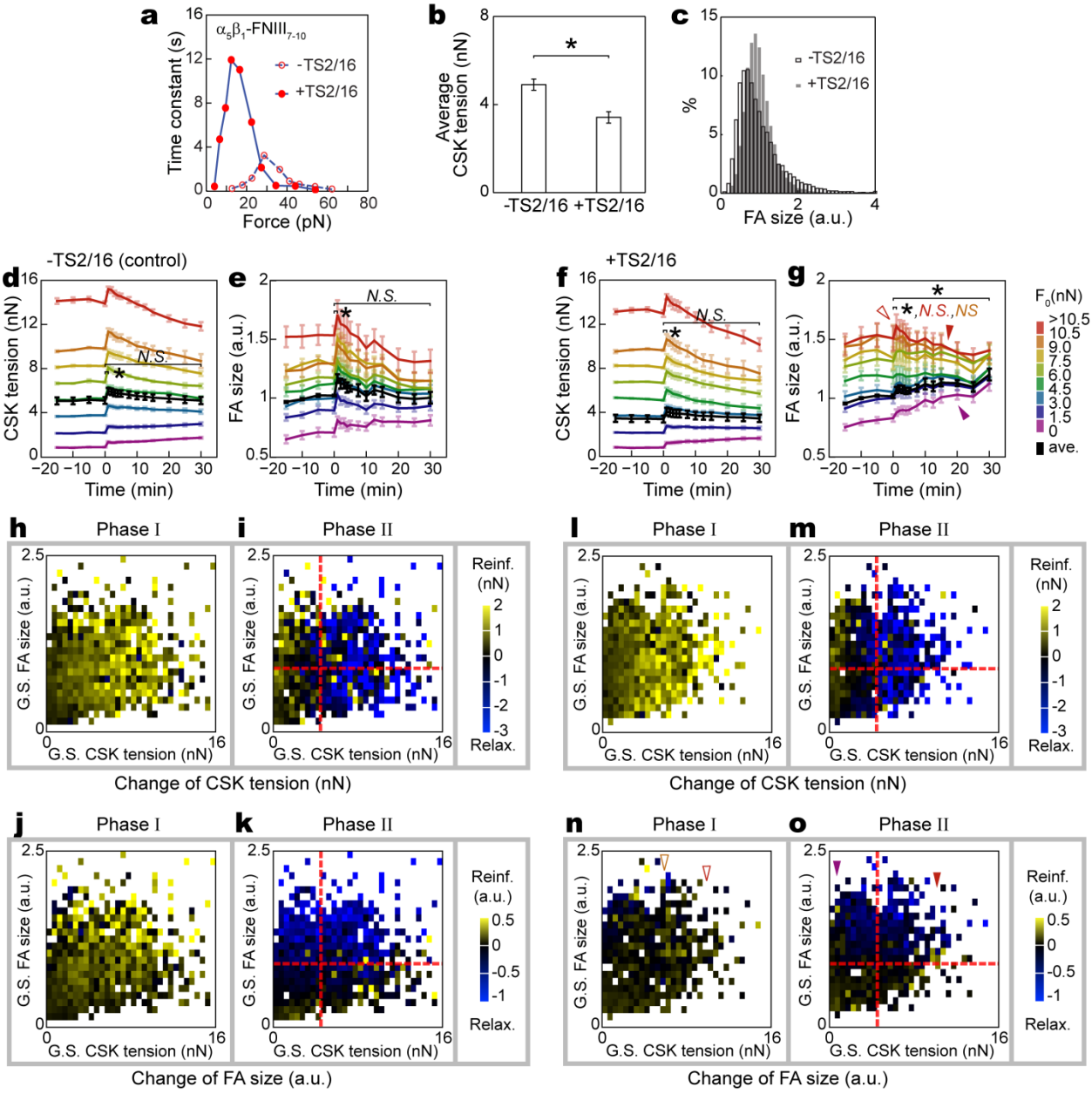

Figure 3-10 Dependence of single-cell homeostasis and subcellular rheostasis on the catch-slip bond behaviors. Force - lifetime diagram of the catch-slip bond between $\alpha_5\beta_1$ integrin and FNIII$_{7-10}$, with or without treatments of antibody TS2/16 as indicated [265]. (**b&c**) Experimental results showing reduction of CSK tension (**b**) and a shift of FA size distribution toward large FAs (**c**) upon TS2/16 treatments for HUMSCs at ground-state. (**d-g**) Single-cell and subcellular responses of CSK tension (**d&f**) and FAs (**e&g**) in HUMSCs under 8% static equibiaxial stretch with (**f&g**) or without (**d&e**) TS2/16 treatment. Paired single FA-subcellular CSK tension data were grouped into subsets based on ground-state CSK tension values at t = 0 min (F_0). Average results from each subset were plotted using the rainbow spectra (from *purple* to *red*). Whole-cell average responses were plotted in *black* indicating changes in single-cell homeostasis. Data represents the mean ± s.e.m with n = 11. *P*-values were calculated using student's paired sample *t*-test comparing data

before (t = 0 min) and after (t = 1 or 30 min) stretch. *N.S.*, statistically not significant and $P > 0.05$. *, $P < 0.05$. Statistical analysis for different FA subsets was color-coded as indicated. (**h-o**) Dependence of subcellular rheostasis on ground-state values of CSK tension and FA size in HUMSCs. Changes in CSK tension (**h**, **i**, **l**, **m**) and FA size (**j**, **k**, **n**, **o**) during *Phase I* (t = 0 - 1 min; **h**, **j**, **l**, **n**) and *phase II* (t = 1 - 30 min; **i**, **k**, **m**, **o**) were color-coded in two-dimensional CSK tension - FA size diagrams obtained at t = 0 min showing ground-state values of CSK tension and FA size. Red dashed lines marked the average of ground-state values of CSK tension and FA size for TS2/16 untreated HUMSCs, showing the CSK tension and FA size-dependent transition between reinforcement and relaxation, as well as the changes in the mechanosensitive rheostatic patterns upon TS2/16 treatment. Hollow orange and red arrowheads indicated damped FA strengthening in *Phase I*, whereas solid purple arrowhead marked enhanced FA reinforcement and solid red arrowheads marked largely abolished FA relaxation in *Phase II*.

3.4 Summary

Living cells behave as adaptive autonomous systems in the face of mechanical perturbations that operate through subcellular events with elegant spatiotemporal regulation to maintain the intracellular stability. However, the link between subcellular dynamics and single-cell level properties reacting to the mechanical perturbation has not been studied and understood. The present work, for the first time, has established a missing link between the single-cell mechanical homeostasis and the subcellular events.

With the application of micropost array cytometry described in **Chapter 2**, we have for the first time illustrated that single-cell mechanical homeostasis is an emergent phenomenon driven by graduated and distinctive dynamics (“rheostasis”) of CSK tension and FA at a subcellular scale. Such subcellular rheostasis further featured a mechanosensitive pattern wherein quasi-static values of CSK tension and FA determined their distinct reactive paths via either relaxation or reinforcement that compensate with each other to approach mechanical homeostasis. Our drug treatment studies have further demonstrated an effective exit of mechanical homeostasis through skewed subcellular rheostasis and unbalanced intracellular

compensation, suggesting it important role in pathogenic contexts featuring dysregulation of mechanical homeostasis, such as cancer. This finding emphasized that cellular mechanical homeostasis depends highly on the structural and functional integrity of the ECM-FA-CSK mechanical network, and provided a possible explanation to the non-homeostatic and/or buffering cellular responses to cell stretching as are reported by other groups [96, 97].

To highlight, we have discovered that subcellular dynamics would observe patterns different from that at the single-cell level, and thus have confirmed single-cell homeostasis as an emergent phenomenon. Such idea, to the best of our knowledge, is proposed for the first time in this present work. This idea, which has potentially revealed a general and previously underappreciated physical nature of single-cell behaviors, should inspire researchers in diverse fields (such as oncology, developmental biology, and stem cell biology) to initiate new multidimensional and interdisciplinary research studying cellular behaviors as emergent properties driven by collective dynamics at the subcellular level.

Chapter 4

Mechano-biophysical model

The major content of this chapter is reproduced from our previously published paper: "Mechanosensitive subcellular rheostasis drives emergent single-cell mechanical homeostasis" in Nature Materials, 2016 [88].

4.1 Introduction

Mechanics regulates biological processes at molecular, cellular, tissue, organ, and organism level. For the quantification and identification of the mechanosensitive responses and their mechanisms that are likely interconnected, there have been increasing appreciations for the value of computational models in the study of mechanobiology and mechanotransduction. With quantitative experimental data, knowledge from biology, physics, mechanics, material science, and mathematics is employed to create models to recapitulate certain aspects of the biological system, and to explain mechanosensitive cellular behaviors.

The simplest biomechanical model is perhaps to model cellular and multicellular structures as a network of 1D elements that have the mechanical properties of elastic (spring) , viscous (dashpot), and/or contractile elements [266-268]. These models can provide insight into

basic mechanical behaviors, but their application are limited due to the lack of other significant mechanical links such as cell-ECM and cell-cell interactions. More commonly, the mechanical behaviors of tissues are analyzed using continuum mechanics of elastic solid, viscoelastic solid, or viscous liquid, wherein the fundamental concepts such as stress-strain constitutive equations, force equilibrium, geometric compatibility must be obeyed. These models have been applied successfully to predict the cell and tissue shape changes with mechanical deformation [269-271]. By enabling the core biological processes such as cell proliferation, cell migration, cell contraction, and force transmission at the cell-cell and cell-ECM interfaces, and even molecular and subcellular scale events such as the turnover of cell adhesion and cytoskeleton, such multiscale models can recapitulate more complicated mechanosensitive behaviors such as collective cell migration and morphogenesis [272-276].

Down to the scale of subcellular structures and molecules, there are much more variations on the computational approaches developed to interpret mechanosensitive responses of live cells, such as cell shape change, cell migration, and cell contraction. In these models, a variety of mechanisms including biophysics and thermodynamics are incorporated to recapitulate the experimental findings (see the Ref. [277] for the continuum-based modeling approaches). For example, Oakes et al. used a contractile gel model [194, 278] to recapitulate cell shape changes and cell contraction during cell division and polarization [279]. The authors found that it is essential to incorporate a uniform line tension along the cell edge in addition to the contractile gel model so that the modeling results could recapitulate the elastic energy, cell contraction, and traction force distribution [279]. This finding raised an interesting question about the origin of this line tension and its molecular mechanism that could possibly affect the morphological behaviors of cells. In contrast, Tee. et al. treated a cell as a network of actin filaments, where the

radial fibers were modeled as elastic rods originated from focal adhesions at the cell peripheral and polymerized toward cell center, and transverse fibers as active contractile elements that bind the radial fibers and could slide on them [280]. By incorporating the cross-linker proteins including formin and α-actinin into the model, Tee et al. demonstrated that cellular chirality arose from the formin and α-actinin dependent self-organization of actin cytoskeleton [280]. In another study, Elosegui-Artola et al. observed that talin depletion changed the force-ECM rigidity relation from linear to biphasic. With the knowledge that talin unfold under force *in vitro* and bind to vinculin, Elosegui-Artola et al. coupled the talin unfolding dynamics to a theoretical clutch model and successfully constructed a predictive physical model of the actin-talin-integrin-fibronectin clutch for the force transmission and transduction [281]. Last but not least, Livne et al. developed a novel energy method based on the molecular and physical properties of stress fiber and FAs to explain the cell reorientation under cyclic stretch. Their results agreed quantitatively with cellular reorientation dynamics and further revealed that cell reorientation was driven by the minimization process of cell's passively-stored, two-dimensional elastic energy [282].

It is intriguing to generate a multiscale and microscopic models that incorporate many mechanisms and details that might be relevant to the biological process to bridge the different length scales. However, the flexibility increases the complexity of the model and might make it difficult to pinpoint the most relevant parameters in the process. Therefore, our strategy, which is also the choice of many others, is to build a minimal model that capture the main features. Here, we describe a discrete mechano-biophysical model to explain the subcellular rheostasis and how it determines the maintenance or exit of mechanical homeostasis.

4.2 Mechano-biophysical modeling approach

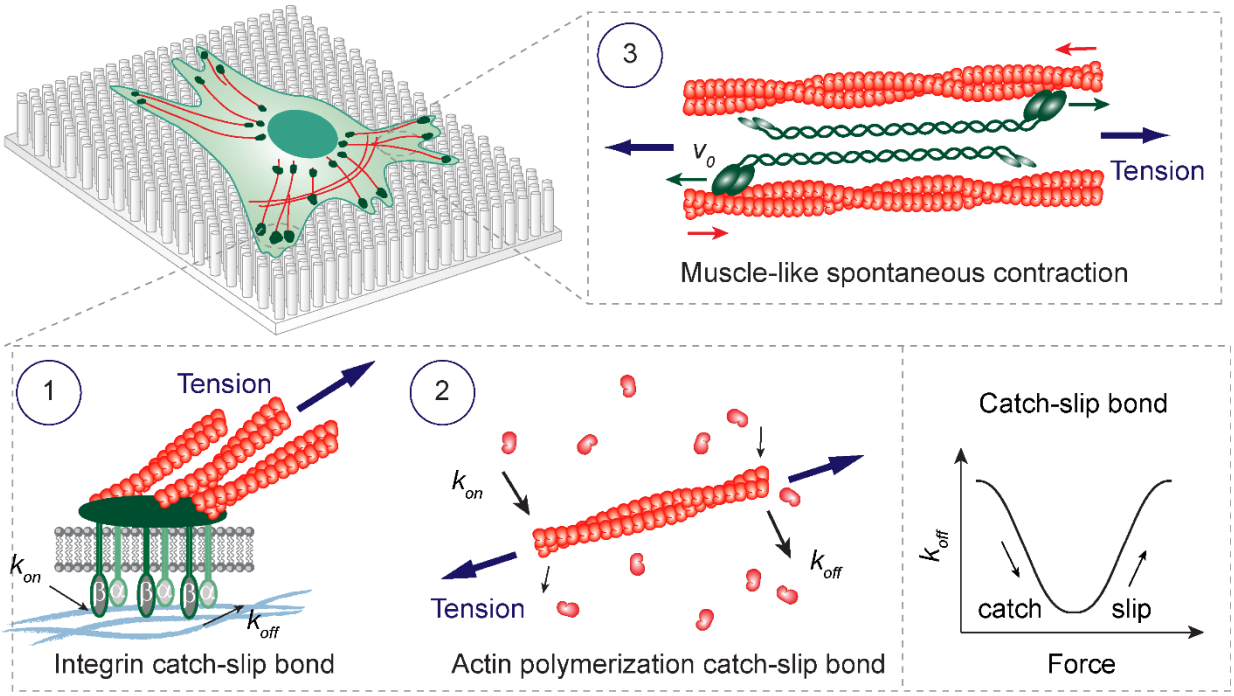

Figure 4-1 Theoretical modeling of mechanosensitive subcellular rheostasis. Illustration of three key mechanisms incorporated in the theoretical framework, including (1) catch-slip bonds in integrin, (2) catch-slip bonds in F-actin and (3) muscle-like spontaneous contractility driven by myosin motor activity.

In light of the experimental findings described in **Chapter 3**, the biophysical model characterizing the dynamics of subcellular CSK tension and FA upon cell stretch was comprised of three key mechanisms (**Figure 4-1**): (1) integrin catch-slip bond (**Figure 4-2 a**) [265], which was shown in this work as required for FA rheostasis (**Figure 3-10**); (2) F-actin catch-slip bond (**Figure 4-2 b**) [283], to recapitulate catch-slip-like behaviors in the FA-CSK mechanical network; and (3) myosin motor activity[284], which drives muscle-like spontaneous contraction in response to external forces and was shown as required for FA rheostasis (**Figure 3-8 g-i**).

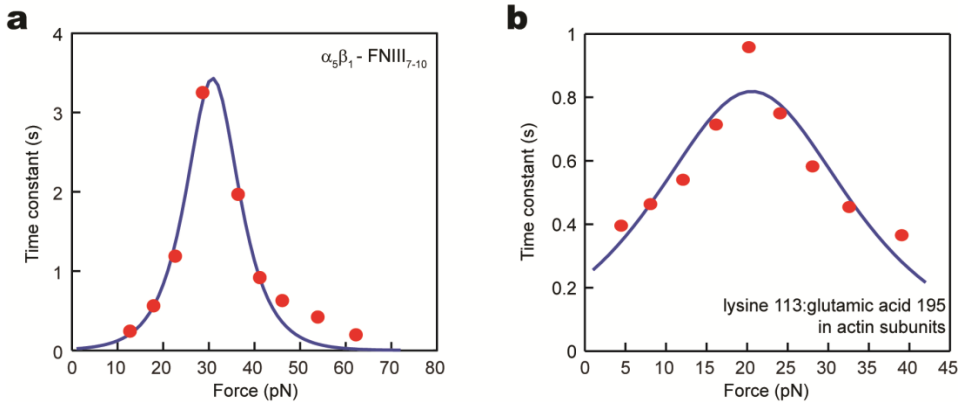

Figure 4-2 Catch-slip-bond-like behaviors in the FA-CSK network. Bonds between integrin $\alpha_5\beta_1$ and fibronectin FNIII$_{7\text{-}10}$ (**a**), and bonds between lysin113 and glutamic acid 195 in F-actin (**b**) have been demonstrated catch-slip-bond-like in vitro featuring an increase of the dissociation lifetime with loading force ("catch") followed by a decrease as expected in normal bonds ("slip") [265, 283]. Red dots in **a** and **b** were experimental results from Kong *et al.*[1]and Lee *et al.*[2], respectively. Two-pathway model (Equ. (4.3) and (4.6)) was used for fitting experimental data to determine the best-fit parameters of $\phi_{FA,s}$, $\phi_{FA,c}$, f_{FA}^{*}, $\phi_{ACT,s}$, $\phi_{ACT,c}$, and f_{ACT}^{*}.

4.2.1 Integrin catch-slip bond

Force dependent association and dissociation of FA molecules were analyzed using a model described previously ('*Novikova-Storm* model' [285]) featuring a catch-slip bond between integrin $\alpha_5\beta_1$ and fibronectin FNIII$_{7\text{-}10}$[265]. Temporal evolution of FA size was thus expressed as

$$\frac{dN_{FA}}{dt} = k_{FA,on}\left(N_{FA}^{tot} - N_{FA}\right) - k_{FA,off}\cdot N_{FA} \tag{4.1}$$

, where N_{FA} represented the total number of integrin molecules contained in FA, N_{FA}^{tot} denoted the total number of integrin molecules available in the neighboring cytosol, and $k_{FA,on}$ and $k_{FA,off}$ were the association and dissociation rates of a single integrin catch-slip bond, respectively. For simplicity, $k_{FA,on}$ was assumed independent of force and was calculated as

$$k_{FA,on} = k_{FA,o} \cdot \gamma_{FA} \tag{4.2}$$

, where γ_{FA} was a dimensionless rate constant and $k_{FA,o}$ was a reference rate. $k_{FA,off}$ was characterized by a force-dependent function using a two-pathway model [286]

$$k_{FA,off} = k_{FA,o}\left[\exp\left(\frac{f}{f_{FA}^{*}} - \phi_{FA,s}\right) + \exp\left(-\frac{f}{f_{FA}^{*}} + \phi_{FA,c}\right)\right] \tag{4.3}$$

, where f denoted the force acting on a single integrin molecule, f_{FA}^{*} was a reference force for normalization, and $\phi_{FA,c}$ and $\phi_{FA,s}$ represented zero-force dissociation rates associated with the catch and slip portions of integrin catch-slip bond dynamics, respectively. Assuming that the total force exerted on individual FA cluster, F_{tot} was uniformly distributed on each single integrin molecule, an ordinary differential equation governing the dynamic evolution of FA size, N_{FA} was obtained as

$$\frac{dN_{FA}}{dt} = k_{FA,o}\left\{\gamma_{FA}\left(N_{FA}^{tot} - N_{FA}\right) - N_{FA}\left[\exp\left(\frac{F_{tot}}{f_{FA}^{*} \cdot N_{FA}} - \phi_{FA,s}\right) + \exp\left(-\frac{F_{tot}}{f_{FA}^{*} \cdot N_{FA}} + \phi_{FA,c}\right)\right]\right\} \tag{4.4}$$

4.2.2 Catch-slip bond of F-actin

Force-dependent association and dissociation of G-actin with F-actin have been demonstrated to follow a catch-slip bond model [283]. The association and dissociation rates of G-actin with F-actin $k_{ACT,on}$ and $k_{ACT,off}$ were thus written as

$$k_{ACT,on} = k_{ACT,o} \cdot \gamma_{ACT} \tag{4.5}$$

and

$$k_{ACT,off} = k_{ACT,o}\left[\exp\left(\frac{f}{f_{ACT}^{*}} - \phi_{ACT,s}\right) + \exp\left(-\frac{f}{f_{ACT}^{*}} + \phi_{ACT,c}\right)\right] \tag{4.6}$$

, respectively, where γ_{ACT} was a dimensionless rate constant, $k_{ACT,o}$ was a reference rate, f denoted force acting on F-actin, f_{ACT}^{*} was a reference force for normalization, and $\phi_{ACT,c}$ and $\phi_{ACT,s}$ represented zero-force dissociation rates associated with the catch and slip portions of F-actin catch-slip bond, respectively.

Given force balance and force transmission across the mechanical linkage between the actin CSK and FA, the total force acting on actin stress fibers was also denoted as F_{tot}. Actin stress fibers were modeled as bundled F-actin filaments with each filament comprising actin monomers connected in series. Assuming a uniform force distribution in stress fibers and that each F-actin filament in stress fibers was connected to one integrin molecule in FA, the force acting on each actin monomer along a F-actin filament was obtained as F_{tot} / N_{FA}. The ordinary differential equation governing dynamic evolution of the total number of actin monomers N_{ACT} in actin stress fibers was thus written as

$$\frac{dN_{ACT}}{dt} = k_{ACT,o}\left\{\gamma_{ACT}\left(N_{ACT}^{tot} - N_{ACT}\right) - N_{ACT}\left[\exp\left(\frac{F_{tot}}{f_{ACT}^{*} \cdot N_{FA}} - \phi_{ACT,s}\right) + \exp\left(-\frac{F_{tot}}{f_{ACT}^{*} \cdot N_{FA}} + \phi_{ACT,c}\right)\right]\right\} \tag{4.7}$$

Of note, the integrin catch-slip bond and the F-actin catch-slip bond used in the current theoretical framework could be readily generalized to incorporate other molecular machineries residing in FA and the actin CSK that exhibit catch-slip bond behaviors. For example, Equ. (4.4)

could also be applied directly to describe force-dependent catch-slip-like behaviors of vinculin [180, 287], another FA protein. In addition, Equ. (4.7) could be used directly to describe force-dependent, catch-slip-like recruitment of actin-binding scaffold proteins, such as filamin and α-actinin [264, 288], onto F-actin filaments, which could further modulate mechanical properties of actin stress fibers as in Equ. (4.8) below.

4.2.3 Muscle-like spontaneous contraction upon external force stimulation

Cell stretch-induced changes of CSK tension on stress fibers could be simulated using a contractile element (CE)-spring model [289, 290]. Thus, to simulate cell stretch on the stretchable micropost array membrane, a mechanical model was developed that comprised a spring representing a PDMS micropost in series with another spring and a CE representing actin stress fiber containing myosin motor proteins arranged in parallel (**Figure 4-3**). The effective spring constant K_{eff} of the model was given by $1/K_{eff} = 1/K_{post} + 1/K_{SF}$, where K_{post} and K_{SF} were the spring constants of the PDMS micropost and actin stress fiber, respectively. The total force F_{tot} was thus calculated as $F_{tot} = K_{eff} [L – (L_0 + \Delta L)]$, where L was the length of activated CE-spring assembly under external force, L_0 was the length of inactivated and tension-free CE-spring assembly, and ΔL was the length change driven purely by myosin motor protein activity. ΔL would be negative for shortening and positive for lengthening of actin stress fiber, respectively. Temporal evolution of F_{tot} was then calulcated as $dF_{tot}/dt = K_{eff} (dL/dt – d\Delta L/dt)$, where dL/dt was determined from cell stretches on the stretchable micropost array membrane and $d\Delta L/dt$ was derived from a linear force-velocity relation simiplified from the *Hill*'s muscle model $F_{tot} = N_{MYO} \cdot f_{stall} [1 + (d\Delta L/dt) / v_0]$ [284, 291], where N_{MYO}, the

number of myosin molecules on actin stress fiber, was assumed proportional to the total nubmer of actin monomers N_{ACT} (i.e., $N_{MYO} = c \cdot N_{ACT}$; c was a constant), f_{stall} was the myosin stall force, and v_0 was the equivlant sliding velocity of myosin. Together, the governing equation for spontaneous muscle-like contraction of actin stress fiber when $t > 0$ was expressed as

$$\frac{dF_{tot}}{dt} = \left(K_{post}^{-1} + K_{SF}^{-1}\right)^{-1} \cdot \left[\frac{dL}{dt} - v_o\left(\frac{F_{tot}}{c \cdot f_{stall} \cdot N_{ACT}} - 1\right)\right] \tag{4.8}$$

Equations (4.4), (4.7), and (4.8) formed a complete set of equations needed for calculating temporal variations of FA size N_{FA}, the total number of actin monomers in actin stress fiber N_{ACT}, and the total force exerted on FA F_{tot}, when responding to external cell stretches.

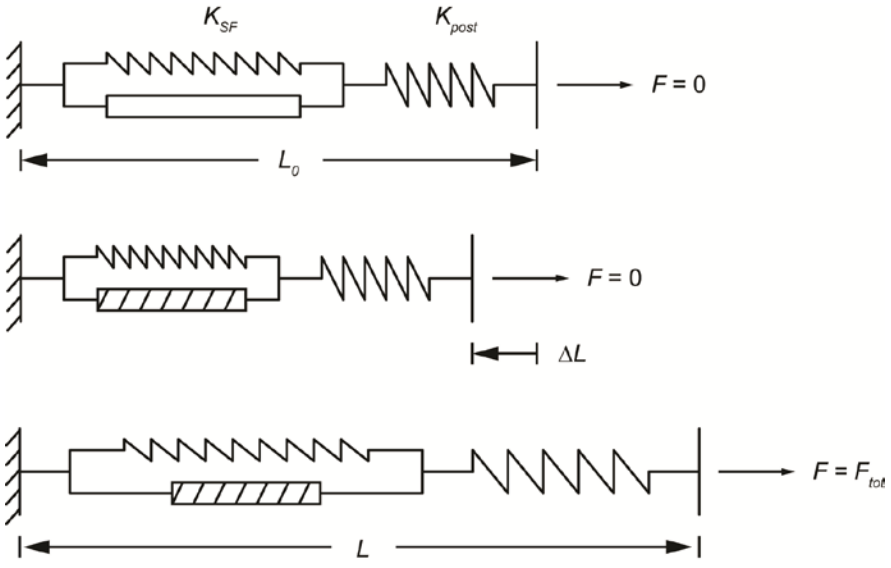

Figure 4-3 Contractile element (CE)-spring model for analyzing muscle-like spontaneous contraction of actin cytoskeleton (CSK). The model comprised a spring representing a PDMS micropost (with a spring constant K_{post}) in series with another spring (with a spring constant K_{SF}) and a CE arranged in parallel representing actin stress fibers with myosin motor proteins. The model had a nominal length of L_o when it was unloaded with the external load $F = 0$ and myosin motor proteins inactivated. Myosin motor protein activation would induce adaptive contraction of

stress fibers with a change of length ΔL (negative for shortening and positive for lengthening) under a hypothetical load-free state. Under an external force F_{tot}, the model would reach its mechanical equilibrium with a new equilibrium length L.

4.2.4 Steady-state solution of the biophysical model for cells at the ground state

The ordinary differential equations governing force dependent dynamic evolutions of FA size N_{FA} (Equ. (4.4)) and the total number of actin monomers N_{ACT} (Equ. (4.7)) allowed us to calculate steady-state solutions describing the relationship between CSK tension, FA size, and actin stress fiber for cells at the ground state. Setting $dN_{FA} / dt = 0$ in Equ. (4.4) allowed calculations of steady-state solutions for Equ. (4.4) as

$$F_{tot} = N_{FA} \cdot f_{FA}^{*} \left\{ \phi_{FA,\max} + \cosh^{-1} \left[\frac{\gamma_{FA} \left(N_{FA}^{tot} - N_{FA} \right)}{2\alpha_{FA} \cdot N_{FA}} \right] \right\} \tag{4.9}$$

and

$$F_{tot} = N_{FA} \cdot f_{FA}^{*} \left\{ \phi_{FA,\max} - \cosh^{-1} \left[\frac{\gamma_{FA} \left(N_{FA}^{tot} - N_{FA} \right)}{2\alpha_{FA} \cdot N_{FA}} \right] \right\} \tag{4.10}$$

, where $\alpha_{FA} = \exp (\phi_{FA,c} / 2 - \phi_{FA,s} / 2)$ and $\phi_{FA,max} = (\phi_{FA,c} + \phi_{FA,s}) / 2$. Equ. (4.9) and Equ. (4.10) plotted as dashed and solid curves, respectively, in **Figure 4-4 a** with N_{FA} and F_{tot} as the *x*- and *y*-axes, respectively, divided the plot into three different regions, where dN_{FA}/dt was positive in the area enclosed by the two curves (*region i*) and negative outside the area (*region ii* and *iii*). Individual FAs with a transient state falling in *region i* and *ii* would be capable of restoring their equilibrium states on the solid curve by recruiting and clustering new FA proteins

and modulated FA disassembly, respectively. In contrast, individual FAs in *region iii* were unstable and would rapidly disassemble and be completely dissolved. Together, Equ. (4.10) provided a stable steady-state solution and was used for theoretical calculations of steady-state conditions under different drug treatment conditions (**Figure 4-4**).

Of note, when external perturbations were mild, CSK tension and FA were capable of self-adaptation to restore their stable equilibrium states in a quasi-static manner. Here, stability of self-adaptation of CSK tension and FA was limited by the end point of theoretical curves calculated from Equ. (4.10), beyond which stable steady-state solutions became unavailable and FA would undergo rapid disassembly.

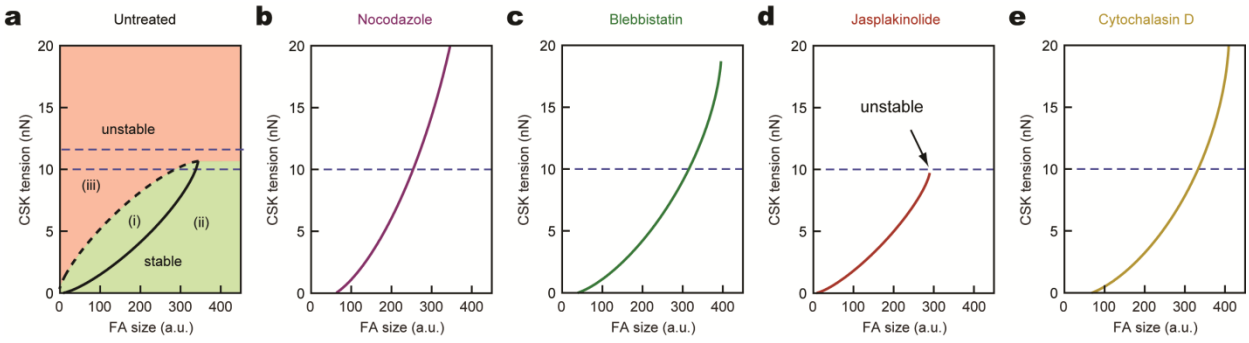

Figure 4-4 Modeling results of FA stability under tension. (**a**) Steady-state analysis of the CSK tension and FAs using the parameters for the untreated control condition. The two steady state solutions (Equ. (4.9): *dashed black* curve; Equ. (4.10): *solid black* curve) to the ordinary differential equation governing force-dependent dynamic evolution of FA size N_{FA} (Equ. (4.4)) devided the two-dimensional space with N_{FA} and F_{tot} as the *x*- and *y*-axes, respectively, into stable *region i* and *ii* and unstable *region iii*, as illustrated in a. The steady-state solution corresponding to Equ. (4.9) was at the boundary between unstable and stable regions, and any fluctuation from this boundary could either regress to the stable steady-state curve (*region i*; *solid black* curve) or diminish to zero (*region iii*). The steady-state solution corresponding to Equ. (4.10) was stable, since transient states falling into *region i* and *region ii* would be driven by the governing equation to pull back to itself. The transient state falling into *region iii* from the stable steady-state solution would also lead to a rapid disassembly of FA. Therefore, stability of the CSK-FA system was limited by the end-point of the stable steady-state curve. (**b-e**) Dependence of steady state solutions on the CSK integrity. Using the parameters corresponding to the small molecule inhibitor

treated conditions (see **Section 4.2.5**), the steady-state solution curves as well as the stability of FA under CKS tension were changed. For example, FA bearing 10 nN CSK tension was stable in untreated cells (**a**); however, it became unstable in jasplakinolide-treated cells (**d**). In the untreated condition, FA cannot bear force at 12 nN (**a**).

Similarly, a stable steady-state solution for Equ. (4.7) was obtained as

$$F_{tot} = N_{FA} \cdot f^*_{ACT} \left\{ \phi_{ACT,\max} - \cosh^{-1}\left[\frac{\gamma_{ACT}\left(N^{tot}_{ACT} - N_{ACT}\right)}{2\alpha_{ACT} \cdot N_{ACT}} \right] \right\} \tag{4.11}$$

, where α_{ACT} = exp ($\phi_{ACT,c}$ / 2 – $\phi_{ACT,s}$ / 2) and $\phi_{ACT,max}$ = ($\phi_{ACT,c}$ + $\phi_{ACT,s}$) / 2 . Equ. (4.10) and Equ. (4.11) together defined stablilty of the FA-CSK tension system and provided stable steady-state solutions for N_{FA} , N_{ACT} , and F_{tot} at ground states.

4.2.5 Determination of model parameters

Equations (4.10) and (4.11) provided a stable solution space for N_{FA} , N_{ACT} , and F_{tot} at ground states. Parameters including N^{tot}_{FA} and N^{tot}_{ACT} were selected to ensure F_{tot} covering a physiologically relevant range from 0 - 10 nN as observed in experiments with REF-52 fibroblasts (**Figure 3-3 e**). Parameters for integrin and F-actin catch-slip bonds including f^*_{FA}, $\phi_{FA,s}$, $\phi_{FA,c}$, f^*_{ACT} , $\phi_{ACT,s}$, and $\phi_{ACT,c}$ were determined by fitting experimental data reported previously [265, 283] using Equ. (4.3) and Equ. (4.6) with $k_{FA,o}$ and $k_{ACT,o}$ set to 1 s^{-1} (**Figure 4-2** and **Table C.1**). K_{post} was determined using finite element analysis, and K_{post} = 7.2 nN μm^{-1}. K_{SF} was estimated by assuming actin stress fibers as solid ropes with a rope length of 60 μm (L; t < 0), a rope diameter of 1 μm, and a modulus of 12 kPa [292, 293]. Myosin stall force f_{stall} was

selected to match experimental results reported previously [294], and the equivalent sliding velocity of myosin molecules v_o was set as 1/10 of the value measured for a single myosin molecule sliding on unloaded F-actin [295], to compensate discontinuous myosin sliding on F-actin (power stroke duty ratio). Value of the constant c in Equ. (4.8) was determined by fitting quasi-static values of the total force F_{tot} exerted on FA obtained experimentally with REF-52 fibroblasts. A complete list of model parameters was provided in **Table C.1**.

4.2.6 Theoretical validation of the indispensability of catch-slip bonds and myosin motor activity

To examine whether integrin catch-slip bond would be indispensable for theoretical recapitulation of subcellular rheostasis of CSK tension and FA, Equ. (4.4) was modified to remove the catch-bond portion of the integrin catch-slip bond as

$$\frac{dN_{FA}}{dt} = k_{FA,o}\left[\gamma_{FA}\left(N_{FA}^{tot} - N_{FA}\right) - N_{FA}\cdot\exp\left(\frac{F_{tot}}{f_{FA}^{*}\cdot N_{FA}} - \phi_{FA,s}\right)\right] \tag{4.12}$$

Equations (4.7), (4.8), and (4.12) formed a complete set of equations needed for calculating temporal evolutions of FA size N_{FA}, the total number of actin monomers in actin stress fiber N_{ACT}, and the total force exerted on FA F_{tot}, when responding to external cell stretches with pure slip bonds between integrin and fibronectin.

In distinct contrast to the stable steady-state solution in **Figure 4-4 a** that allowed spontaneous restoration of CSK tension and FA to their stable equilibrium states under small perturbations, the only steady-state solution to Equ. (4.12) expressed as

$$F_{tot} = N_{FA} \cdot f_{FA}^{*} \left\{ \phi_{FA,s} + \ln \left[\frac{\gamma_{FA} \left(N_{FA}^{tot} - N_{FA} \right)}{N_{FA}} \right] \right\} \tag{4.13}$$

was unstable for majority of its solution space (**Figure 4-5 a**). Specifically, the steady-state solution curve described by Eq. (4.13) was biphasic and divided a two-dimensional surface with N_{FA} and F_{tot} as the x- and y-axes, respectively, into three different regions, where $\mathrm{d}N_{FA}/\mathrm{d}t$ was positive underneath the curve (*region i*) and negative above the curve (*region ii* and *region iii*). Individual FAs with a transient state falling into *region i* and *region ii* would approach equilibrium states on the *solid* portion of the theoretical curve where FA size were unrealistically large and FA size and CSK tension became negatively correlated (contradictory to experimental observations). FAs on the rest part of the steady-state solution curve (*dashed* line) were unstable: they would either be completely dissolved or grow to its maximum size when perturbed to fall into *region iii* or *region i*, respectively. Such hypersensitivity of the FA-CSK tension system without catch bonds was also revealed in simulations of dynamic responses of CSK tension and FAs upon cell stretch. Majority of FAs disassembled instantaneously upon cell stretch, while those survived in the initial phase grew to its maximum regardless of CSK tension force, contradictory to experimental observations of subcellular rheostasis of CSK tension and FA (**Figure 4-5 b,c**).

The necessity of myosin motor activity for subcellular rheostasis of CSK tension and FA was investigated by removing it from Equ. (4.8), resulting in a modified Equ. (4.8) with only elastic properties as $dF_{tot}/dt = \left(K_{post}^{-1} + K_{SF}^{-1} \right)^{-1} \cdot dL/dt$. Simulation results using this modified equation recapitulated reinforcements of both CSK tension and FA in *Phase I* of the homeostatic

response, but failed to predict subcellular rheostasis in *Phase II* of the homeostatic response (**Figure 4-5 d-f**).

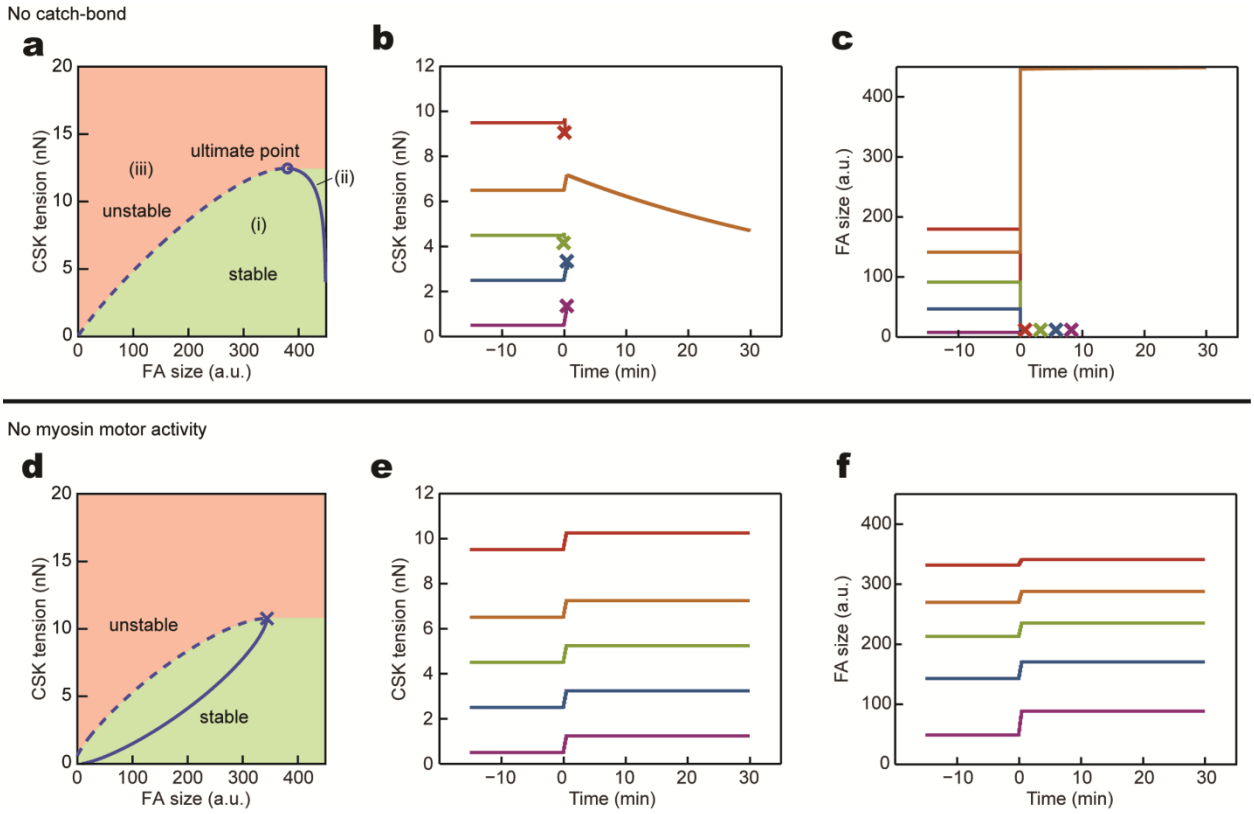

Figure 4-5 Indispensability of catch-slip bond and myosin motor activity in mediating mechanosensitive rheostasis of subcellular CSK tension and FAs. Dynamic responses of CSK tension and FA to static cell stretch were simulated using a modified biophysical model without the catch-bond portion of the integrin catch-slip bond (**a-c**) or myosin motor activity (**d-f**). (**a-c**) Stable steady-state solution of CSK tension *vs.* FA (solid blue curve) obtained from the modified model without the catch-bond portion of the integrin catch-slip bond would suggest ground-state values of FA unrealistically large and independent of CSK tension. Small perturbations to the CSK-FA system on the unstable portion of the steady-state curve (dashed blue curve) would result in FAs to either be completely dissolved or grow to its maximum size when perturbed to fall into *region iii* or *region i*, respectively. Such hypersensitivity of the CSK-FA system without catch bonds would also lead to spontaneous disassembly of majority of FAs upon cell stretch (**b&c**). FAs surviving from the initial phase would grow to its maximum size regardless of CSK tension (**c**), contradictory to experimental observations of subcellular rheostasis of CSK tension and FA. (**d-f**) Theoretical modeling without considering myosin motor activity. Steady-state solution of CSK tension *vs.* FA obtained from the modified model was not affected by the removal of myosin motor activity in theoretical modeling. However, upon cell stretch, both CSK tension (**e**) and FA size (**f**) could only

demonstrate reinforcement in *Phase I*, but not exhibiting rheostatic behaviors (reinforcement or relaxation) during *Phase II*.

The model source code is available upon request.

4.3 Modeling results and discussion

The modeling results generated from the mechano-biophysical model clearly provided a three-dimensional space for temporal evolutions of CSK tension and FA size during single-cell homeostasis (**Figure 4-6 a**). FAs with different initial size and bearing force at the ground state followed different paths to converge after the onset of mechanical stimulation (**Figure 4-6 a**). This mechanosensitive behavior qualitatively recapitulated mechanosensitive rheostatic dynamics of both CSK tension and FA and its dependence on their respective ground-state values in the experiment (**Figure 3-5 e&f**). Meanwhile, the temporal evolution of CSK tension and FA during subcellular rheostasis followed closed to the steady-state solution surface of CSK tension *vs.* FA size generated from the biophysical model (**Figure 4-6 a**, translucent *blue* surface), which demonstrated the linear correlation between CSK tension and FA size as is observed in experiment (**Figure 3-4 a-d**) was an intrinsic property of FAs with a quasi-static load below a threshold.

Excitingly, by directly adapting data from previous experimental studies [265, 283, 292-295] as well as fitting model parameters using ground-state values ($t < 0$ min) of CSK tension and FA size (see **4.2.5 Determination of model parameters** and **Table C.1**), our model quantitatively predicted mechanosensitive rheostatic behaviors ($t > 0$ min) of CSK tension and

FA in REF-52 fibroblasts in response to 8% cell stretch (**Figure 4-6 b&c**). By modifying stretch magnitude from 8% to 4% and 16%, respectively, while keeping all other model parameters unchanged, theoretical simulations further successfully recapitulated subcellular rheostasis of CSK tension and FA under different cell stretch levels (**Figure 4-6 d&e**). The most important feature of the subcellular rheostatic pattern in 16% stretch that FAs bearing high force had a monotonic relaxation without an immediate reinforcement phase after the onset of cell stretching (**Figure 3-5 c&d**) was also recapitulated in the modeling results as there was no convergent numerical result for this group (**Figure 4-6 e**, *red* curve and *black* cross). The stability analysis in **Figure 4-4 a** also confirmed that the fast disassociation of FAs and the force relaxation was the consequence of FA instability. The comparison between the modeling results for 4%, 8%, and 16% stretch also revealed that the stretch severity influenced the passive responses of FA and CSK tension in *Phase I* that could even induce the fast disassembly of FAs and releasing of load due to the limited FA stability, but not on the rate of relaxation and reinforcement in *Phase II* (**Figure 4-6 f&g**).

Using ground-state data to fit and simulate effects of inhibitor treatments on different model parameters (**Table C.1**), we further achieved quantitative simulations of experimental results from inhibitor-treated cells (**Figure 4-7 a-d**, **Figure 3-7**). Single-parameter studies using the biophysical model to mimic the effects of specific inhibitors also supported the important roles of microtubule-mediated FA disassembly, myosin motor activity, and actin polymerization in selectively biasing mechanosensitive FA rheostasis (**Figure 4-7 e-h**). Specifically, we set the change of the total number of integrin molecules contained in FA, dN_{FA} nonnegative to mimic the effect of nocodazole *ex vivo* that blocks FA disassembly. The modeling results, in comparison with the untreated control, did not influence the subcellular rheostasis of CSK

tension, but completed abolished FA disassembly in *Phase II* (**Figure 4-7 e**). To mimic the effect of blebbistatin that inhibits myosin II activity, we reduced equivalent unloaded sliding velocity of myosin, v_0 by 40%, and its effect was reflected in the lowered rate of reinforcement and relaxation of CSK tension and FAs in *Phase II* in rheostasis (**Figure 4-7 f**). This is consistent with our virtual experiment in **Figure 4-5 b** in which the myosin motor activity was deleted, and there was no reinforcement nor relaxation in *Phase II*. For jasplakinolide and cytochalasin D that enhances and inhibits actin polymerization, respectively, we tuned the non-dimensional association rate for actin, γ_{ACT} accordingly (**Figure 4-7 g&h**). In contrast to parameter v_0 for myosin that changed the rate of reinforcement and relaxation, the parameter γ_{ACT} was associated with the converging plateau for both CSK tension and FAs. Increased γ_{ACT} for jasplakinolide elevated the converging plateau (**Figure 4-7 g**), while decreased γ_{ACT} for cytochalasin D decreased it (**Figure 4-7 h**). The modeling result for jasplakinolide, as same the one under 16% stretch, also suggested that abolished reinforcement of FA size with high ground-state values in *Phase I* was attributable to an instability-like phenomenon, where the steady-state solution curve describing stable states of CSK tension and FA was not available beyond a threshold (**Figure 4-4 d**, **Figure 4-7 h**).

We further used modified integrin catch-slip-bond parameters upon TS2/16 treatment (**Figure 4-8 a**) to simulate the effect of impaired catch-slip bond activities on subcellular rheostasis. The theoretical model successfully predicted a decrease and an increase in the ground-state whole-cell average of CSK tension and FA size, respectively (**Figure 4-8 c&d**), which was consistent with experimental results (**Figure 3-10 b&c**). It also suggested that the decrease in the ground-state values of CSK tension and increase in FA size respectively was a result of the right-shifted steady state curve that covered a narrow range of CSK tension but wide of FA size (**Figure 4-8 b**). Importantly, the model further recapitulated the effect of TS2/16

treatment in biasing subcellular FA rheostasis but not CSK tension, wherein only FAs with high ground-state CSK tension would demonstrate initial instability followed by rapid re-stabilization to achieve an apparently suppressed rheostasis (**Figure 4-8 e&f**, **Figure 3-10 d-g**).

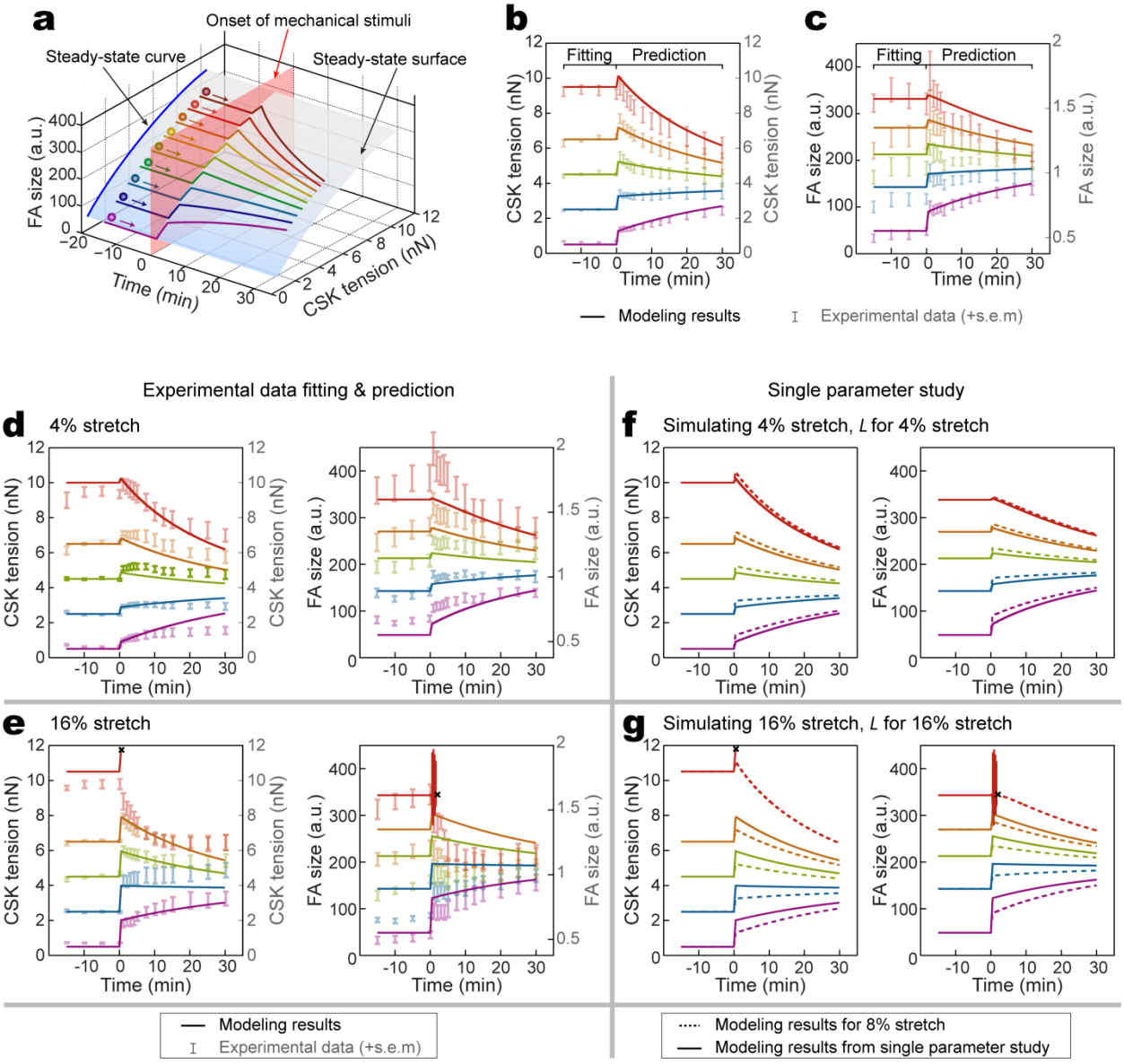

Figure 4-6 Theoretical modeling results of mechanosensitive subcellular rheostasis. (**a**) Theoretical result showing a three-dimensional, stable solution surface (*translucent blue*) for temporal evolutions of CSK tension and FA size during single-cell homeostasis. Color-coded trajectories simulated mechanosensitive rheostasis that depended on ground-state values of FA size and CSK

tension. The onset of mechanical perturbation was indicated by a translucent pink surface. (**b&c**) Theoretical results (solid curves) quantitatively agreed with experimental data (translucent error bars) for rheostatic behaviors of subcellular CSK tension (**b**) and FA size (**c**) in untreated REF-52 fibroblasts under 8% static equi-biaxial stretch. Ground-state data obtained for $t \leq 0$ min was used for fitting model parameters, which were then employed to calculate rheostatic paths for $t > 0$ min. (**d&e**) Recapitulation of mechanosensitive rheostatic behaviors of subcellular CSK tension (*left*) and FA (*right*) under 4% (**d**) and 16% (**e**) static equi-biaxial stretches using the biophysical model. Theoretical calculations were conducted using model parameters determined through fitting ground-state values of REF-52 fibroblasts ($t \leq 0$ min) under 8% stretch, except that the stretch magnitude was set as 4% and 16% as indicated. (**f&g**) Single-parameter studies to elucidate the effect of stretch level on subcellular rheostasis. Modeling results for 4% (**f**) and 16% (**g**) stretches (solid curves) were plotted together with results from 8% stretch (dashed curves) for comparison. Black crosses in **e** and **g** marked where simulations became divergent, leading to unstable solutions and implying instability of FAs (see **Figure 4-4a**).

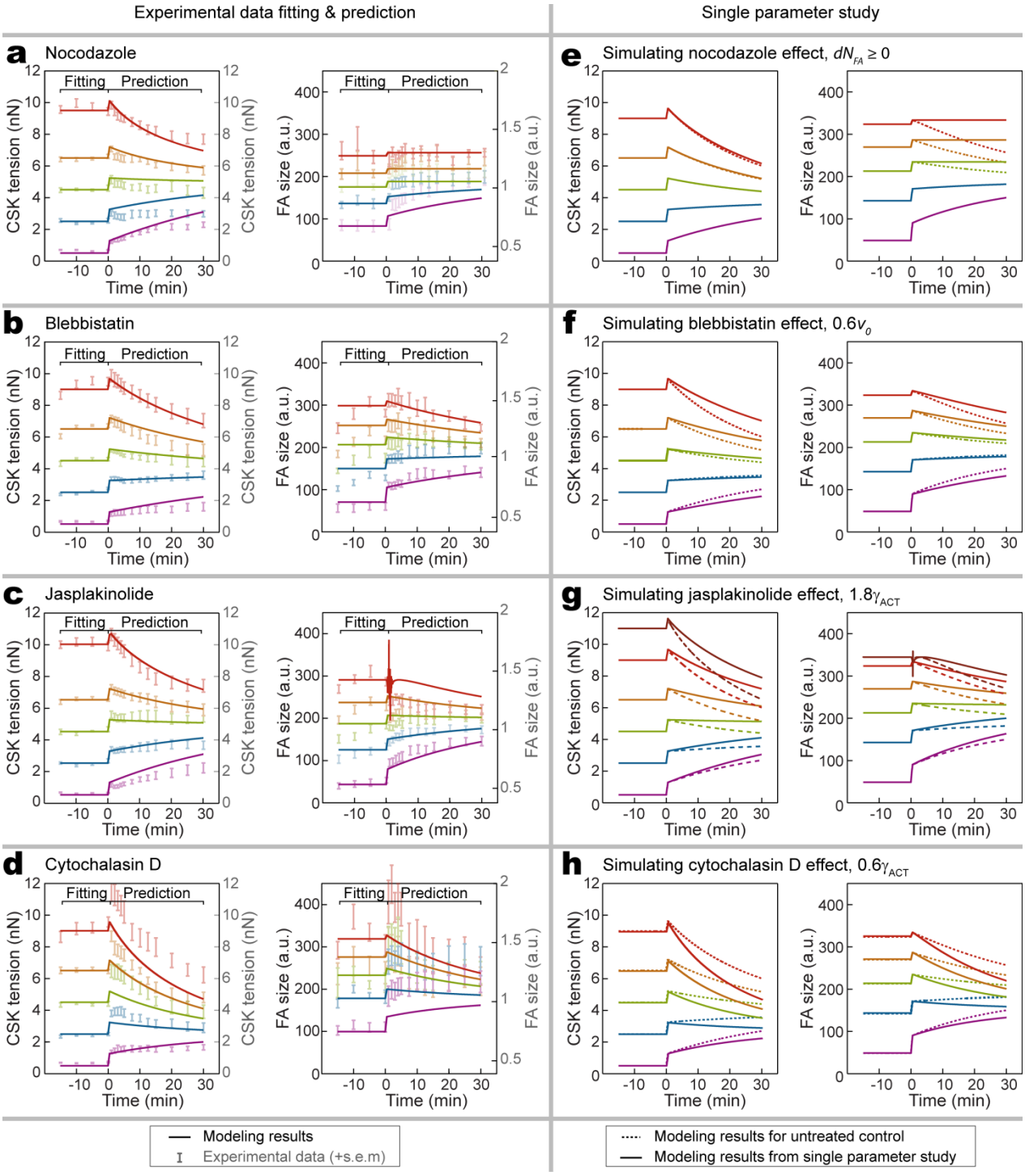

Figure 4-7 Modeling results of CSK perturbation to skew subcellular rheostasis pattern. Recapitulation and prediction of mechanosensitive rheostasis of subcellular CSK tension and FA for REF-52 fibroblasts under 8% static equi-biaxial stretch and treated with small-molecule inhibitors as indicated. (**a-d**) Theoretical calculations of rheostatic responses of CSK tension (*left*) and FA size (*right*) plotted against time (solid curves), agreeing reasonably well with experimental data (translucent error bars). Ground-state values of CSK tension and FA size obtained for $t \leq 0$ min were used for calculations of best-fit model parameters, which were then employed for

calculations of rheostatic paths for $t > 0$. (**e-h**) Single-parameter studies to theoretically elucidate the role of individual CSK components in subcellular rheostasis. Theoretical calculations of rheostatic responses of CSK tension (*left*) and FA size (*right*) were conducted using modified model parameters as indicated (solid curves). Modeling results for untreated control (dashed curves) were plotted together for comparison. In **e**, temporal change of FA size dN_{FA}/dt was set ≥ 0, to simulate the effect of nocodazole treatment on preventing FA disassembly. There was no significant change in rheostatic behavior of CSK tension. However, relaxation of FA rheostasis in *Phase II* was inhibited. In **f**, the equivalent sliding velocity of myosin motor v_o was decreased from the value for untreated control to simulate the effect of blebbistatin treatment on reducing myosin II activity, resulting in slower rheostatic responses in *Phase II* for both CSK tension and FA. In **g**, to mimic the effect of jasplakinolide, the dimensionless association rate of actin subunits γ_{ACT} was increased from the value for untreated control. The abolished initial FA strengthening in *Phase I* for FA subsets sustaining high CSK tension was due to instability of theoretical modeling (see **Section 4.2.4** and **Figure 4-4 d**). In **h**, the dimensionless association rate of actin subunits γ_{ACT} was decreased from the value for untreated control, to mimic reduced association of actin monomers onto the barbed end of actin filaments due to cytochalasin D treatment. This modification of model parameter resulted in faster relaxation yet slower reinforcement for both CSK tension and FA in *Phase II*.

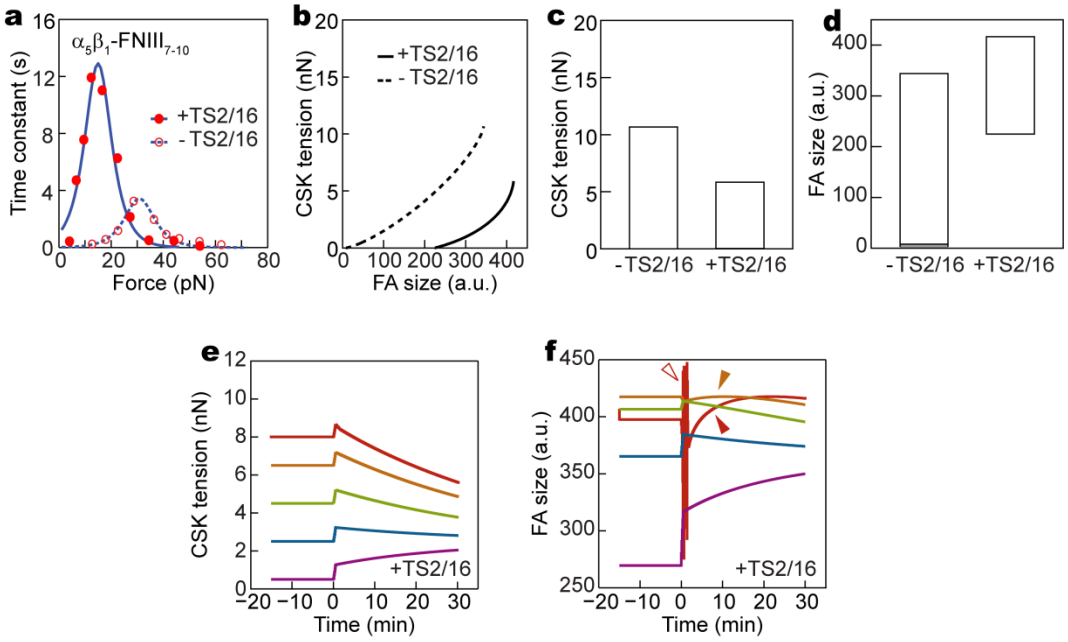

Figure 4-8 Modeling results for the catch-slip bond perturbation. Integrin catch-slip bond in regulating mechanosensitive rheostasis of subcellular cytoskeleton (CSK) tension and focal adhesion (FA) is significant. (**a**) Force - lifetime diagram of the catch-slip bond between $\alpha_5\beta_1$ integrin and $FNIII_{7\text{-}10}$, with or without treatments of integrin $\beta 1$ antibody TS2/16 as indicated (data from Ref. [11]). Treatment of TS2/16 significantly changes catch-slip bond dynamics by

shortening bond lifetime under high forces and prolonging bond lifetime at low forces. To determine catch-slip bond parameters, the two-pathway model (solid blue curve; Equ. (4.3) was used for fitting experimental data (red dots) from Kong *et al.*[265] for TS2/16-treated cells, with best-fit parameters $\phi_{FA,s}$ = 7.65, $\phi_{FA,c}$ = 0, and f_{FA}^{*} = 4.6 pN. Experimental data for untreated control as well as its associated best fitting curve generated from the two-pathway model (red open circles and dashed blue curve) were plotted for comparison. (**b**) Stable steady-state solutions of CSK tension *vs.* FA size, with or without treatments of TS2/16 as indicated. Treatment with TS2/16 modified correlations between FA size and CSK tension, and it further stabilized FA under low force but reduced the maximum CSK tension sustained by FA under steady-state conditions. (**c&d**) Theoretical predictions of changes in CSK tension (**c**) and FA size (**d**) upon TS2/16 treatment. Data was extracted from **b**. (**e&f**) Experimental results showing reduction of CSK tension (**e**) and a shift of FA size distribution toward large FAs (**f**) upon TS2/16 treatments for human mesenchymal stem cells (HUMSCs). (**g&h**) Theoretical calculations of rheostatic behaviors of CSK tension (**g**) and FA size (**h**) for TS2/16-treated cells. Best-fit parameters $\phi_{FA,s}$, $\phi_{FA,c}$, and f_{FA}^{*} obtained from **a** for TS2/16-treated cells were used for calculation, together with other model parameters determined by fitting ground-state values of CSK tension and FA size in REF-52 fibroblasts. Hollow red arrowhead indicated instability of FA response in *Phase I*, whereas solid red and orange arrowheads marked reinforcement of FA in *Phase II*.

4.4 Summary

In summary, we constructed a mechano-biophysical model in light of our experimental results that was comprised of three key mechanisms: integrin catch-slip bond as is required for FA stability, F-actin catch-slip bond for the CSK stability, and myosin motor activity that drives muscle-like spontaneous contraction in response to external forces. The theoretical model has quantitatively recapitulated experimental observations under different stretch severity and ECM-FA-CSK perturbation that clearly demonstrated it quantitative predictive power. It further led to the discovery of the mechanistic roles of force-sensitive molecular machineries including catch-slip bonds between integrin and fibronectin, and myosin motor activity in regulating homeostasis through the physical emergence of subcellular rheostasis. Via cross-examining the experimental and theoretical results, we have not only validated the assumptions and the predictive power of the theoretical model, but also showed that the mechanisms incorporated in the model were both

sufficient and necessary for recapitulating experimental findings, thus further confirmed the origin and regulation of mechanosensitive subcellular rheostatic behaviors of CSK tension and FA formation.

We claim that the governing equations derived here are capable of being readily generalized to incorporate other molecular machineries residing in the ECM-FA-CSK mechanical network that exhibit catch-slip bond like behaviors [180, 264, 287, 288] for the studies of other mechanoresponsive behaviors. We also acknowledge that this model with a minimalistic set of mechanisms are oversimplified to simulate cellular responses in a complicated mechanical environment where nonlinearity of the mechanical properties of CSK and CSK remodeling, and spatial information have to account.

Although there are many other parameters that could be incorporated into the model, our results have strongly suggested that our model contains a minimalistic set of rules that govern subcellular rheostasis. Like many other minimalistic rules built upon seemingly complex experimental data, such as the Kepler's laws of planetary motion, the theoretical model developed in the present work has provided unique insights that reveal the most essential, sometimes seemingly simplistic, mechanisms underlying complex system-level cellular dynamics. Together, this present work has underscored the significance of theoretical modeling in assisting mechanistic investigations of cell behaviors.

Chapter 5

Conclusion, perspective, and future work

5.1 Conclusions

Homeostasis is a fundamental adaptive biological process that is of utmost importance in maintaining whole-cell/tissue physiology against constant external perturbations. Cellular homeostasis to mechanical perturbation ("mechanical homeostasis") is an emerging new concept in the field of biology especially in mechanobiology, as its dysregulation has an important contribution to pathophysiological conditions such as developmental defects, cardiovascular and pulmonary diseases, and cancer [13, 98, 109, 236]. Studies on mechanical homeostasis have further provided a basic, yet exciting framework to the mechanobiology field to examine dynamic and adaptive biomechanical behaviors of mammalian cells in response to force and deformation arising both intra- and extracellularly.

In the past, homeostasis has been commonly studied at the cell, tissue, or organ levels, and the link between different length scales has not been studied and understood. For decades, the relation between collective dynamics at smaller scales and emergent system-level properties at larger scales has attracted scientists in biology, physics, and materials sciences. The beautiful living cells, which behave as adaptive autonomous systems operating through subcellular events, draw our attention. In this present work, we, for the first time, have established the missing link

between cellular mechanical homeostasis and subcellular behaviors. Here are three major accomplishments of this work.

First, we have developed a novel and powerful technological tool – the micropost array cytometry (**Chapter 2**) [85-89], which has distinct advantages over conventional cell stretching systems. With live-cell fluorescence microscopy and image analysis techniques, the micropost array cytometry is capable of applying controlled cell stretches while simultaneously reporting dynamic responses of subcellular cell contraction, FAs, actin stress fibers (see **Section Error! Reference source not found.**), and even cell stiffness with precise spatial registrations across the entire cell area. The micropost array cytometry could also be utilized for studies of other structural and signaling proteins that reside in or are associated with the ECM – FA – CSK mechanical network. This unique feature of the micropost array cytometry has enabled quantitative and statistical analysis of the ECM – FA – CSK system based on the amount of data with a high spatial resolution and subcellular registration. As shown in this dissertation, deep analysis of such data could help reveal hidden patterns of the dynamic ECM – FA – CSK system, and provide multiscale and multi-content information for theoretical modeling that further unveils hidden mechanisms, which could be extremely powerful for elucidating cellular and subcellular mechanisms for future studies. The micropost array cytometry also provides the flexibility to be integrated with other techniques such as acoustic tweezers and optogenetics, and to be implemented for other tissue cultures such as cell colonies and cell monolayer. By virtue of the simplicity of design and versatility for applications, the micropost array cytometry holds great promise as a platform for investigating mechanobiology.

Second, we have unveiled mechanosensitive subcellular rheostasis as a fundamental mechanism to drive single-cell mechanical homeostasis (**Chapter 3**) [88]. To the best of our knowledge, this is the first study to examine mechanical homeostasis of cells from a subcellular scope. The primary finding that single-cell mechanical homeostasis is an emergent phenomenon driven collectively by mechanosensitive and compensatory subcellular rheostasis of CSK tension and FA, is entirely novel and totally unexpected and unpredicted from our perspective, and has not been proposed or hypothesized in any previous publications. Specifically, we found that during single-cell homeostasis, subcellular behaviors featured a mechanosensitive pattern wherein quasi-static values of CSK tension and FA determined their distinct reactive paths ("rheostasis") via either relaxation or reinforcement to approach mechanical homeostasis. Drug treatment studies have further demonstrated an efficient exit of mechanical homeostasis through skewed subcellular rheostasis pattern. Intriguingly, we have discovered that subcellular dynamics would observe patterns different from that at the single-cell level, and thus have confirmed single-cell homeostasis as an emergent phenomenon. This idea, which has potentially revealed a general and previously underappreciated physical nature of single-cell behaviors, should inspire researchers in diverse fields (such as oncology, developmental biology, and stem cell biology) to initiate new multidimensional and interdisciplinary research studying cellular behaviors as emergent properties driven by collective dynamics at the subcellular level.

Third, we have conducted theoretical modeling based on first principles to illustrate the origin and regulation of the mechanosensitive subcellular rheostatic behaviors of cell contraction and FA dynamics [88]. Our theoretical model has quantitatively recapitulated experimental observations and further led to the discovery of functional roles of force-sensitive molecular machineries such as catch-slip bonds and myosin motor activity in regulating homeostasis

through physical emergence. The present work has underscored the significance of theoretical modeling, especially the minimal models, in assisting mechanistic investigations of cell behaviors.

5.2 Perspectives

The field of mechanobiology and mechanotransduction has been expanding rapidly over the last decades. Increasing numbers of researchers from both engineering and biology fields have started to appreciate the fact that mechanical cues from cell and tissue environments are important regulators of cell function that are important for applications in tissue engineering and regenerative medicine. These new findings also boost the fundamental studies in mechanobiology to tease out detailed genetic, epigenetic, and biochemical mechanisms of mechanosensation and mechanotransduction. However, reports are implying that we, indeed, still underestimate cellular sensitivity to their intracellular and extracellular physical environment. For instance, variations on the magnitude of cyclic stretch can significantly alter the metabolic and mechanical behaviors of smooth muscle cells [296, 297]. It also remains unclear why different cell types show different behaviors in the seemingly same mechanical environment. Although many mechanosensitive molecules and machineries have been identified, their connection, interaction, and crosstalk with other mechanotransductive pathways are still elusive.

Intuitively, mechanical attributes of cells and tissues are both causes and effects of their own mechanobiological processes. Given the complexity and sensitivity of the system, I

envision that multiscale and systematic study of cell and tissue responses to physiologically relevant physical stimuli is one of the opportunities and challenges of mechanobiology.

From the engineering side, more efforts are needed to develop biomimetic systems with spatiotemporally controlled mechanical environments. One of the promising areas of research is in biomaterial development. Most of the current studies are still using static, elastic/viscoelastic, continuous, 2D culture systems, while in reality, cells are in a dynamic, fibrillar, and 3D matrix. The other area is in complex patterns of mechanical stimulation, specifically for cell stretch and shear flow. Majority of existing studies invariably use sustained or monotonous mechanical stimuli; however, cells in the body are exposed to regularly and irregularly varying stimuli under physiological and pathological conditions. Recent work has started tackling these challenges, and discovered distinct pathways and new insights in mechanotransduction [296, 297]. These findings shed light on the need for novel tools to recapitulate the complex *in vivo* environment.

From the experimental side, biologists need to work in close collaboration with physicists and engineers to develop new techniques to control and engineer interactions between different molecules, to probe subcellular events, and to discover new phenomena. Efforts also need to be made to meet the rising need for predictive mechano-chemical biophysical models that can facilitate the identification of relevant regulatory parameters and reveal how molecular-scale activities tune the emergent cell and tissue properties.

Understanding how such mechanosensitive machineries facilitate the complex physiology of cells, tissues, and organisms remains an exciting research area. I envision that it will keep attracting more and more biologists, physicists, and engineers.

5.3 Future work

Cell memory to mechanical history has drawn attention of researchers, as it is not only relevant to a number of physiological and pathological processes, but also applicable to tissue engineering and stem cell therapy in regenerative medicine. Repeated mechanical stimulation is physiological relevant to endothelial cells, epithelial cells, smooth muscle cells, myocytes, fibroblasts, and many other cell types in the respiratory and cardiovascular systems. Cyclic stretch to cells has been shown of vital importance to cell growth, differentiation, signal synchronization, inflammatory responses, etc. [298-303]. Changes in cell mechanics after cyclic stretch have also been reported, which have been demonstrated to correlate with pathology and disease progression such as asthma [304-306]. Recent studies have also revealed that fluctuations on cycle-by-cycle cell stretching play significant regulatory roles on mechanotransduction [297]. Evidence has shown that variable cyclic stretch applied to vascular smooth muscle cells alter ATP production, cytoskeleton organization, and signaling compared with those under monotonous cyclic stress [296]. Recent study has also demonstrated that human mesenchymal stem cells possess mechanical memory of the substrates where they were cultured [307]. Long dosage of stiff substrate to mesenchymal stem cells can irreversible change their phenotype that influences the cells' fate in subsequent differentiation assays. Although the mechanisms that retain cell memory to the mechanical history are largely elusive, it is becoming clear that mechanical history impacts the epigenetic, metabolic, and mechanical properties of cells via regulating the fundamental mechanosensation and mechanotransduction.

Recently, single-molecule studies by the Zhu group and others have found that the lifetime of receptor-ligand bonds mediating cell adhesions and subjected to force transmission

depends not only on the magnitude of force, but also on the force loading rate and history of force application [178, 308]. For example, catch-slip bond-like integrin-ligand interaction under cyclic forces was reinforced via a memory-like mechanism that accumulates over repeated cycles [308]. The lifetime of integrin-fibronectin bond at low force increased around 10-fold after repeated cell stretch and relaxation. Chen et al. constructed catch-slip bond models by adopting different "catching" mechanisms, and theoretically demonstrated that the bonds, although having similar force-lifetime profile upon a constant force, have a differential dependency on the loading rate, force history, and even the clustering of bonds [309].

The results from single-molecule studies have suggested that cells might memorize the history of mechanical stimulations and adapt via the broadened ECM – FA – CSK mechanical linkage, which functions as an adaptive structure retaining non-genetic cell memory to mechanical history.

Based on the work described in the dissertation, micropost array cytometry (**Chapter 2**) can be used to apply repeated cell stretch and relaxation cycles and to measure cellular responses, and cellular mechanical homeostasis on CSK tension and FAs (**Chapter 3**) can be used as a measure to examine cell memory to mechanical history. It would be interesting to examine whether cellular homeostasis and subcellular rheostasis of CSK tension and FAs depend on mechanical history. If yes, is it associated with a reinforcement in the ECM – FA – CSK mechanical linkage and has similar responses as integrins in the single molecule study? If not, what is the feedback mechanism that prevents cells from a continuous reinforcement of ECM – FA – CSK mechanical linkage as observed on integrin molecules *in vitro* (**Figure 5-1**)? Mechano-biophysical model can be modified from the one described in **Chapter 4** to

accommodate changes in molecular binding dynamics as observed in single-molecule studies, and cross-examining modeling results and experimental findings could potentially reveal the link to phenotypical and morphological changes of cells with repeated mechanical stimuli.

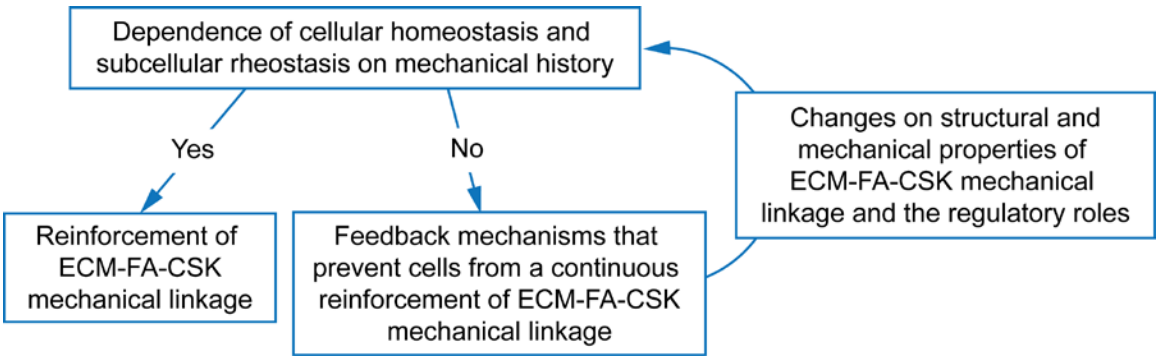

Figure 5-1 Illustration showing the steps for the study of cell memory to the mechanical history.

To connect molecular dynamics, subcellular rheostasis, and cellular homeostasis, multiscale and systematic study should be performed to identify potential changes on the structural and mechanical properties of the ECM – FA – CSK mechanical linkage and its regulatory roles on cell memory (**Figure 5-1**). For this purpose, it would be critical to add the actin CSK into the framework, as it is one of the most important contributors to cell mechanics and mechanotransduction.

As introduced briefly in **Chapter 1**, actin CSK forms a complex network interlinking filaments and molecules that extend from the nucleus to the plasma membrane. It provides a dynamic scaffold for the organization of intracellular contents and for transportation of vesicles and organelles intracellularly. It also connects cells with their extracellular microenvironment both physically and biochemically for cell-cell and cell-ECM communication [15, 17, 22, 23, 74].

Moreover, the CSK generates coordinated forces that not only enable the cells to move and change shapes, but also activate mechanosensitive pathways for gene expression change to alter cell behaviors [76-80].

Actin monomers are able to form crosslinked and/or branched actin networks in the cortex and lamellipodia, parallel actin filaments in the filopodia, and antiparallel contractile bundles in the stress fibers, by recruiting and binding to a variety of region-specific proteins including nucleation proteins such as Arp2/3 complex and formin, crosslinking proteins such as α-actinin and filamin, capping proteins and myosin proteins [81]. The primary microstructures of actin CSK that are intricately linked together in a whole cell to form the complex architecture of CSK network are associated with specific physical properties and functions.

For example, filopodia, the spike-like surface protrusion at the cell front are composed of bundled actin filaments with the fast growing end (*plus end* or *barbed end*) toward the filopodial tips, playing a role in sensing the cell microenvironment, initiating cell-ECM and cell-cell interaction, and transmitting signals [310-315]. The backside of filopodia is embedded in and connected to a quasi-two-dimensional actin mesh, the lamellipodium, where the actin filaments have consistent radial orientation to create retrograde flow and treadmilling that push forward the leading edge of motile cells [316, 317]. In contrast to lamellipodia, actin mesh at the cell cortex is contractile in the presence of myosin and is attached to the plasma membrane via linkage proteins [318, 319]. The cortical contraction results in an inward force on the cell membrane that tends to balance the osmotic pressure difference thus regulating cell shape changes and cell motility via mechanisms such as blebbing [318]. Excluded from the aforementioned regions but throughout the rest of the cell and dominant in less motile cells are stress fibers that have a

central role in cell adhesion and morphogenesis [123, 320, 321]. The structure of stress fibers is classified as: (1) transverse arcs that run parallel to the cell leading edge and behind the lamellipodia, nucleated from lamellipodia, crosslinked with myosin but not anchored with FAs; (2) dorsal stress fibers that extend from nascent FAs in the lamellipodia and insert into the transverse arcs, not contractile but mechanically link the transverse arcs and FAs to redistribute tension to cell-ECM interface; (3) ventral stress fibers that are thought to assemble through fusion of dorsal stress fibers and/or transverse arcs, enriched with myosin II and generate high contractile forces in the direction optimal for ECM sensing.

The connection and dynamic transition between different subcellular actin architectures create a mechanosensitive physical coupling that controls the physical properties of cells and play a central role in transmitting compressive and tensile forces and in sensing mechanical microenvironment. Therefore, unraveling the correlation between the actin cytoskeletal architecture and the mechanical properties of a cell can provide insights into where forces are acting or transmitted through the cytoskeleton network and broaden our understanding of force-dependent cellular processes such as durotaxis and epithelial-mesenchymal transition (EMT). The long-lived, highly active, and multi-architectural actin cytoskeleton likely functions as a cellular memory that integrates the past interactions with the mechanical microenvironments and influences future cell behaviors.

Therefore, detection and quantification of actin CSK and measurement of the transition between different actin architectures when cells are subjected to repeated mechanical stimuli could provide unique insights into the adaptive process of cell memory. Molecular manipulations interfering actin nucleation, branching, capping, and crosslinking can be applied

to tune the composition of different actin architectures. Together with theoretical modeling, key measures that might correlate with the mechanical properties of cells such as cell contraction and cell stiffness that change with the mechanical and biochemical microenvironment, may be extracted. It would be possible to reveal the regulatory roles of different actin architectures and CSK-associated proteins in mediating mechanical memory/adaptation and mechanical homeostasis.

Appendices

Appendix A

Fabrication and functionalization of unstretchable and stretchable micropost arrays

A.1 Fabrication of Si micropost mold

Conventional high-resolution photolithography and deep reactive ion-etching (DRIE) techniques were used for fabrication of Si micropost mold. A 5× reduction step-and-repeat projection stepper (Nikon NSR2005i9, Nikon Precision Inc., Belmont, CA) was used for photoresist patterning. DRIE was performed with an inductively coupled plasma deep reactive-ion etcher (ICP Deep Trench Etching Systems, Surface Technology Systems, Allentown, PA). Height of Si micropost was controlled by varying etching time during DRIE. After stripping photoresist with the Piranha solution (4:1 *v* / *v* H_2SO_4 / H_2O_2), dimensions of Si micropost were measured using surface profilometry (Prometrix P-10, KLA-Tenco, Milpitas, CA) and scanning electron microscopy (SEM; JEOL6320FV, JEOL USA, Peabody, MA). Si mold was activated by oxygen plasma for 2 min (Plasma Cleaner PDC-001, Harrick Plasma, Ithaca, NY), and was passivated with trichloro (1H, 1H, 2H, 2H-perfluorooctyl) silane (Sigma-Aldrich, St. Louis, MO)

for 4 hr under vacuum to aid subsequent release of negative PDMS templates from the Si mold. The Si mold used in this work contained hexagonally spaced posts with various post diameters, post heights, and post center-to-center distance. Finite element modeling was used to characterize the nominal spring constant K_{post} of PDMS microposts replicated from the Si molds[85] .

A.2 Fabrication of PDMS micropost array

The PDMS micropost array was generated by replica molding as previously described [258, 322-324]. Briefly, to make a negative template containing an array of holes, PDMS prepolymer with a 10:1 base to curing agent ratio was poured over the Si micropost mold and cured at 110°C for 20 min. The negative PDMS mold was peeled off from the Si micropost mold before oxidized with oxygen plasma and passivated with trichloro (1H, 1H, 2H, 2H-perfluorooctyl) silane vapor overnight under vacuum. In parallel, for the fabrication of stretchable micropost array, a coverslip was passivated with trichloro (1H, 1H, 2H, 2H-perfluorooctyl) silane vapor for 2 hr before spin-coated with a thin layer of PDMS prepolymer at 2000 rpm for 30 sec (Laurell Technologies, North Wales, PA). PDMS on the coverslip was cured at 110°C for 20 min to form a releasable thin PDMS layer. The final PDMS micropost array was generated by pouring PDMS prepolymer over the PDMS negative template, degassing under vacuum, flipping and placing a normal or the PDMS-coated coverslip in direct contact with the negative PDMS template, curing at 110°C for 40 hr, and peeling off the PDMS micropost array from the negative PDMS template. When peeling induced collapse of PDMS microposts, we recovered PDMS microposts by sonication in 100% ethanol for 30 sec followed

by dry-release with liquid CO_2 using a critical point dryer (Samdri®-PVT-3D, Tousimis, Rockville, MD).

A.3 Functionalization of PDMS micropost array

Functionalization of the PDMS micropost array was achieved using micro-contact printing. Briefly, flat, featureless PDMS stamps were generated and immersed in a solution containing both fibronectin (50 μg mL^{-1}; Sigma-Aldrich) and Alexa-Fluor 647 conjugated fibrinogen (25 μg mL^{-1}; Invitrogen, Carlsbad, CA) for 1 hr. PDMS stamps were rinsed with DI water before blown dry using nitrogen gas. Protein-coated PDMS stamps were then placed in conformal contact with the PDMS micropost array pre-treated with UV-ozone (UV-ozone cleaner, Jelight, Irvine, CA) to transfer adhesive proteins from stamps to the tops of PDMS microposts. To passivate side surfaces of micropost to avoid undesired cell adhesion, PDMS microposts were submerged sequentially in 100% ethanol (10 sec), 70% ethanol (10 sec), 30% ethanol (10 sec), DI water (10 sec), and 0.2% *w*/*v* Pluronics® F-127 solution (Sigma-Aldrich; 1 hr), before rinsed three times with DI water. Functionalized PDMS micropost arrasys could be stored in phosphate-buffered saline (PBS; Invitrogen) solution for up to one week before use.

A.4 Integration of PDMS micropost array onto a stretchable PDMS basal membrane

Stretchable micropost array was generated by integrating the PDMS micropost array onto a stretchable PDMS basal membrane. To generate a PDMS basal membrane, PDMS prepolymer was spin-coated onto 100 mm petri dish covers at 500 rpm for 30 sec followed by curing at 70°C for 40 hr. The resultant PDMS basal membrane had a thickness of 200 – 300 μm. In parallel, prior to the surface passivation, the thin PDMS layer holding the PDMS micropost array was gently peeled off from the coverslip, flipped, and brought into conformal contact with a PDMS pad before the backside of the PDMS layer was treated with air plasma. The thin PDMS layer holding the PDMS micropost array was then bonded to the PDMS basal membrane *via* plasma-assisted PDMS-PDMS bonding to generate the final stretchable micropost array, followed by surface passivation as descried in **Appendix A.3**.

Appendix B

Traction force measurement

A MATLAB program was developed to measure cellular and subcellular traction forces applied by the cells cultured on the micropost arrays. Code and full instructions are available upon request. A lite step-by-step instruction is as follows.

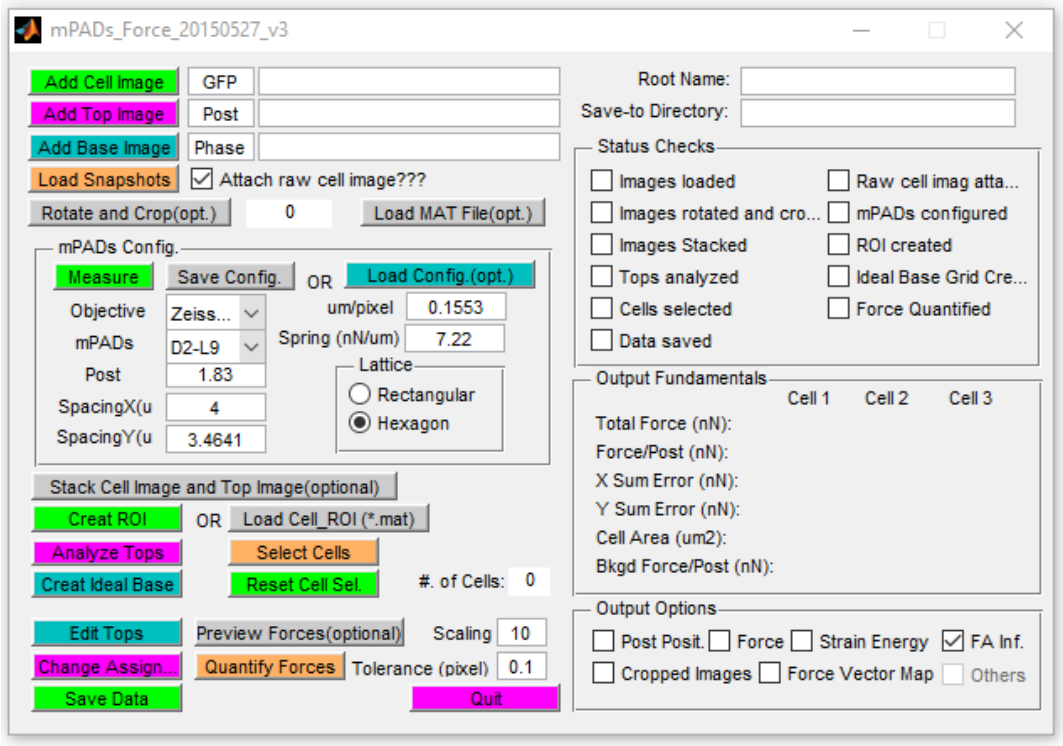

Figure B-1 Graphic user interface of the MATLAB code for traction force measurement.

- *Starting the program*

Step 1: Open MATLAB software, change the current directory to the folder containing the whole package, open the latest file named "mPADs_Force_20131018.m" for example, and run (F5) the script. The user interface as shown in **Figure B-1** pops up.

- *Loading images*

Step 2: Edit the channel names for Cell Image, Top Image, and Base Image ("Pax", "Post", and "Phase" in the demo).

Use the channel names defined in the microscope software, which are the last several letters before the extension of the image files.

Step 3: Click <Add Cell Image>, <Add Top Image>, and <Add Base Image> to select the images to load.

Top image is required for the force measurement. Cell image is needed if you want to measure the fluorescence intensity of FAs for example on each post. Base image is a reference for the post base positions and is only used to correct the image stack. After selecting the cell image, the program will automatically find the top image and base image by searching the predefined channel names. If the files cannot be found automatically, windows will pop up for manual selection. You can also click <Add Top Image> and <Add Base Image> to select the images accordingly. If you only need to measure cell contraction, you can use top image for the three channels.

Step 4: Click <Load Snapshots> to load all images.

- *Pre-processing images*

Step 5: Click <Rotate and Crop(opt.)>.

Click on any two points in the image and the image will be rotated such that the two points are in a horizontal line. Two posts in the close-packed direction of the microposts are recommended, but not necessary. Three green dashed lines appear in the window as horizontal reference. Press *left* or *right* arrow on the keyboard to make fine adjustment. Press *Enter* when done.

To crop/trim the image, draw a rectangle in the window by click and dragging the mouse, to completely enclose the cells. Double click inside the rectangle to close the window and return to the user interface.

- *Micropost array configuration*

Step 6: Select *Objective Mag.* and *mPADs Geo.* in the popup menus, and *um/pixel* and *Spring (nN/um)* are changed accordingly. You can also select *others* in *Objective Mag.* and *mPADs Geo.* popup menus, and manually input *um/pixel* and *Spring (nN/um)* if they are not in the list.

Step 7: Enter the post diameter.

Step 8: Select the *Lattice* pattern (*Hexagon* is default), and enter the designed post spacing in *x* and *y* direction in *SpacingX(um)* and *SpacingY(um)*.

Step 9: Click <Measure> to measure the actual spacing in the *x* and *y* direction.

Measure Horizontal: select the center of two distal posts in the same row (not necessary to be horizontal, but must in the close packed direction if the pattern is hexagonal). A row of blue boxes appears based on your post selections (**Figure B-2**, *left*). Make sure the boxes each

enclose one post, and there is no overlap between boxes and posts. Click <Yes> to continue, and <No> to retry.

Measure Vertical: select the center of two distal posts in the same column (perpendicular to the "horizontal" direction). Make sure that every other boxes enclose one post (**Figure B-2**, *right*).

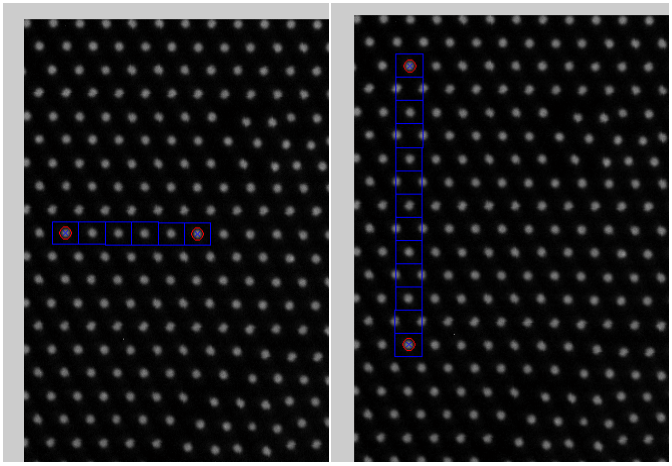

Figure B-2 Configuration of micropost arrays. Demo showing the measurement of post spacing the *x* (*left*) and *y* (*right*) direction.

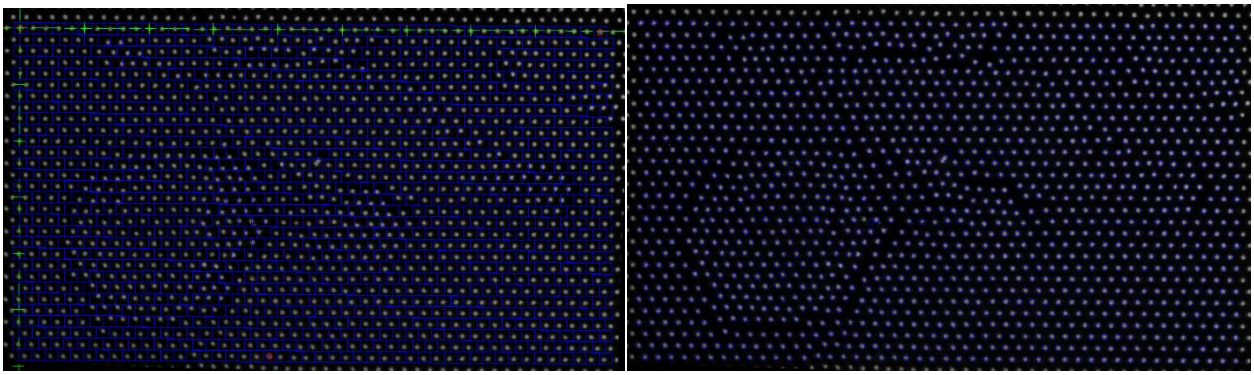

Figure B-3 Post top position analysis. (*left*) Creation of the region of interest (ROI) by selecting the posts (*red* circles)in the upper left corner, upper right corner, and one on the bottom row. The grid of blue boxes each enclosing one post shows the ROI. (*right*) Detection of the micropost tops. Once the analysis is complete, all posts in the ROI are circled in *blue*.

- *Analyzing post positions*

Step 10: Click <Create ROI> and click in the window showing the top image the centers of top left post, top right post, and the one on the bottom row in your region of interest.

After selecting the post on the bottom row in ROI, a grid of blue boxes appears with every post in ROI assigned to one box (**Figure B-3**, *left*). Click <Yes> to continue and <No> to redo it.

Step 11: Click <Analyze Tops> and a waiting bar pops up showing the processing of analyzing post tops. Once it is finished, top image is opened and all posts in the ROI are circled in blue (**Figure B-3**, *right*). Press Enter to close it.

Step 12: Click <Create Ideal Base>, and both Cell Image and Top Image are opened. On the Top Image, select as many free posts as possible (**Figure B-4**, *left*). Left click to select one post, middle click to select a cluster of them, and right click to unselect it. Click out of the blue grid when done. By doing the least squares fitting, the ideal base position is calculated and marked with *red* circles (**Figure B-4**, *right*). Click <Yes> to continue and <No> to redo it.

- *Selecting cells and assigning posts*

Step 13: Click <Select Cells> to open Cell Image and Top Image with force vector maps. On the Cell Image, draw polygon around a cell, and double click inside when done. Repeat to select more cells if necessary. Overlap is allowed but not recommended.

Step 14: Click <Change Assigned Post> to modify the post assignment. Posts in different cells are boxed in green, cyan, and red (**Figure B-5**, *left*). Unassigned posts are boxed in blue. Click inside a cell to activate the modification mode. Selected cell is highlighted in yellow.

Left click to assign a post to the cell and the box enclosing the post is turned into magenta; right click to un-assign a post and the box into blue. Click out of the blue ROI array when the post assignment to a cell is done. Repeat it to edit post assignment of any cell if necessary. Click out of the blue box array when post assignment of all cells is done.

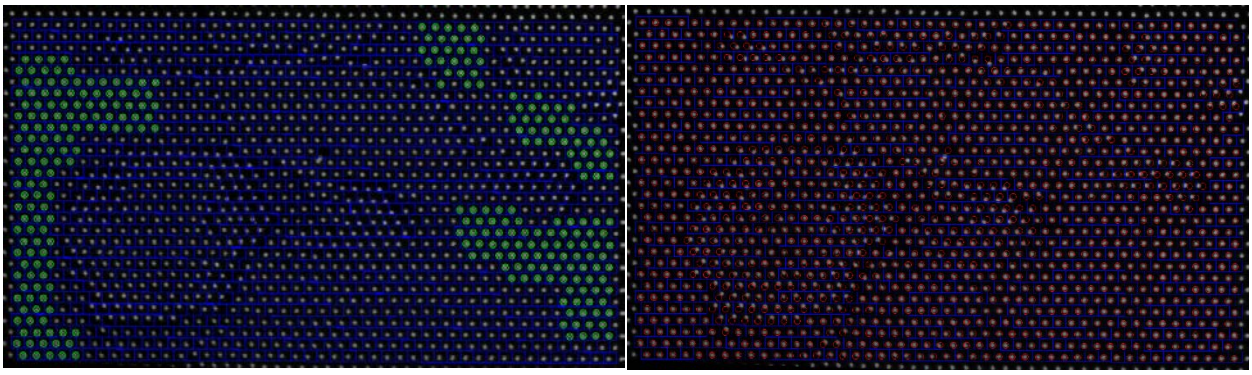

Figure B-4 Post base position estimation. (*left*) Selection of the free standing posts which are marked with *green* circles. (*right*) Grid of the ideal positions of the post bases (*red*) generated from the free standing posts.

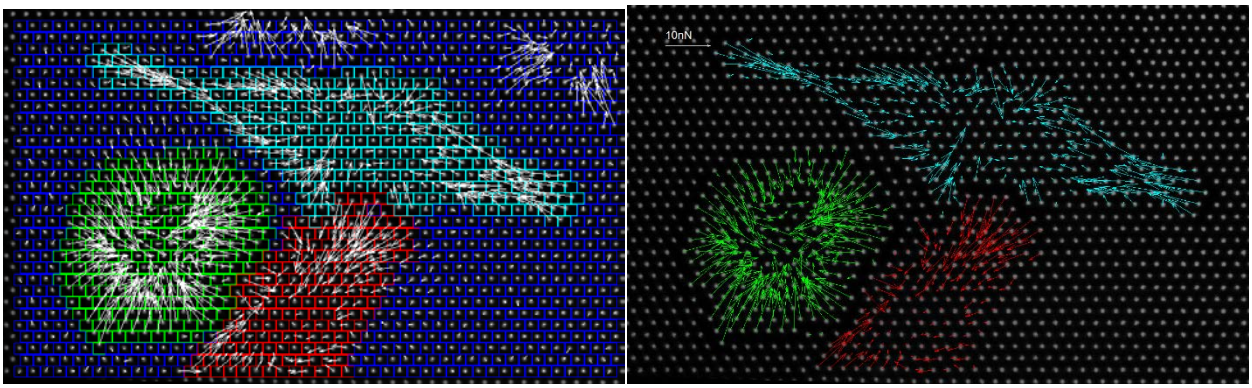

Figure B-5 Post assignment and cell contractility measurement. (*left*) Demo showing that posts underneath different cells were assigned with different colors. (*right*) Representative force vector maps showing the cell contractility.

- *Adjusting post positions*

Step 15: Click <Edit Tops> to manually correct the position of post tops. Posts assigned to different cells are circled in green, cyan, and red. Click inside a blue box that is assigned to the post with incorrect detected position, and a zoom image appears with the box highlighted in yellow and the automatically detected tops in magenta. Click at the center of the post, and use arrow key to make any find adjustments. Press Enter when done. Repeat it to correct any post you want, or click out of the blue box array to continue.

Step 16: Edit the scaling parameter, and click <Preview Forces> to preview the force vector map of all cells on the Top Images (**Figure B-5**, *right*).

- *Quantify Forces*

Step 17: Click <Quantify Force> to quantify the force. The basic information will be refreshed in the panel of *Output Fundamentals*. If variables such as the spring constant, um/pixel, and post assignment that determine the force are changed, you must click <Quantify Force> to update the results before saving the data.

- *Save Data*

Click <Save Data> to save the results. If no item in the *Output Options* is checked, one *.mat file containing all data and one *.xls file containing the output basics will be created in the folder indicated by the *Save-to Directory*. Their file names are the *Root Name*. Both *Root Name* and *Save-to Directory* are editable.

In the panel of Output Options, check *Post Posit.*, *Force*, *Strain Energy*, or *FA inform.* to output the results on individual posts to the *.xls file. Check Cropped Images to save the image

(*.tif) after pre-processing, and check Force Vector Map to save the force vector map with the background of the post top image(*.tif, *.eps, and *.tif).

Appendix C

Model parameters

Table C.1 Model parameters for the study of cellular homeostasis and subcellular rheostasis

Sym.	Definition	*U*	*N*	*B*	*J*	*C*	*T*
N_{FA}	FA size	OUT	-	-	-	-	-
$k_{FA,o}$	Reference rate for FA association and dissociation (s^{-1})	1	-	-	-	-	-
N_{FA}^{tot}	Total number of FA unit available in the cytosol	450	-	-	-	-	-
γ_{FA}	Non-dimensional association rate for FA	1	-	-	-	-	-
f_{FA}^{*}	Force scale for non-dimensionalization (pN)	5.38 [265]	18.83	9.68	6.46	10.76	4.60 [265]
$\phi_{FA,s}$	See Equ. (4.3)	7.78 [265]	-	-	6.61	-	7.65 [265]
$\phi_{FA,c}$	See Equ. (4.3)	4.02 [265]	1.81	2.41	-	1.73	0 [265]
N_{ACT}	Actin subunits in stress fiber	OUT	-	-	-	-	-
$k_{ACT,o}$	Reference rate for actin association and dissociation	1	-	-	-	-	-
N_{ACT}^{tot}	Total number of actin subunit available in the cytosol	9000	-	-	-	-	-
γ_{ACT}	Non-dimensional association rate for actin	1	2	-	1.8	0.6	-
f_{ACT}^{*}	Force scale for non-dimensionalization (pN)	10.68 [283]	-	-	-	-	-
$\phi_{ACT,s}$	See Equ. (4.4)	2.42 [283]	-	-	-	-	-
$\phi_{ACT,c}$	See Equ. (4.4)	1.43 [283]	-	-	-	-	-
F_{tot}	Total force on FA cluster and actin stress fiber	OUT	-	-	-	-	-

Continue on next page

Sym.	Definition	*U*	*N*	*B*	*J*	*C*	*T*
K_{post}	Spring constant of micropost (pN/μm)	7200 [324]	-	-	-	-	-
K_{SF}	Spring constant of actin stress fiber (pN/μm)	157 [292, 293]	-	-	-	-	-
L	Length of spring-CE system; stretch profile	INP	-	-	-	-	-
v_o	Equivalent unloaded sliding velocity of myosin (μm/s)	0.012 [295]	0.015	0.0072	-	-	-
f_{stall}	Stall force of myosin (pN)	2 [294]	-	-	-	-	-
c	Ratio of myosin number to actin subunit number	0.469	-	-	-	-	-

Note: *U*: untreated; *N*: nocodazole treatment; *B*: blebbistatin treatment; *J*: jasplakinolide treatment; *C*: cytochalasin D treatment; *T*: TS2/16 antibody treatment; INP: input of the model; OUT: output of the model; -: same as untreated control. If references were not listed, then model parameters were determined by fitting ground-state values of cytoskeleton (CSK) tension and focal adhesion (FA) size for REF-52 fibroblasts under conditions as specified.

References

1. Hudspeth, A.J., *How the ear's works work.* Nature, 1989. **341**(6241): p. 397-404.
2. Wang, N., J.P. Butler, and D.E. Ingber, *Mechanotransduction across the cell surface and through the cytoskeleton.* Science, 1993. **260**(5111): p. 1124-7.
3. Osol, G., *Mechanotransduction by vascular smooth muscle.* J Vasc Res, 1995. **32**(5): p. 275-92.
4. Davies, P.F., *Flow-mediated endothelial mechanotransduction.* Physiol Rev, 1995. **75**(3): p. 519-60.
5. Discher, D.E., P. Janmey, and Y.L. Wang, *Tissue cells feel and respond to the stiffness of their substrate.* Science, 2005. **310**: p. 1139-1143.
6. Vogel, V. and M. Sheetz, *Local force and geometry sensing regulate cell functions.* Nature Reviews Molecular Cell Biology, 2006. **7**(4): p. 265-275.
7. Engler, A.J., et al., *Matrix Elasticity Directs Stem Cell Lineage Specification.* Cell, 2006. **126**(4): p. 677-689.
8. Chen, C.S., *Mechanotransduction – a field pulling together?* Journal of Cell Science, 2008. **121**(20): p. 3285-3292.
9. Geiger, B., J.P. Spatz, and A.D. Bershadsky, *Environmental sensing through focal adhesions.* Nature Reviews Molecular Cell Biology, 2009. **10**(1): p. 21-33.
10. Humphrey, J.D., *Vascular Mechanics, Mechanobiology, and Remodeling.* J Mech Med Biol, 2009. **9**(2): p. 243-257.
11. Ando, J. and K. Yamamoto, *Vascular mechanobiology: endothelial cell responses to fluid shear stress.* Circ J, 2009. **73**(11): p. 1983-92.
12. Mammoto, T. and D.E. Ingber, *Mechanical control of tissue and organ development.* Development, 2010. **137**(9): p. 1407-1420.
13. Chien, S., *Mechanotransduction and endothelial cell homeostasis: the wisdom of the cell.* American Journal of Physiology - Heart and Circulatory Physiology, 2007. **292**(3): p. H1209-H1224.
14. Janmey, P.A. and C.A. McCulloch, *Cell Mechanics: Integrating Cell Responses to Mechanical Stimuli.* Annual Review of Biomedical Engineering, 2007. **9**(1): p. 1-34.
15. Mammoto, T., A. Mammoto, and D.E. Ingber, *Mechanobiology and Developmental Control.* Annual Review of Cell and Developmental Biology, 2013. **29**(1): p. 27-61.
16. Schoen, I., B.L. Pruitt, and V. Vogel, *The Yin-Yang of Rigidity Sensing: How Forces and Mechanical Properties Regulate the Cellular Response to Materials.* Annual Review of Materials Research, 2013. **43**(1): p. 589-618.
17. Sun, Y. and J. Fu, *Mechanobiology: a new frontier for human pluripotent stem cells.* Integr Biol (Camb), 2013. **5**(3): p. 450-7.
18. Ivanovska, I.L., et al., *Stem cell mechanobiology: diverse lessons from bone marrow.* Trends in Cell Biology, 2015. **25**(9): p. 523-532.

19. Paluch, E.K., et al., *Mechanotransduction: use the force(s).* BMC Biology, 2015. **13**: p. 47.
20. Kutys, M.L. and C.S. Chen, *Forces and mechanotransduction in 3D vascular biology.* Current Opinion in Cell Biology, 2016. **42**: p. 73-79.
21. Haack, T. and S. Abdelilah-Seyfried, *The force within: endocardial development, mechanotransduction and signalling during cardiac morphogenesis.* Development, 2016. **143**(3): p. 373-386.
22. Heisenberg, C.P. and Y. Bellaiche, *Forces in tissue morphogenesis and patterning.* Cell, 2013. **153**(5): p. 948-62.
23. Wolf, C.B. and M.R.K. Mofrad, *Mechanotransduction and Its Role in Stem Cell Biology.* Trends in Stem Cell Biology and Technology, H. Baharvand, Editor. 2009, Humana Press. p. 389-403.
24. Kieserman, E.K., M. Glotzer, and J.B. Wallingford, *Developmental regulation of central spindle assembly and cytokinesis during vertebrate embryogenesis.* Curr Biol, 2008. **18**(2): p. 116-23.
25. Fink, J., et al., *External forces control mitotic spindle positioning.* Nat Cell Biol, 2011. **13**(7): p. 771-8.
26. Lancaster, O.M. and B. Baum, *Might makes right: Using force to align the mitotic spindle.* Nat Cell Biol, 2011. **13**(7): p. 736-8.
27. Garzon-Coral, C., H.A. Fantana, and J. Howard, *A force-generating machinery maintains the spindle at the cell center during mitosis.* Science, 2016. **352**(6289): p. 1124-7.
28. Nishioka, N., et al., *The Hippo Signaling Pathway Components Lats and Yap Pattern Tead4 Activity to Distinguish Mouse Trophectoderm from Inner Cell Mass.* Developmental Cell, 2009. **16**(3): p. 398-410.
29. Nishioka, N., et al., *Tead4 is required for specification of trophectoderm in pre-implantation mouse embryos.* Mechanisms of Development, 2008. **125**(3–4): p. 270-283.
30. Krupinski, P., V. Chickarmane, and C. Peterson, *Simulating the Mammalian Blastocyst - Molecular and Mechanical Interactions Pattern the Embryo.* PLoS Computational Biology, 2011. **7**(5): p. e1001128.
31. Martin, A.C. and B. Goldstein, *Apical constriction: themes and variations on a cellular mechanism driving morphogenesis.* Development, 2014. **141**(10): p. 1987-1998.
32. Sawyer, J.M., et al., *Apical constriction: A cell shape change that can drive morphogenesis.* Developmental Biology, 2010. **341**(1): p. 5-19.
33. He, B., et al., *Apical constriction drives tissue-scale hydrodynamic flow to mediate cell elongation.* Nature, 2014. **508**(7496): p. 392-396.
34. Martin, A.C., M. Kaschube, and E.F. Wieschaus, *Pulsed contractions of an actin-myosin network drive apical constriction.* Nature, 2009. **457**(7228): p. 495-499.
35. Wang, H.Q., et al., *Shear stress protects against endothelial regulation of vascular smooth muscle cell migration in a coculture system.* Endothelium, 2006. **13**(3): p. 171-80.
36. Ye, C., et al., *Shear stress and vascular smooth muscle cells promote endothelial differentiation of endothelial progenitor cells via activation of Akt.* Clin Biomech (Bristol, Avon), 2008. **23 Suppl 1**: p. S118-24.
37. Chiu, J.J., S. Usami, and S. Chien, *Vascular endothelial responses to altered shear stress: pathologic implications for atherosclerosis.* Ann Med, 2009. **41**(1): p. 19-28.

38. Nigro, P., J. Abe, and B.C. Berk, *Flow shear stress and atherosclerosis: a matter of site specificity.* Antioxid Redox Signal, 2011. **15**(5): p. 1405-14.
39. Lu, D. and G.S. Kassab, *Role of shear stress and stretch in vascular mechanobiology.* J R Soc Interface, 2011. **8**(63): p. 1379-85.
40. Zhang, C., et al., *Blood flow and stem cells in vascular disease.* Cardiovasc Res, 2013. **99**(2): p. 251-9.
41. Chatzizisis, Y.S., et al., *Role of endothelial shear stress in the natural history of coronary atherosclerosis and vascular remodeling: molecular, cellular, and vascular behavior.* J Am Coll Cardiol, 2007. **49**(25): p. 2379-93.
42. Mehdizadeh, A. and A. Norouzpour, *New insights in atherosclerosis: endothelial shear stress as promoter rather than initiator.* Med Hypotheses, 2009. **73**(6): p. 989-93.
43. Lacolley, P., et al., *The vascular smooth muscle cell in arterial pathology: a cell that can take on multiple roles*. Vol. 95. 2012. 194-204.
44. Nykanen, A.I., et al., *Combined vascular endothelial growth factor and platelet-derived growth factor inhibition in rat cardiac allografts: beneficial effects on inflammation and smooth muscle cell proliferation.* Transplantation, 2005. **79**(2): p. 182-9.
45. Koller, A., *Signaling pathways of mechanotransduction in arteriolar endothelium and smooth muscle cells in hypertension.* Microcirculation, 2002. **9**(4): p. 277-94.
46. Sukhovershin, R.A., G. Yepuri, and Y.T. Ghebremariam, *Endothelium-Derived Nitric Oxide as an Antiatherogenic Mechanism: Implications for Therapy.* Methodist DeBakey Cardiovascular Journal, 2015. **11**(3): p. 166-171.
47. Taguchi, E., et al., *Impact of shear stress and atherosclerosis on entrance-tear formation in patients with acute aortic syndromes.* Heart Vessels, 2014. **29**(1): p. 78-82.
48. Heo, K.S., K. Fujiwara, and J. Abe, *Shear stress and atherosclerosis.* Mol Cells, 2014. **37**(6): p. 435-40.
49. Schaefer, A. and P.L. Hordijk, *Cell-stiffness-induced mechanosignaling – a key driver of leukocyte transendothelial migration.* Journal of Cell Science, 2015. **128**(13): p. 2221-2230.
50. Shkumatov, A., et al., *Matrix stiffness-modulated proliferation and secretory function of the airway smooth muscle cells.* Am J Physiol Lung Cell Mol Physiol, 2015. **308**(11): p. L1125-35.
51. Peyton, S.R., et al., *The effects of matrix stiffness and RhoA on the phenotypic plasticity of smooth muscle cells in a 3-D biosynthetic hydrogel system.* Biomaterials, 2008. **29**(17): p. 2597-607.
52. Brown, X.Q., et al., *Effect of substrate stiffness and PDGF on the behavior of vascular smooth muscle cells: implications for atherosclerosis.* J Cell Physiol, 2010. **225**(1): p. 115-22.
53. Schulz, R.M. and A. Bader, *Cartilage tissue engineering and bioreactor systems for the cultivation and stimulation of chondrocytes.* European Biophysics Journal, 2007. **36**(4): p. 539-568.
54. Royce, S.G., Y. Moodley, and C.S. Samuel, *Novel therapeutic strategies for lung disorders associated with airway remodelling and fibrosis.* Pharmacology & Therapeutics, 2014. **141**(3): p. 250-260.

55. Shao, Y. and J. Fu, *Integrated micro/nanoengineered functional biomaterials for cell mechanics and mechanobiology: a materials perspective.* Adv Mater, 2014. **26**(10): p. 1494-533.
56. Gui, L. and L.E. Niklason, *Vascular Tissue Engineering: Building Perfusable Vasculature for Implantation.* Curr Opin Chem Eng, 2014. **3**: p. 68-74.
57. Sachs, F., *Stretch-activated ion channels: what are they?* Physiology (Bethesda), 2010. **25**(1): p. 50-6.
58. Delmas, P. and B. Coste, *Mechano-gated ion channels in sensory systems.* Cell, 2013. **155**(2): p. 278-84.
59. Ranade, S.S., R. Syeda, and A. Patapoutian, *Mechanically Activated Ion Channels.* Neuron, 2015. **87**(6): p. 1162-79.
60. Volkers, L., Y. Mechioukhi, and B. Coste, *Piezo channels: from structure to function.* Pflugers Arch, 2015. **467**(1): p. 95-9.
61. Wu, J., A.H. Lewis, and J. Grandl, *Touch, Tension, and Transduction - The Function and Regulation of Piezo Ion Channels.* Trends Biochem Sci, 2016.
62. Campbell, I.D. and M.J. Humphries, *Integrin structure, activation, and interactions.* Cold Spring Harb Perspect Biol, 2011. **3**(3).
63. Choquet, D., D. Felsenfeld, and M. Sheetz, *Extracellular matrix rigidity causes strengthening of integrin-cytoskeleton linkages.* Cell, 1997. **88**(1): p. 39-48.
64. Li, Z., H. Lee, and C. Zhu, *Molecular mechanisms of mechanotransduction in integrin-mediated cell-matrix adhesion.* Experimental Cell Research.
65. Roca-Cusachs, P., T. Iskratsch, and M.P. Sheetz, *Finding the weakest link - exploring integrin-mediated mechanical molecular pathways.* J Cell Sci, 2012. **125**(Pt 13): p. 3025-38.
66. Goldmann, W.H., *Mechanotransduction and focal adhesions.* Cell Biol Int, 2012. **36**(7): p. 649-52.
67. Ross, T.D., et al., *Integrins in mechanotransduction.* Current Opinion in Cell Biology, 2013. **25**(5): p. 613-618.
68. Leckband, D.E. and J. de Rooij, *Cadherin adhesion and mechanotransduction.* Annu Rev Cell Dev Biol, 2014. **30**: p. 291-315.
69. Dorland, Y.L. and S. Huveneers, *Cell–cell junctional mechanotransduction in endothelial remodeling.* Cellular and Molecular Life Sciences, 2016: p. 1-14.
70. Wang, N., J.D. Tytell, and D.E. Ingber, *Mechanotransduction at a distance: mechanically coupling the extracellular matrix with the nucleus.* Nat Rev Mol Cell Biol, 2009. **10**(1): p. 75-82.
71. Kaminski, A., G.R. Fedorchak, and J. Lammerding, *The cellular mastermind(?) – Mechanotransduction and the nucleus.* Progress in molecular biology and translational science, 2014. **126**: p. 157-203.
72. Belaadi, N., J. Aureille, and C. Guilluy, *Under Pressure: Mechanical Stress Management in the Nucleus.* Cells, 2016. **5**(2): p. 27.
73. Navarro, A.P., M.A. Collins, and E.S. Folker, *The nucleus is a conserved mechanosensation and mechanoresponse organelle.* Cytoskeleton, 2016. **73**(2): p. 59-67.
74. Mui, K.L., C.S. Chen, and R.K. Assoian, *The mechanical regulation of integrin–cadherin crosstalk organizes cells, signaling and forces.* Journal of Cell Science, 2016. **129**(6): p. 1093-1100.

75. Weber, G.F., M.A. Bjerke, and D.W. DeSimone, *Integrins and cadherins join forces to form adhesive networks.* Journal of Cell Science, 2011. **124**(8): p. 1183-1193.
76. Papusheva, E. and C.P. Heisenberg, *Spatial organization of adhesion: force-dependent regulation and function in tissue morphogenesis.* EMBO J, 2010. **29**(16): p. 2753-68.
77. Murrell, M., et al., *Forcing cells into shape: the mechanics of actomyosin contractility.* Nat Rev Mol Cell Biol, 2015. **16**(8): p. 486-498.
78. Anon, E., et al., *Cell crawling mediates collective cell migration to close undamaged epithelial gaps.* Proceedings of the National Academy of Sciences, 2012.
79. Das, T., et al., *A molecular mechanotransduction pathway regulates collective migration of epithelial cells.* Nat Cell Biol, 2015. **17**(3): p. 276-287.
80. DuFort, C.C., M.J. Paszek, and V.M. Weaver, *Balancing forces: architectural control of mechanotransduction.* Nat Rev Mol Cell Biol, 2011. **12**(5): p. 308-319.
81. Blanchoin, L., et al., *Actin dynamics, architecture, and mechanics in cell motility.* Physiol Rev, 2014. **94**(1): p. 235-63.
82. Murrell, M.P. and M.L. Gardel, *F-actin buckling coordinates contractility and severing in a biomimetic actomyosin cortex.* Proc Natl Acad Sci U S A, 2012. **109**(51): p. 20820-5.
83. Deriu, M.A., et al., *Biomechanics of actin filaments: a computational multi-level study.* J Biomech, 2011. **44**(4): p. 630-6.
84. Chaudhuri, O., S.H. Parekh, and D.A. Fletcher, *Reversible stress softening of actin networks.* Nature, 2007. **445**(7125): p. 295-8.
85. Weng, S. and J. Fu, *Synergistic regulation of cell function by matrix rigidity and adhesive pattern.* Biomaterials, 2011. **32**(36): p. 9584-9593.
86. Mann, J.M., et al., *A silicone-based stretchable micropost array membrane for monitoring live-cell subcellular cytoskeletal response.* Lab on a Chip, 2012. **12**(4): p. 731-740.
87. Lam, R., et al., *Live-cell subcellular measurement of cell stiffness using a microengineered stretchable micropost array membrane.* Integrative biology : quantitative biosciences from nano to macro, 2012. **4**(10): p. 1289-1298.
88. Weng, S., et al., *Mechanosensitive subcellular rheostasis drives emergent single-cell mechanical homeostasis.* Nat Mater, 2016. **advance online publication**.
89. Shao, Y., S. Weng, and J. Fu, *Stretchable micropost array cytometry: a powerful tool for cell mechanics and mechanobiology research,* in *Integrative Mechanobiology: Micro- and Nano- Techniques in Cell Mechanobiology*, Y. Sun, D.-H. Kim, and C.A. Simmons, Editors. 2015, Cambridge University Press. p. 32-46.
90. Agrawal, R., et al., *Assessment of red blood cell deformability in type 2 diabetes mellitus and diabetic retinopathy by dual optical tweezers stretching technique.* Sci Rep, 2016. **6**: p. 15873.
91. Bornschlogl, T., et al., *Filopodial retraction force is generated by cortical actin dynamics and controlled by reversible tethering at the tip.* Proc Natl Acad Sci U S A, 2013. **110**(47): p. 18928-33.
92. Honarmandi, P., et al., *A microfluidic system with optical laser tweezers to study mechanotransduction and focal adhesion recruitment.* Lab Chip, 2011. **11**(4): p. 684-94.
93. Baumgartner, W., et al., *Cadherin interaction probed by atomic force microscopy.* Proc Natl Acad Sci U S A, 2000. **97**(8): p. 4005-10.

94. Matzke, R., K. Jacobson, and M. Radmacher, *Direct, high-resolution measurement of furrow stiffening during division of adherent cells.* Nat Cell Biol, 2001. **3**(6): p. 607-10.
95. Lee, L.M., et al., *Development of an advanced microfluidic micropipette aspiration device for single cell mechanics studies.* Biomicrofluidics, 2016. **10**(5): p. 054105.
96. Webster, K.D., W.P. Ng, and D.A. Fletcher, *Tensional homeostasis in single fibroblasts.* Biophys J, 2014. **107**(1): p. 146-55.
97. Krishnan, R., et al., *Reinforcement versus fluidization in cytoskeletal mechanoresponsiveness.* PLoS One, 2009. **4**(5): p. e5486.
98. Humphrey, J.D., E.R. Dufresne, and M.A. Schwartz, *Mechanotransduction and extracellular matrix homeostasis.* Nat Rev Mol Cell Biol, 2014. **15**(12): p. 802-12.
99. Muhamed, I., et al., *E-cadherin-mediated force transduction signals regulate global cell mechanics.* J Cell Sci, 2016. **129**(9): p. 1843-54.
100. Connelly, J.T., et al., *Actin and serum response factor transduce physical cues from the microenvironment to regulate epidermal stem cell fate decisions.* Nature Cell Biology, 2010. **12**(7): p. 711-U177.
101. McBeath, R., et al., *Cell shape, cytoskeletal tension, and RhoA regulate stem cell lineage commitment.* Developmental Cell, 2004. **6**: p. 483-495.
102. Chen, C.S., et al., *Geometric control of cell life and death.* Science, 1997. **276**: p. 1425-1428.
103. Huebsch, N., et al., *Harnessing traction-mediated manipulation of the cell/matrix interface to control stem-cell fate.* Nature Materials, 2010. **9**(6): p. 518-526.
104. Gilbert, P.M., et al., *Substrate elasticity regulates skeletal muscle stem cell self-renewal in culture.* Science, 2010. **329**: p. 1078-1081.
105. Mammoto, A., et al., *A mechanosensitive transcriptional mechanism that controls angiogenesis.* Nature, 2009. **457**(7233): p. 1103-1108.
106. Levental, K.R., et al., *Matrix crosslinking forces tumor progression by enhancing integrin signaling.* Cell, 2009. **139**(5): p. 891-906.
107. Isenberg, B.C., et al., *Vascular smooth muscle cell durotaxis depends on substrate stiffness gradient strength.* Biophysical Journal, 2009. **97**(5): p. 1313-1322.
108. Engler, A.J., et al., *Matrix elasticity directs stem cell lineage specification.* Cell, 2006. **126**: p. 677-689.
109. Paszek, M.J., et al., *Tensional homeostasis and the malignant phenotype.* Cancer Cell, 2005. **8**(3): p. 241-254.
110. Dalby, M.J., et al., *The control of human mesenchymal cell differentiation using nanoscale symmetry and disorder.* Nature Materials, 2007. **6**(12): p. 997-1003.
111. Yim, E.K., et al., *Nanopattern-induced changes in morphology and motility of smooth muscle cells.* Biomaterials, 2005. **26**(26): p. 5405-13.
112. Curtis, A. and C. Wilkinson, *Topographical control of cells.* Biomaterials, 1997. **18**(24): p. 1573-1583.
113. Conway, D.E. and M.A. Schwartz, *Mechanotransduction of shear stress occurs through changes in VE-cadherin and PECAM-1 tension: implications for cell migration.* Cell Adh Migr, 2015. **9**(5): p. 335-9.
114. Shav, D., et al., *Wall shear stress effects on endothelial-endothelial and endothelial-smooth muscle cell interactions in tissue engineered models of the vascular wall.* PLoS One, 2014. **9**(2): p. e88304.

115. Conway, D.E., et al., *Fluid shear stress on endothelial cells modulates mechanical tension across VE-cadherin and PECAM-1.* Curr Biol, 2013. **23**(11): p. 1024-30.
116. Sun, Y., et al., *MicroRNA 4323 induces human bladder smooth muscle cell proliferation under cyclic hydrodynamic pressure by activation of erk1/2 signaling pathway.* Exp Biol Med (Maywood), 2016.
117. Liu, Z., et al., *Mechanical tugging force regulates the size of cell–cell junctions.* Proceedings of the National Academy of Sciences, 2010. **107**(22): p. 9944-9949.
118. Shen, C., J. Fu, and C. Chen, *Patterning cell and tissue function.* Cellular and Molecular Bioengineering, 2008. **1**(1): p. 15-23.
119. Chen, C.S., *Mechanotransduction - a field pulling together?* Journal of Cell Science, 2008. **121**(20): p. 3285-3292.
120. Peyton, S., et al., *The emergence of ECM mechanics and cytoskeletal tension as important regulators of cell function.* Cell Biochemistry and Biophysics, 2007. **47**(2): p. 300-320.
121. Hoffman, B.D., C. Grashoff, and M.A. Schwartz, *Dynamic molecular processes mediate cellular mechanotransduction.* Nature, 2011. **475**(7356): p. 316-323.
122. Kim, D.H., et al., *Microengineered platforms for cell mechanobiology.* Annu Rev Biomed Eng, 2009. **11**: p. 203-33.
123. Kassianidou, E. and S. Kumar, *A biomechanical perspective on stress fiber structure and function.* Biochimica et Biophysica Acta (BBA) - Molecular Cell Research, 2015. **1853**(11, Part B): p. 3065-3074.
124. LaCroix, A.S., K.E. Rothenberg, and B.D. Hoffman, *Molecular-Scale Tools for Studying Mechanotransduction.* Annual Review of Biomedical Engineering, 2015. **17**(1): p. 287-316.
125. Chen, W., et al., *Nanotopography Influences Adhesion, Spreading, and Self-Renewal of Human Embryonic Stem Cells.* ACS Nano, 2012. **6**(5): p. 4094-4103.
126. Myrna, K.E., et al., *Substratum topography modulates corneal fibroblast to myofibroblast transformation.* Invest Ophthalmol Vis Sci, 2012. **53**(2): p. 811-6.
127. Teo, B.K., et al., *Nanotopography modulates mechanotransduction of stem cells and induces differentiation through focal adhesion kinase.* ACS Nano, 2013. **7**(6): p. 4785-98.
128. Georges, P.C. and P.A. Janmey, *Cell type-specific response to growth on soft materials.* Journal of Applied Physiology, 2005. **98**(4): p. 1547-1553.
129. Wong, J.Y., J.B. Leach, and X.Q. Brown, *Balance of chemistry, topography, and mechanics at the cell-biomaterial interface: Issues and challenges for assessing the role of substrate mechanics on cell response.* Surface Science, 2004. **570**(1-2): p. 119-133.
130. Pelham, R.J. and Y.-l. Wang, *Cell locomotion and focal adhesions are regulated by substrate flexibility.* Proceedings of the National Academy of Sciences of the United States of America, 1997. **94**(25): p. 13661-13665.
131. Lo, C.-M., et al., *Cell movement is guided by the rigidity of the substrate.* Biophysical Journal, 2000. **79**(1): p. 144-152.
132. Mei, Y., et al., *Combinatorial development of biomaterials for clonal growth of human pluripotent stem cells.* Nature Materials, 2010. **9**(9): p. 768-778.
133. Keselowsky, B.G., D.M. Collard, and A.J. García, *Integrin binding specificity regulates biomaterial surface chemistry effects on cell differentiation.* Proceedings of the National Academy of Sciences of the United States of America, 2005. **102**(17): p. 5953-5957.

134. Houseman, B.T. and M. Mrksich, *The microenvironment of immobilized Arg-Gly-Asp peptides is an important determinant of cell adhesion.* Biomaterials, 2001. **22**(9): p. 943-955.
135. Lutolf, M.P. and J.A. Hubbell, *Synthetic biomaterials as instructive extracellular microenvironments for morphogenesis in tissue engineering.* Nature Biotechnology, 2005. **23**(1): p. 47-55.
136. Vunjak-Novakovic, G. and David T. Scadden, *Biomimetic platforms for human stem cell research.* Cell Stem Cell, 2011. **8**(3): p. 252-261.
137. Fu, J., et al., *Mechanical regulation of cell function using geometrically modulated elastomeric substrates.* Nature Methods, 2010. **7**: p. 733-736.
138. Saez, A., et al., *Is the mechanical activity of epithelial cells controlled by deformations or forces?* Biophysical Journal, 2005. **89**(6): p. L52-L54.
139. du Roure, O., *Force mapping in epithelial cell migration.* Proceedings of the National Academy of Sciences of the United States of America, 2005. **102**: p. 2390-2395.
140. Tan, J.L., et al., *Cells lying on a bed of microneedles: An approach to isolate mechanical force.* Proceedings of the National Academy of Sciences of the United States of America, 2003. **100**(4): p. 1484-1489.
141. Yang, M.T., et al., *Assaying stem cell mechanobiology on microfabricated elastomeric substrates with geometrically modulated rigidity.* Nature Protocols, 2011. **6**: p. 187-213.
142. Sun, Y., et al., *Mechanics regulates fate decisions of human embryonic stem cells.* PLoS One, 2012. **7**(5).
143. Sun, Y., et al., *Hippo/YAP-mediated rigidity-dependent motor neuron differentiation of human pluripotent stem cells.* Nat Mater, 2014. **13**(6): p. 599-604.
144. Ricart, B., et al., *Measuring traction forces of motile dendritic cells on micropost arrays.* Biophysical Journal, 2011. **101**(11): p. 2620-2628.
145. Lam, R., et al., *Elastomeric microposts integrated into microfluidics for flow-mediated endothelial mechanotransduction analysis.* Lab on a Chip, 2012. **12**(10): p. 1865-1873.
146. Lin, Y.C., et al., *Probing cellular traction forces with magnetic nanowires and microfabricated force sensor arrays.* Nanotechnology, 2012. **23**(7): p. 075101.
147. Sniadecki, N.J., et al., *Magnetic microposts as an approach to apply forces to living cells.* Proc Natl Acad Sci U S A, 2007. **104**(37): p. 14553-8.
148. Tanase, M., N. Biais, and M. Sheetz, *Magnetic tweezers in cell biology.* Methods in cell biology, 2007. **83**: p. 473-493.
149. Chiou, P.Y., A.T. Ohta, and M.C. Wu, *Massively parallel manipulation of single cells and microparticles using optical images.* Nature, 2005. **436**(7049): p. 370-372.
150. Chen, D., et al., *Two-bubble acoustic tweezing cytometry for biomechanical probing and stimulation of cells.* Biophys J, 2015. **108**(1): p. 32-42.
151. Fan, Z., et al., *Acoustic tweezing cytometry for live-cell subcellular modulation of intracellular cytoskeleton contractility.* Sci Rep, 2013. **3**: p. 2176.
152. Webster, Kevin D., Win P. Ng, and Daniel A. Fletcher, *Tensional Homeostasis in Single Fibroblasts.* Biophysical Journal, 2014. **107**(1): p. 146-155.
153. Kamble, H., et al., *Cell stretching devices as research tools: engineering and biological considerations.* Lab Chip, 2016. **16**(17): p. 3193-203.
154. Tremblay, D., et al., *A novel stretching platform for applications in cell and tissue mechanobiology.* J Vis Exp, 2014(88).

155. Shao, Y., et al., *Uniaxial cell stretching device for live-cell imaging of mechanosensitive cellular functions.* Rev Sci Instrum, 2013. **84**(11): p. 114304.
156. Albinsson, S., I. Nordstrom, and P. Hellstrand, *Stretch of the vascular wall induces smooth muscle differentiation by promoting actin polymerization.* J Biol Chem, 2004. **279**(33): p. 34849-55.
157. Birukov, K.G., et al., *Stretch affects phenotype and proliferation of vascular smooth muscle cells.* Mol Cell Biochem, 1995. **144**(2): p. 131-9.
158. Lux, M., et al., *In vitro maturation of large-scale cardiac patches based on a perfusable starter matrix by cyclic mechanical stimulation.* Acta Biomater, 2016. **30**: p. 177-87.
159. Mihic, A., et al., *The effect of cyclic stretch on maturation and 3D tissue formation of human embryonic stem cell-derived cardiomyocytes.* Biomaterials, 2014. **35**(9): p. 2798-808.
160. Huang, Y., et al., *Effect of cyclic strain on cardiomyogenic differentiation of rat bone marrow derived mesenchymal stem cells.* PLoS One, 2012. **7**(4): p. e34960.
161. Lehoux, S. and E.A. Jones, *Shear stress, arterial identity and atherosclerosis.* Thromb Haemost, 2016. **115**(3): p. 467-73.
162. Cunningham, K.S. and A.I. Gotlieb, *The role of shear stress in the pathogenesis of atherosclerosis.* Lab Invest, 2005. **85**(1): p. 9-23.
163. Chiu, J.J., et al., *Shear stress inhibits smooth muscle cell-induced inflammatory gene expression in endothelial cells: role of NF-kappaB.* Arterioscler Thromb Vasc Biol, 2005. **25**(5): p. 963-9.
164. Wang, P., et al., *Mechanical stretch regulates the expression of matrix metalloproteinase in rheumatoid arthritis fibroblast-like synoviocytes.* Connect Tissue Res, 2009. **50**(2): p. 98-109.
165. Takemura, M., et al., *Cyclic mechanical stretch augments hyaluronan production in cultured human uterine cervical fibroblast cells.* Mol Hum Reprod, 2005. **11**(9): p. 659-65.
166. Tyagi, S.C., et al., *Stretch-induced membrane type matrix metalloproteinase and tissue plasminogen activator in cardiac fibroblast cells.* J Cell Physiol, 1998. **176**(2): p. 374-82.
167. Li, J., et al., *Mechanical stretch changes coronary artery fibroblasts function by upregulating HSF1 protein expression.* Int J Biol Macromol, 2013. **59**: p. 105-10.
168. Hochmuth, R.M., *Micropipette aspiration of living cells.* Journal of Biomechanics, 2000. **33**(1): p. 15-22.
169. Lee, L.M. and A.P. Liu, *The Application of Micropipette Aspiration in Molecular Mechanics of Single Cells.* Journal of Nanotechnology in Engineering and Medicine, 2014. **5**(4): p. 0408011-0408016.
170. Plaza, G.R., et al., *Study of the influence of actin-binding proteins using linear analyses of cell deformability.* Soft Matter, 2015. **11**(27): p. 5435-46.
171. Kee, Y.S. and D.N. Robinson, *Micropipette aspiration for studying cellular mechanosensory responses and mechanics.* Methods Mol Biol, 2013. **983**: p. 367-82.
172. Luo, T., et al., *Molecular mechanisms of cellular mechanosensing.* Nat Mater, 2013. **12**(11): p. 1064-1071.
173. del Rio, A., et al., *Stretching single talin rod molecules activates vinculin binding.* Science, 2009. **323**(5914): p. 638-41.

174. Bonakdar, N., et al., *Mechanical plasticity of cells.* Nat Mater, 2016. **15**(10): p. 1090-1094.
175. Gavara, N. and R.S. Chadwick, *Relationship between cell stiffness and stress fiber amount, assessed by simultaneous atomic force microscopy and live-cell fluorescence imaging.* Biomechanics and Modeling in Mechanobiology, 2016. **15**(3): p. 511-523.
176. Mathur, A., et al., *Endothelial, cardiac muscle and skeletal muscle exhibit different viscous and elastic properties as determined by atomic force microscopy.* Journal of biomechanics, 2001. **34**(12): p. 1545-1553.
177. Ikai, A., *A review on: atomic force microscopy applied to nano-mechanics of the cell.* Adv Biochem Eng Biotechnol, 2010. **119**: p. 47-61.
178. Marshall, B.T., et al., *Force History Dependence of Receptor-Ligand Dissociation.* Biophysical Journal, 2005. **88**(2): p. 1458-1466.
179. Lee, C.-y., et al., *Actin depolymerization under force is governed by lysine 113:glutamic acid 195-mediated catch-slip bonds.* Proceedings of the National Academy of Sciences, 2013. **110**(13): p. 5022-5027.
180. del Rio, A., et al., *Stretching Single Talin Rod Molecules Activates Vinculin Binding.* Science, 2009. **323**(5914): p. 638-641.
181. Helfer, E., et al., *Buckling of Actin-Coated Membranes under Application of a Local Force.* Physical Review Letters, 2001. **87**(8): p. 088103.
182. Kumar, S., et al., *Viscoelastic retraction of single living stress fibers and its impact on cell shape, cytoskeletal organization, and extracellular matrix mechanics.* Biophys J, 2006. **90**(10): p. 3762-73.
183. Lele, T.P., et al., *Mechanical forces alter zyxin unbinding kinetics within focal adhesions of living cells.* Journal of Cellular Physiology, 2006. **207**(1): p. 187-194.
184. Chown, M.G. and S. Kumar, *Imaging and manipulating the structural machinery of living cells on the micro- and nanoscale.* Int J Nanomedicine, 2007. **2**(3): p. 333-44.
185. Chang, C.W. and S. Kumar, *Vinculin tension distributions of individual stress fibers within cell-matrix adhesions.* J Cell Sci, 2013. **126**(Pt 14): p. 3021-30.
186. Polacheck, W.J., et al., *Microfluidic platforms for mechanobiology.* Lab on a chip, 2013. **13**(12): p. 2252-2267.
187. Kamble, H., et al., *Cell stretching devices as research tools: engineering and biological considerations.* Lab on a Chip, 2016. **16**(17): p. 3193-3203.
188. Benbrahim, A., et al., *Characteristics of vascular wall cells subjected to dynamic cyclic strain and fluid shear conditions in vitro.* J Surg Res, 1996. **65**(2): p. 119-27.
189. Kim, C.H., et al., *Oscillatory fluid flow-induced shear stress decreases osteoclastogenesis through RANKL and OPG signaling.* Bone, 2006. **39**(5): p. 1043-7.
190. Luo, C.W., C.C. Wu, and H.J. Ch'ang, *Radiation sensitization of tumor cells induced by shear stress: the roles of integrins and FAK.* Biochim Biophys Acta, 2014. **1843**(9): p. 2129-37.
191. Shao, Y., et al., *Global architecture of the F-actin cytoskeleton regulates cell shape-dependent endothelial mechanotransduction.* Integrative Biology, 2014. **6**(3): p. 300-311.
192. Linsmeier, I., et al., *Disordered actomyosin networks are sufficient to produce cooperative and telescopic contractility.* Nat Commun, 2016. **7**.
193. Sakar, M.S., et al., *Cellular forces and matrix assembly coordinate fibrous tissue repair.* Nat Commun, 2016. **7**.

194. Sedzinski, J., et al., *Polar actomyosin contractility destabilizes the position of the cytokinetic furrow.* Nature, 2011. **476**(7361): p. 462-466.
195. Deakin, N.O. and C.E. Turner, *Paxillin comes of age.* Journal of Cell Science, 2008. **121**(15): p. 2435-2444.
196. Wozniak, M.A., et al., *Focal adhesion regulation of cell behavior.* Biochimica et Biophysica Acta (BBA) - Molecular Cell Research, 2004. **1692**(2-3): p. 103-119.
197. Turner, C.E., *Paxillin and focal adhesion signalling.* Nat Cell Biol, 2000. **2**(12): p. E231-E236.
198. Turner, C.E., *Paxillin interactions.* Journal of Cell Science, 2000. **113**(23): p. 4139-4140.
199. Oakes, P.W. and M.L. Gardel, *Stressing the limits of focal adhesion mechanosensitivity.* Curr Opin Cell Biol, 2014. **30C**: p. 68-73.
200. Chen, Y., et al., *Force regulated conformational change of integrin αVβ3.* Matrix Biology.
201. Margadant, C., et al., *Mechanisms of integrin activation and trafficking.* Curr Opin Cell Biol, 2011. **23**(5): p. 607-14.
202. Golji, J. and M.R.K. Mofrad, *A Molecular Dynamics Investigation of Vinculin Activation.* Biophysical Journal, 2010. **99**(4): p. 1073-1081.
203. Haining, A.W., T.J. Lieberthal, and A. Del Rio Hernandez, *Talin: a mechanosensitive molecule in health and disease.* FASEB J, 2016. **30**(6): p. 2073-85.
204. Oakes, P.W., et al., *Tension is required but not sufficient for focal adhesion maturation without a stress fiber template.* The Journal of Cell Biology, 2012. **196**(3): p. 363-374.
205. Shemesh, T., et al., *Focal adhesions as mechanosensors: A physical mechanism.* Proceedings of the National Academy of Sciences of the United States of America, 2005. **102**(35): p. 12383-12388.
206. Rossier, O.M., et al., *Force generated by actomyosin contraction builds bridges between adhesive contacts.* EMBO J, 2010. **29**(6): p. 1055-68.
207. Case, L.B., et al., *Molecular mechanism of vinculin activation and nanoscale spatial organization in focal adhesions.* Nat Cell Biol, 2015.
208. Dupont, S., *Role of YAP/TAZ in cell-matrix adhesion-mediated signalling and mechanotransduction.* Experimental Cell Research, 2016. **343**(1): p. 42-53.
209. Calvo, F., et al., *Mechanotransduction and YAP-dependent matrix remodelling is required for the generation and maintenance of cancer-associated fibroblasts.* Nat Cell Biol, 2013. **15**(6): p. 637-646.
210. Dupont, S., et al., *Role of YAP/TAZ in mechanotransduction.* Nature, 2011. **474**(7350): p. 179-183.
211. Sabass, B., et al., *High resolution traction force microscopy based on experimental and computational advances.* Biophys J, 2008. **94**(1): p. 207-20.
212. Oakes, P.W., et al., *Geometry regulates traction stresses in adherent cells.* Biophys J, 2014. **107**(4): p. 825-33.
213. Gardel, M.L., et al., *Traction stress in focal adhesions correlates biphasically with actin retrograde flow speed.* J Cell Biol, 2008. **183**(6): p. 999-1005.
214. Franck, C., et al., *Three-dimensional traction force microscopy: a new tool for quantifying cell-matrix interactions.* PLoS One, 2011. **6**(3).

215. Legant, W.R., et al., *Multidimensional traction force microscopy reveals out-of-plane rotational moments about focal adhesions.* Proceedings of the National Academy of Sciences, 2013. **110**(3): p. 881-886.
216. Oyen, M.L., *Mechanical characterisation of hydrogel materials.* International Materials Reviews, 2014. **59**(1): p. 44-59.
217. Ganz, A., et al., *Traction forces exerted through N-cadherin contacts.* Biology of the cell / under the auspices of the European Cell Biology Organization, 2006. **98**(12): p. 721-730.
218. du Roure, O., et al., *Force mapping in epithelial cell migration.* Proceedings of the National Academy of Sciences of the United States of America, 2005. **102**(7): p. 2390-2395.
219. Nelson, C., et al., *Emergent patterns of growth controlled by multicellular form and mechanics.* Proceedings of the National Academy of Sciences of the United States of America, 2005. **102**(33): p. 11594-11599.
220. Ruiz, S. and C. Chen, *Emergence of patterned stem cell differentiation within multicellular structures.* Stem cells (Dayton, Ohio), 2008. **26**(11): p. 2921-2927.
221. Rabodzey, A., et al., *Mechanical forces induced by the transendothelial migration of human neutrophils.* Biophysical Journal, 2008. **95**(3): p. 1428-1438.
222. Liu, Z., N. Sniadecki, and C. Chen, *Mechanical Forces in Endothelial Cells during Firm Adhesion and Early Transmigration of Human Monocytes.* Cellular and molecular bioengineering, 2010. **3**(1): p. 50-59.
223. Liang, X., et al., *Platelet retraction force measurements using flexible post force sensors.* Lab on a Chip, 2010. **10**(8): p. 991-998.
224. Baker, E.L., et al., *Cancer cell stiffness: integrated roles of three-dimensional matrix stiffness and transforming potential.* Biophys J, 2010. **99**(7): p. 2048-57.
225. Xu, W., et al., *Cell stiffness is a biomarker of the metastatic potential of ovarian cancer cells.* PLoS One, 2012. **7**(10): p. e46609.
226. Hayashi, K. and M. Iwata, *Stiffness of cancer cells measured with an AFM indentation method.* Journal of the Mechanical Behavior of Biomedical Materials, 2015. **49**: p. 105-111.
227. Sehgel, N.L., et al., *Increased vascular smooth muscle cell stiffness: a novel mechanism for aortic stiffness in hypertension.* Am J Physiol Heart Circ Physiol, 2013. **305**(9): p. H1281-7.
228. Sehgel, N.L., S.F. Vatner, and G.A. Meininger, *"Smooth Muscle Cell Stiffness Syndrome"-Revisiting the Structural Basis of Arterial Stiffness.* Front Physiol, 2015. **6**: p. 335.
229. Sehgel, N.L., et al., *Augmented vascular smooth muscle cell stiffness and adhesion when hypertension is superimposed on aging.* Hypertension, 2015. **65**(2): p. 370-7.
230. !!! INVALID CITATION !!! {Sehgel, 2015 #19769;Sehgel, 2015 #19770;Sehgel, 2013 #19771;Baker, 2010 #19716}.
231. Chiang, M.Y.M., et al., *Relationships among cell morphology, intrinsic cell stiffness and cell–substrate interactions.* Biomaterials, 2013. **34**(38): p. 9754-9762.
232. Tee, S.-Y., et al., *Cell Shape and Substrate Rigidity Both Regulate Cell Stiffness.* Biophysical Journal, 2011. **100**(5): p. L25-L27.
233. Warmflash, A., et al., *A method to recapitulate early embryonic spatial patterning in human embryonic stem cells.* Nat Meth, 2014. **11**(8): p. 847-854.

234. Wagner, E. and M. Glotzer, *Local RhoA activation induces cytokinetic furrows independent of spindle position and cell cycle stage.* The Journal of Cell Biology, 2016. **213**(6): p. 641-649.
235. Lau, K., et al., *Anisotropic stress orients remodelling of mammalian limb bud ectoderm.* Nat Cell Biol, 2015. **17**(5): p. 569-579.
236. Wyatt, T., B. Baum, and G. Charras, *A question of time: tissue adaptation to mechanical forces.* Current Opinion in Cell Biology, 2016. **38**: p. 68-73.
237. Mitchison, T.J., G.T. Charras, and L. Mahadevan, *Implications of a poroelastic cytoplasm for the dynamics of animal cell shape.* Semin Cell Dev Biol, 2008. **19**(3): p. 215-23.
238. Moeendarbary, E., et al., *The cytoplasm of living cells behaves as a poroelastic material.* Nat Mater, 2013. **12**(3): p. 253-261.
239. Kaunas, R. and H.-J. Hsu, *A kinematic model of stretch-induced stress fiber turnover and reorientation.* Journal of Theoretical Biology, 2009. **257**(2): p. 320-330.
240. Xu, G.-K., Y. Liu, and Z. Zheng, *Oriented cell division affects the global stress and cell packing geometry of a monolayer under stretch.* Journal of Biomechanics, 2016. **49**(3): p. 401-407.
241. Wyatt, T.P.J., et al., *Emergence of homeostatic epithelial packing and stress dissipation through divisions oriented along the long cell axis.* Proceedings of the National Academy of Sciences of the United States of America, 2015. **112**(18): p. 5726-5731.
242. Kim, E.H., et al., *Effect of cyclic stretching on cell shape and division.* BioChip Journal, 2015. **9**(4): p. 306-312.
243. Ragkousi, K. and M.C. Gibson, *Cell division and the maintenance of epithelial order.* The Journal of Cell Biology, 2014. **207**(2): p. 181-188.
244. Gudipaty, S.A. and J. Rosenblatt, *Epithelial cell extrusion: Pathways and pathologies.* Seminars in Cell & Developmental Biology.
245. Slattum, G.M. and J. Rosenblatt, *Tumour cell invasion: an emerging role for basal epithelial cell extrusion.* Nat Rev Cancer, 2014. **14**(7): p. 495-501.
246. Gu, Y. and J. Rosenblatt, *New emerging roles for epithelial cell extrusion.* Current opinion in cell biology, 2012. **24**(6): p. 865-870.
247. Fitts, R.H., D.R. Riley, and J.J. Widrick, *Functional and structural adaptations of skeletal muscle to microgravity.* Journal of Experimental Biology, 2001. **204**(18): p. 3201-3208.
248. Shin, M.E., et al., *Spatiotemporal organization, regulation, and functions of tractions during neutrophil chemotaxis.* Blood, 2010. **116**(17): p. 3297-310.
249. Dupays, L. and T. Mohun, *Spatiotemporal regulation of enhancers during cardiogenesis.* Cell Mol Life Sci, 2016.
250. Valent, E.T., et al., *Traction force dynamics predict gap formation in activated endothelium.* Exp Cell Res, 2016. **347**(1): p. 161-70.
251. Chen, C., et al., *Fluidization and resolidification of the human bladder smooth muscle cell in response to transient stretch.* PLoS One, 2010. **5**(8): p. e12035.
252. Chen, Y., et al., *Orientation-specific responses to sustained uniaxial stretching in focal adhesion growth and turnover.* Proc Natl Acad Sci U S A, 2013. **110**(26): p. E2352-61.

253. Ezratty, E.J., M.A. Partridge, and G.G. Gundersen, *Microtubule-induced focal adhesion disassembly is mediated by dynamin and focal adhesion kinase.* Nat. Cell Biol., 2005. **7**(6): p. 581-590.
254. Allingham, J.S., R. Smith, and I. Rayment, *The structural basis of blebbistatin inhibition and specificity for myosin II.* Nat. Struct. Mol. Biol., 2005. **12**(4): p. 378-379.
255. Holzinger, A., *Jasplakinolide: An actin-specific reagent that promotes actin polymerization.* Methods Mol. Biol. , 2009. **586**: p. 71-87.
256. Flanagan, M.D. and S. Lin, *Cytochalasins block actin filament elongation by binding to high affinity sites associated with F-actin.* J. Biol. Chem., 1980. **255**(3): p. 835-838.
257. Mann, J.M., et al., *A silicone-based stretchable micropost array membrane for monitoring live-cell subcellular cytoskeletal response.* Lab Chip, 2012. **12**(4): p. 731-740.
258. Yang, M.T., et al., *Assaying stem cell mechanobiology on microfabricated elastomeric substrates with geometrically modulated rigidity.* Nat. Protoc., 2011. **6**: p. 187-213.
259. Lu, S., et al., *Decipher the dynamic coordination between enzymatic activity and structural modulation at focal adhesions in living cells.* Sci. Rep., 2014. **4**: p. 5756.
260. Guo, B. and W.H. Guilford, *Mechanics of actomyosin bonds in different nucleotide states are tuned to muscle contraction.* Proceedings of the National Academy of Sciences, 2006. **103**(26): p. 9844-9849.
261. Kong, F., et al., *Demonstration of catch bonds between an integrin and its ligand.* The Journal of cell biology, 2009. **185**(7): p. 1275-1284.
262. Luo, T., et al., *Molecular mechanisms of cellular mechanosensing.* Nat. Mater., 2013. **12**(11): p. 1064-1071.
263. Luo, T., et al., *Understanding the cooperative interaction between myosin II and actin cross-linkers mediated by actin filaments during mechanosensation.* Biophys J, 2012. **102**(2): p. 238-47.
264. Ferrer, J.M., et al., *Measuring molecular rupture forces between single actin filaments and actin-binding proteins.* Proceedings of the National Academy of Sciences of the United States of America, 2008. **105**(27): p. 9221-9226.
265. Kong, F., et al., *Demonstration of catch bonds between an integrin and its ligand.* J. Cell Biol., 2009. **185**(7): p. 1275-1284.
266. Schultz, A.B., J.A. Faulkner, and V.A. Kadhiresan, *A simple Hill element-nonlinear spring model of muscle contraction biomechanics.* Journal of Applied Physiology, 1991. **70**(2): p. 803-812.
267. Glass, D.H., et al., *A viscoelastic biomechanical model of the cornea describing the effect of viscosity and elasticity on hysteresis.* Invest Ophthalmol Vis Sci, 2008. **49**(9): p. 3919-26.
268. Sato, M., et al., *Application of the micropipette technique to the measurement of cultured porcine aortic endothelial cell viscoelastic properties.* J Biomech Eng, 1990. **112**(3): p. 263-8.
269. Wang, D.H.J., et al., *Effect of intraluminal thrombus on wall stress in patient-specific models of abdominal aortic aneurysm.* Journal of Vascular Surgery, 2002. **36**(3): p. 598-604.
270. Honda, H., M. Tanemura, and T. Nagai, *A three-dimensional vertex dynamics cell model of space-filling polyhedra simulating cell behavior in a cell aggregate.* Journal of Theoretical Biology, 2004. **226**(4): p. 439-453.

271. Bidhendi, A.J. and R.K. Korhonen, *A finite element study of micropipette aspiration of single cells: effect of compressibility.* Comput Math Methods Med, 2012. **2012**: p. 192618.
272. Kuchen, E.E., et al., *Generation of leaf shape through early patterns of growth and tissue polarity.* Science, 2012. **335**(6072): p. 1092-6.
273. Tan, R.Z. and K.H. Chiam, *Computational modeling reveals that a combination of chemotaxis and differential adhesion leads to robust cell sorting during tissue patterning.* PLoS One, 2014. **9**(10): p. e109286.
274. Polyakov, O., et al., *Passive mechanical forces control cell-shape change during Drosophila ventral furrow formation.* Biophys J, 2014. **107**(4): p. 998-1010.
275. Li, D.S., J. Zimmermann, and H. Levine, *Modeling closure of circular wounds through coordinated collective motion.* Phys Biol, 2016. **13**(1): p. 016006.
276. Varner, V.D. and C.M. Nelson, *Computational models of airway branching morphogenesis.* Seminars in Cell & Developmental Biology.
277. Bansod, Y.D. and J. Bursa, *Continuum-Based Modelling Approaches for Cell Mechanics.* International Journal of Biological, Biomolecular, Agricultural, Food and Biotechnological Engineering, 2015. **9**: p. 947-959.
278. Goehring, N.W., et al., *Polarization of PAR Proteins by Advective Triggering of a Pattern-Forming System.* Science, 2011. **334**(6059): p. 1137-1141.
279. Oakes, Patrick W., et al., *Geometry Regulates Traction Stresses in Adherent Cells.* Biophysical Journal, 2014. **107**(4): p. 825-833.
280. Tee, Y.H., et al., *Cellular chirality arising from the self-organization of the actin cytoskeleton.* Nat Cell Biol, 2015. **17**(4): p. 445-457.
281. Elosegui-Artola, A., et al., *Mechanical regulation of a molecular clutch defines force transmission and transduction in response to matrix rigidity.* Nat Cell Biol, 2016. **18**(5): p. 540-548.
282. Livne, A., E. Bouchbinder, and B. Geiger, *Cell reorientation under cyclic stretching.* Nat Commun, 2014. **5**.
283. Lee, C.-Y., et al., *Actin depolymerization under force is governed by lysine 113:glutamic acid 195-mediated catch-slip bonds.* Proc. Natl. Acad. Sci. USA, 2013. **110**(13): p. 5022-5027.
284. Mitrossilis, D., et al., *Single-cell response to stiffness exhibits muscle-like behavior.* Proc. Natl. Acad. Sci. USA, 2009. **106**(43): p. 18243-18248.
285. Novikova, Elizaveta A. and C. Storm, *Contractile fibers and catch-bond clusters: A biological force sensor?* Biophy. J., 2013. **105**(6): p. 1336-1345.
286. Pereverzev, Y.V., et al., *The two-pathway model for the catch-slip transition in biological adhesion.* Biophy. J., 2005. **89**(3): p. 1446-1454.
287. Hirata, H., et al., *Force-dependent vinculin binding to talin in live cells: a crucial step in anchoring the actin cytoskeleton to focal adhesions.* American Journal of Physiology - Cell Physiology, 2014. **306**(6): p. C607-C620.
288. Rognoni, L., et al., *Dynamic force sensing of filamin revealed in single-molecule experiments.* Proceedings of the National Academy of Sciences, 2012. **109**(48): p. 19679-19684.

289. Parmley, W.W. and E.H. Sonnenblick, *Series elasticity in heart muscle. Its relation to contractile element velocity and proposed muscle models.* Circ. Res., 1967. **20**: p. 112-123.
290. MacIntosh, B.R. and M.B. MacNaughton, *The length dependence of muscle active force: Considerations for parallel elastic properties.* J. Appl. Physiol. , 2005. **98**(5): p. 1666-1673.
291. Hill, A.V., *The heat of shortening and the dynamic constants of muscle.* P. Roy. Soc. Lond. B. Bio., 1938. **126**: p. 136-195.
292. Kumar, S., et al., *Viscoelastic retraction of single living stress fibers and its impact on cell shape, cytoskeletal organization, and extracellular matrix mechanics.* Biophys. J., 2006. **90**(10): p. 3762-3773.
293. Lu, L., et al., *Mechanical properties of actin stress fibers in living cells.* Biophys. J., 2008. **95**(12): p. 6060-6071.
294. Veigel, C., et al., *Load-dependent kinetics of force production by smooth muscle myosin measured with optical tweezers.* Nat. Cell Biol., 2003. **5**(11): p. 980-986.
295. Finer, J.T., R.M. Simmons, and J.A. Spudich, *Single myosin molecule mechanics: piconewton forces and nanometre steps.* Nature, 1994. **368**(6467): p. 113-9.
296. Bartolak-Suki, E., et al., *Fluctuation-driven mechanotransduction regulates mitochondrial-network structure and function.* Nat Mater, 2015. **14**(10): p. 1049-1057.
297. Suki, B., et al., *Regulatory Roles of Fluctuation-Driven Mechanotransduction in Cell Function.* Physiology, 2016. **31**(5): p. 346.
298. Ochoa, C.D., et al., *Cyclic stretch affects pulmonary endothelial cell control of pulmonary smooth muscle cell growth.* Am J Respir Cell Mol Biol, 2008. **39**(1): p. 105-12.
299. Thayer, P., et al., *The effects of combined cyclic stretch and pressure on the aortic valve interstitial cell phenotype.* Ann Biomed Eng, 2011. **39**(6): p. 1654-67.
300. Birukov, K.G., *Cyclic stretch, reactive oxygen species, and vascular remodeling.* Antioxid Redox Signal, 2009. **11**(7): p. 1651-67.
301. Gupta, V. and K.J. Grande-Allen, *Effects of static and cyclic loading in regulating extracellular matrix synthesis by cardiovascular cells.* Cardiovasc Res, 2006. **72**(3): p. 375-83.
302. Shimizu, N., et al., *Cyclic strain induces mouse embryonic stem cell differentiation into vascular smooth muscle cells by activating PDGF receptor beta.* J Appl Physiol 2008. **104**(3): p. 766-72.
303. Shyu, K.G., et al., *Cyclical mechanical stretching increases the expression of vascular endothelial growth factor in rat vascular smooth muscle cells.* J Formos Med Assoc, 2001. **100**(11): p. 741-7.
304. Ohashi, T., et al., *Nonuniform strain of substrate induces local development of stress fibers in endothelial cells under uniaxial cyclic stretching.* Clin Hemorheol Microcirc, 2007. **37**(1-2): p. 37-46.
305. Chen, Y., et al., *Orientation-specific responses to sustained uniaxial stretching in focal adhesion growth and turnover.* Proceedings of the National Academy of Sciences of the United States of America, 2013.
306. Park, J.-A., et al., *Unjamming and cell shape in the asthmatic airway epithelium.* Nat Mater, 2015. **14**(10): p. 1040-1048.

307. Yang, C., et al., *Mechanical memory and dosing influence stem cell fate.* Nat Mater, 2014. **13**(6): p. 645-652.
308. Kong, F., et al., *Cyclic Mechanical Reinforcement of Integrin–Ligand Interactions.* Molecular Cell, 2013. **49**(6): p. 1060-1068.
309. Chen, X., Z. Mao, and B. Chen, *Probing time-dependent mechanical behaviors of catch bonds based on two-state models.* Scientific Reports, 2015. **5**: p. 7868.
310. Jacquemet, G., H. Hamidi, and J. Ivaska, *Filopodia in cell adhesion, 3D migration and cancer cell invasion.* Curr Opin Cell Biol, 2015. **36**: p. 23-31.
311. Heckman, C.A. and H.K. Plummer Iii, *Filopodia as sensors.* Cellular Signalling, 2013. **25**(11): p. 2298-2311.
312. Mattila, P.K. and P. Lappalainen, *Filopodia: molecular architecture and cellular functions.* Nat Rev Mol Cell Biol, 2008. **9**(6): p. 446-54.
313. Gupton, S.L. and F.B. Gertler, *Filopodia: The Fingers That Do the Walking.* Science's STKE, 2007. **2007**(400): p. re5-re5.
314. Bornschlogl, T., *How filopodia pull: what we know about the mechanics and dynamics of filopodia.* Cytoskeleton (Hoboken), 2013. **70**(10): p. 590-603.
315. Leijnse, N., L.B. Oddershede, and P.M. Bendix, *An updated look at actin dynamics in filopodia.* Cytoskeleton (Hoboken), 2015. **72**(2): p. 71-9.
316. Condeelis, J.S., et al., *Lamellipodia in invasion.* Semin Cancer Biol, 2001. **11**(2): p. 119-28.
317. Cramer, L.P., *Molecular mechanism of actin-dependent retrograde flow in lamellipodia of motile cells.* Front Biosci, 1997. **2**: p. d260-70.
318. Salbreux, G., G. Charras, and E. Paluch, *Actin cortex mechanics and cellular morphogenesis.* Trends in Cell Biology. **22**(10): p. 536-545.
319. Fehon, R.G., A.I. McClatchey, and A. Bretscher, *Organizing the cell cortex: the role of ERM proteins.* Nat Rev Mol Cell Biol, 2010. **11**(4): p. 276-87.
320. Lee, S. and S. Kumar, *Actomyosin stress fiber mechanosensing in 2D and 3D.* F1000Research, 2016. **5**: p. F1000 Faculty Rev-2261.
321. Tojkander, S., G. Gateva, and P. Lappalainen, *Actin stress fibers – assembly, dynamics and biological roles.* Journal of Cell Science, 2012. **125**(8): p. 1855-1864.
322. du Roure, O., *Force mapping in epithelial cell migration.* Proc. Natl. Acad. Sci. USA, 2005. **102**: p. 2390-2395.
323. Saez, A., et al., *Is the mechanical activity of epithelial cells controlled by deformations or forces?* Biophys. J., 2005. **89**(6): p. L52-L54.
324. Fu, J., et al., *Mechanical regulation of cell function using geometrically modulated elastomeric substrates.* Nat. Methods, 2010. **7**: p. 733-736.